UNIVERSITY OF CALIFORNIA,
IRVINE

Modeling the dynamics of Thwaites Glacier, West Antarctica

DISSERTATION

submitted in partial satisfaction of the requirements
for the degree of

DOCTOR OF PHILOSOPHY

in Earth System Science

by

Hongju Yu

Dissertation Committee:
Professor Eric Rignot, Chair
Professor Mathieu Morlighem
Professor Isabella Velicogna
Professor Michael Pritchard

2018

TABLE OF CONTENTS

LIST OF FIGURES

Page

LIST OF TABLES

ACKNOWLEDGMENTS

I would like to thank my PhD advisor Eric Rignot for taking me as his PhD student when I have no background in glaciology. During these six years, he has been very patient and supportive in guiding me through academic research. His deep undertandings and brillinat ideas about glaciology greatly helped my work since the first day. His devotion and enthusiasm to science set a great example for me.

This work would not be possible without the help I recevied from a lot of people during these years. Mathieu Morlighem and Helene Seroussi are the ones leading me into ice sheet modeling from the very beginning. They provided me great help in coding, discussing about my work and editing my paper. I'm also thankful to Mathieu Morlighem, Isabella Velicogna and Michael Pritchard for serving in my committee. They provided inspiring suggestions along the way and helped editting my thesis.

I feel grateful to be a part of the cryosphere group at UCI. I have learned a lot from my collegues, who are always willing to help. It's a great pleasure to to work with them. Their support and encouragement have helped me survive the years. I also thank the Department of Earth System Science. This department has a great atmoshpere for both research and person connections. I have enjoyed every minute in the time spent here with all the great people.

I thank my parents and my friends for their love and company. They are always their when I needed them and they are the ones who kept me strong in this journey.

This work was performed at University of California, Irvine, funded by a contract with National Aeronautics and Space Administration Crysphere Science.

Parts of Chapter 2, 3 and 4 are reprinted from a publication in The Cryosphere. Part of Chapter 2 and 5 are reprinted from a publication recently submitted to The Cryosphere with the permission from all co-authors.

CURRICULUM VITAE

Hongju Yu

EDUCATION

Doctor of Philosophy in Earth System Science **2018**
University of California *Irvine, California*

Master of Science in Earth System Science **2014**
University of California *Irvine, California*

Bachelor of Science in Atmospheric Science **2012**
Nanjing University *Nanjing, CHINA*

RESEARCH EXPERIENCE

Graduate Research Assistant **2012–2018**
Advisor: Prof. Eric Rignot *UC, Irvine*

TEACHING EXPERIENCE

Catastrophe Teaching Assistant **Fall 2016**
Instructor: Dr. Elizabeth Cook *UC Irvine*

Atmoshphere Teaching Assistant **Spring 2016**
Instructor: Dr. Elizabeth Cook *UC Irvine*

Modeling the Earth Teaching Assistant **Spring 2015**
Instructor: Prof. Mathieu Morlighem *UC Irvine*

Climate Change Teaching Assistant **Winter 2015**
Instructor: Prof. Michael Pritchard *UC Irvine*

Introduction to Earth System Science Teaching Assistant **Fall 2014**
Instructor: Dr. Julie Ferguson *UC Irvine*

The Atmoshphere Teaching Assistant **Spring 2014**
Instructor: Dr. Julie Ferguson *UC Irvine*

PUBLICATIONS

Yu, H., Rignot, E., Morlighem, M., & Seroussi, H. (2017). Iceberg calving of Thwaites Glacier, West Antarctica: full-Stokes modeling combined with linear elastic fracture mechanics, *The Cryosphere*, 11(3), 1283-1296.

Yu, H., Rignot, E., Seroussi, H. & Morlighem, M. (2018). Retreat of Thwaites Glacier, West Antarctica, over the next 100 years using various ice flow models, ice shelf melt scenarios and basal friction laws, *The Cryosphere, in review.*

CONFERENCE PRESENTATIONS

Hongju Yu, Eric Rignot, Mathieu Morlighem and Hélène Seroussi (2017). "3D modeling of continuous retreat of Thwaites Glacier, West Antarctica, under enhanced basal melting". AGU Fall Meeting 2017. New Orleans, LA.

Hongju Yu, Eric Rignot, Mathieu Morlighem and Hélène Seroussi (2016). "3D full-Stokes modeling of the grounding line dynamics of Thwaites Glacier, West Antarctica". AGU Fall Meeting 2016. San Francisco, CA.

Hongju Yu, Eric Rignot, Mathieu Morlighem and Hélène Seroussi (2016). "Full-Stokes modeling of grounding-line dynamics and iceberg calving for Thwaites Glacier,West Antarctica". International Symposium on Interactions of Ice Sheets and Glaciers with the Ocean. San Diego, CA.

Hongju Yu, Eric Rignot and Mathieu Morlighem(2015). "Modeling of the calving dynamics of Thwaites Glacier, West Antarctica". AGU Fall Meeting 2015. San Francisco, CA.

Hongju Yu, Eric Rignot, Mathieu Morlighem, Hélène Seroussi and Eric Larour (2014). "Modeling the grounding line dynamics of Thwaites Glacier, West Antarctica using Full Stokes and lower order models". AGU Fall Meeting 2014. San Francisco, CA.

Hongju Yu, Eric Rignot, Mathieu Morlighem and Hélène Seroussi (2013). "Steady State of Thwaites Glacier, West Antarctica". AGU Fall Meeting 2013. San Francisco, CA.

ABSTRACT OF THE DISSERTATION

Modeling the dynamics of Thwaites Glacier, West Antarctica

By

Hongju Yu

Doctor of Philosophy in Earth System Science

University of California, Irvine, 2018

Professor Eric Rignot, Chair

Thwaites Glacier (TG), West Antarctica, has been experiencing rapid mass loss and grounding line retreat in the past few decades. The mass loss of TG is now responsible for 4% of global sea level rise. It is therefore crucial to simulate the future evolution of TG to make projections for future sea level rise. The cause of the dramatic changes is dynamic through the loss of buttressing from its ice shelf due to calving and ice shelf melting. In this thesis, we employ various numerical ice sheet models to study the calving dynamics of TG and the response of TG to enhanced ice shelf melting. We combine a two-dimensional ice flow model with the linear elastic fracture mechanics (LEFM) theory to model crevasse propagation and ice fracturing. We find that the combination of a full-Stokes (FS) model and LEFM produces surface and bottom crevasses that are consistent with the distribution of depth and width of surface and bottom crevasses observed, whereas the combinations of simplified models with LEFM do not. We find that calving is enhanced when pre-existing surface crevasses are present, when the ice shelf is shortened, or when the ice shelf front is undercut. We show that the FS/LEFM combination yields substantial improvements in capturing the stress field near the grounding line of a glacier for constraining crevasse formation and iceberg calving. We then simulate the evolution of TG under different ice shelf melt scenarios and different ice sheet model configurations. We find that the grounding line retreat and its sensitivity to ocean forcing is enhanced when a full-Stokes model is used, ice shelf melt is applied on

partially floating elements, and a Budd friction is used. Initial conditions also impact the model results. Yet, all simulations suggest a rapid, sustained retreat along the same preferred pathway. The highest retreat rate occurs on the eastern side of the glacier and the lowest rate on a subglacial ridge on the western side. Combining the results, we find the differences among simulations are small in the first 30 years, with a cumulative contribution to sea level rise of 5 mm, similar to the current rate. After 30 years, the mass loss highly depends on the model configurations, with a 300% difference over the next 100 years, ranging from 14 to 42 mm.

Chapter 1

Introduction

1.1 Background

The global mean sea level (GMSL) has been increasing at 1.7 mm/yr in the 20th century, according to the Intergovernmental Panel on Climate Change (IPCC) Fifth Assessment Report (*Stocker et al.*, 2013). In the past two decades, this rate has increased to 3.2 mm/yr (Fig. 1.1). This increase of sea level is mostly dominated by the thermal expansion of the ocean and the mass loss of glaciers. In particular, the contribution to the sea level rise from the Antarctic Ice Sheet (AIS) increased from 0.08 mm/yr in 1992-2001 to 0.40 mm/yr in 2002-2011 (*Stocker et al.*, 2013).

According to the IPCC report (*Stocker et al.*, 2013), the future projection of GMSL rise is 0.63 m in 2081–2100 relative to 1986–2005 following the RCP 8.5 scenario. Among this, the contribution from AIS is 0.03 m. Although the contribution is small, ice sheets produce the largest uncertainty of this projection because the confidence in the simulation of ice sheet dynamics is currently low compared to other components in the Earth system. Moreover, the potential collapse of the West Antarctic Ice Sheet (WAIS) is also not considered in

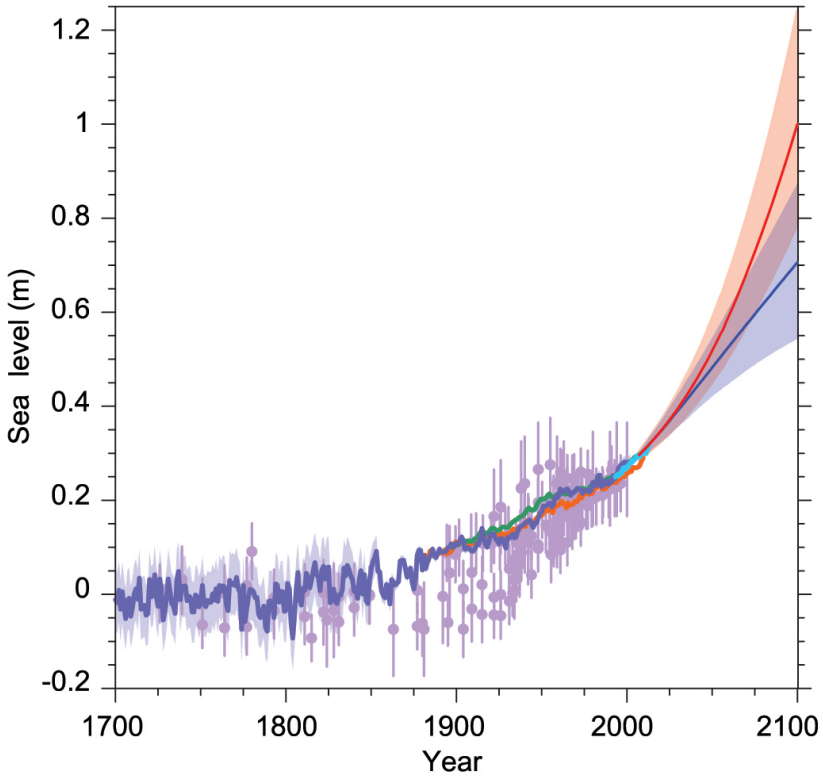

Figure 1.1: Sea level history from paleo-climate data (purple), tide gauge data (blue, red and green), altimeter data (light blue) and future projections from CMIP5 and process-based models for RCP2.6 (blue) and RCP8.5 (red) scenarios, all relative to pre-industrial values (*Stocker et al.*, 2013).

this projection, which might be able to raise GMSL by several tens of centimeters before 2100. Previous studies have shown the Amundsen Sea Embayment (ASE) section of WAIS is currently experiencing the most rapid changes in AIS and may continue losing mass due to its bed configuration (*Fretwell et al.*, 2013; *Medley et al.*, 2014; *Rignot et al.*, 2008). Located in ASE, Thwaites Glacier (TG) has also been observed to lose mass in the past three decades (*Mouginot et al.*, 2014; *Rignot et al.*, 2014). With a vast majority of its drainage basin below sea level, TG is under the risk of collapse due to rapid dynamical changes. Whether this collapse will happen or when this collapse will happen, however, is not well understood.

1.2 Antarctic Ice Sheet

AIS was first formed 34 million years ago due to the decrease of atmospheric CO_2 level and Earth's temperature (*Mayewski et al.*, 2009). The extent of AIS then fluctuated in response to the changes of Earth's orbit, which altered GMSL by 30 to 60 m (*Barrett*, 2009; *Naish et al.*, 2001). The current configuration of AIS was formed 14 million years ago, which is suggested to have survived the Pliocene warming 5 to 3 million years ago (*Flower and Kennett*, 1994; *Kennett and Hodell*, 1993). In the last million years, the climate of Earth was alternating between long cold glacials (∼90,000 years) with GMSL 120 m lower than present, and short warm interglacials (∼10,000 years) with the GMSL near or slightly higher than present (*Mayewski et al.*, 2009). In the last interglacial period (∼125,000 years ago), the GMSL is considered to be 5.5 to 9 m higher than present. Among this, 2.5 to 4 m is caused by the disintegration of the AIS (*Dutton and Lambeck*, 2012; *Kopp et al.*, 2009).

Currently, AIS contains the largest amount of ice on Earth with a total ice extent of 1.4×10^{17} km^2 and a total ice volume of 2.7×10^7 km^3 (∼90% of total world's ice). With this amount of ice, AIS has the potential to raise the global sea level by 58.3 m (*Fretwell et al.*, 2013). The mass balance of Antarctic Ice Sheet has been decreasing in the past few decades as a result of global warming (Fig. 1.2). During the period between 1992 and 2001, the total mass balance for the AIS is -71±53 Gt/yr. According to the studies from *Shepherd et al.* (2012), the mass loss rate has been increasing rapidly within this period, from -48±53 Gt/yr in 1992-2000 to -81±37 Gt/yr in 2000-2011 (Table. 1.1).

Within the AIS, different regions have different trends and rates in their mass balance. The WAIS is the region that dominates the mass loss of the whole Antarctica. An average of 65±26 Gt of ice was lost into the ocean in this area from 1992 to 2011. The rate of mass loss also increased abruptly from 66 Gt/yr in 1996 to 112 Gt/yr in 2006 (*Rignot et al.*, 2008; *Shepherd et al.*, 2012). The mass loss is attributed to the intrusion of warm ocean water,

which enhanced ice shelf melting and calving of ice shelves (*Dutrieux et al.*, 2014; *Jacobs et al.*, 2011). The loss of ice shelves have negligible impact on GMSL. However, it leads to dynamical changes of glaciers upstream, such as glacial speeding up and grounding line retreat. These dynamical changes result in the significant thinning and mass loss of WAIS (*Pritchard et al.*, 2009; *Rignot*, 2008a; *Rignot et al.*, 2011b, 2014).

The Antarctic Peninsula (AP) is another region that is experiencing dramatic changes in the past few decades. The temperature has increased by 2°C since the 1950s and the mass loss rate has increased from 8 Gt/yr in 1992–2000 to 20 Gt/yr in 2000–2011 (*Cook et al.*, 2005; *Shepherd et al.*, 2012). The majority of ice shelves in AP are undergoing fast retreat, including the disintegration of Larsen A in 1995 and Larsen B in 2002 (*Cook et al.*, 2005). Similar to WAIS, following the fast retreat and collapse of ice shelves, significant glacier speed up is observed, which leads to further mass loss and retreat (*Berthier et al.*, 2012; *Rott et al.*, 2011).

The East Antarctic Ice Sheet (EAIS) is a region where the changes are small. In the last two decades, EAIS is about in balance with an averaging mass gain of 14±43 Gt/yr from 1992 to 2011, probably due to an increase of precipitation (*Bracegirdle et al.*, 2008; *Shepherd et al.*, 2012). However, significant mass loss is still observed in Cook and Totten Glaciers, which shows East Antarctica is also not immune to changes (*Li et al.*, 2016; *Rignot*, 2006).

Over the whole AIS, the trend in surface mass balance (SMB) is small compared to inter-annual variability in the past three decades (*Uotila et al.*, 2007). Future projections also suggest that the SMB of AIS will increase in the next century due to the increase in precipitation, which would mitigate the rise of GMSL (*Krinner et al.*, 2007; *Bracegirdle et al.*, 2008). Therefore, the mass loss of the AIS is owned to the dynamical changes that are induced from the loss of ice shelves in WAIS, AP and a few glaciers in EAIS.

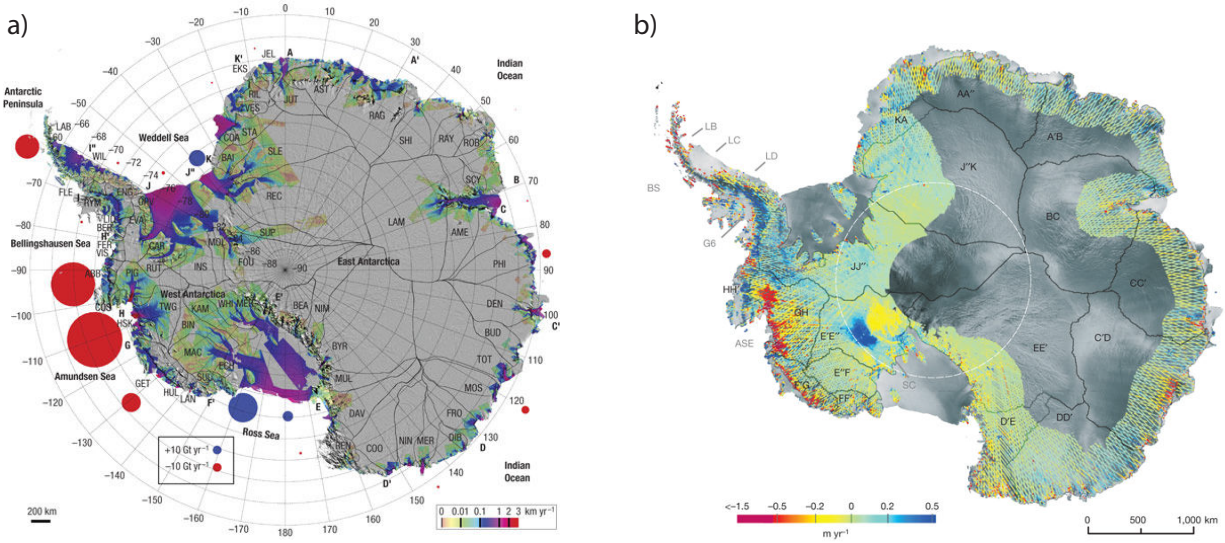

Figure 1.2: Current state of the Antarctic Ice Sheet. a) Mass balance and ice velocity of Antarctica. The maps shows ice velocity overlaid on a MODIS mosaic of Antarctica. Circles represent mass gain (blue) and loss (red) in Gt/yr for each drainage basin. Black lines are the boundaries of the drainage basins (*Rignot et al.*, 2008). b) Surface elevation change of Antarctica in m/yr over the period 2003–2007 (*Pritchard et al.*, 2009).

Region	1992-2011 (Gt/year)	1992-2000 (Gt/year)	1993-2003 (Gt/year)	2000-2011 (Gt/year)	2005-2010 (Gt/year)
AP	-20 ± 14	-8 ± 17	-12 ± 17	-29 ± 12	-36 ± 10
EAIS	14 ± 43	-2 ± 54	-9 ± 50	26 ± 36	58 ± 31
WAIS	-65 ± 26	-38 ± 32	-49 ± 31	-85 ± 22	-102 ± 18
AIS	-71 ± 53	-48 ± 65	-71 ± 61	-87 ± 43	-81 ± 37

Table 1.1: Reconciled mass balance of the Antarctic Ice Sheet during various time periods from 1992 to 2010 (*Shepherd et al.*, 2012).

1.3 Marine Ice Sheet Instability

To make reliable projections of the contribution from ice sheets to GMSL rise, it is important to understand the dynamics of ice sheets and their responses to external changes. *Weertman* (1974) proposed a theory that ice sheets with retrograde beds are inherently unstable to changes, i.e. small perturbations from its environment can cause irreversible retreat or advance. This theory is now referred to as the Marine Ice Sheet Instability (MISI) theory.

The mechanism of MISI theory is shown in Fig. 1.3. A marine ice sheet gains mass through surface mass balance over all of its grounded area. At the same time, it loses mass through the ice mass flux at the grounding line. In a steady state, the total mass gain is equal to the total mass loss. If an external forcing forces the grounding line to retreat, the total surface accumulation would decrease since the total area of grounded ice decreases, which leads to a decrease in total mass gain. If the ice sheet has a prograde bed (Fig. 1.3A), the grounding line would retreat to a shallower water depth. In this case, the ice thickness at the grounding line decreases and leads to a decrease in ice mass flux at the grounding line. Therefore, the total mass loss is also reduces. In this way, with the reduction of both mass gain and mass loss, the ice sheet is able to find a new steady state. However, if the grounding line retreats into deeper water depth in a retrograde bed case (Fig. 1.3B), the ice thickness at the grounding line will increase. This means an increase in ice mass flux at the grounding line and an increase in total mass loss. Due to the decrease of mass gain and increase in mass loss, the ice sheet would have a negative balance. This negative mass balance would in turn lead to further retreat of the ice sheet, which forms a positive feedback until the ice sheet reaches prograde bed or collapse entirely (*Weertman*, 1974; *Thomas*, 1979).

The MISI theory is confirmed by *Schoof* (2006) through an analysis with the boundary layer theory. According to this theory, the ice flux through the grounding line is approximately proportional to the fifth power of ice thickness at the grounding line. With a retrograde bed,

ice flux would increase sharply as the grounding line retreats. Therefore, marine ice sheets are unable to have stable grounding line positions on beds with reverse slopes. However, in these studies, the MISI theory is derived and confirmed in a 2D perspective. In 3D, this instability can be suppressed by lateral drag and ice-shelf buttressing (*Dupont and Alley*, 2005; *Gudmundsson et al.*, 2012). The behavior of an ice sheet is dependent on the combining effect of the MISI and the stabilizing effects, which is unique for every glacier basin. Therefore, numerical modeling is required to estimate the potential stability (instability) of any glacier.

In the majority of Antarctica, the bed is deeper inland because of isostatic depression, which makes the ice sheet unstable according to the MISI theory (Fig. 1.4). Therefore, many studies have been done to model the stability of AIS. In particular, the WAIS has drawn the most attention since its bed is both retrograde and immersed in warm ocean water. *Hughes* (1981) raised the idea that the WAIS may disintegrate in a CO_2 induced climatic warming scenario. *Feldmann and Levermann* (2015) also showed that the topographic features in the WAIS are unable to halt MISI after its initiation and a collapse of WAIS is irrevocable if a local destabilization is initiated in the ASE sector.

1.4 Ice Sheet Modeling

The basic concept of ice sheet modeling is to treat ice as an incompressible fluid with nonlinear viscosity that is driven by gravity. In this way, the flow of ice can be computed through the conservation laws of mass, momentum and energy.

The flow law of ice was first derived by Glen in 1955. Through laboratory experiments, he proposed that the deformation of ice under stress follows a flow law:

$$\dot{\varepsilon} = B\sigma^n \tag{1.1}$$

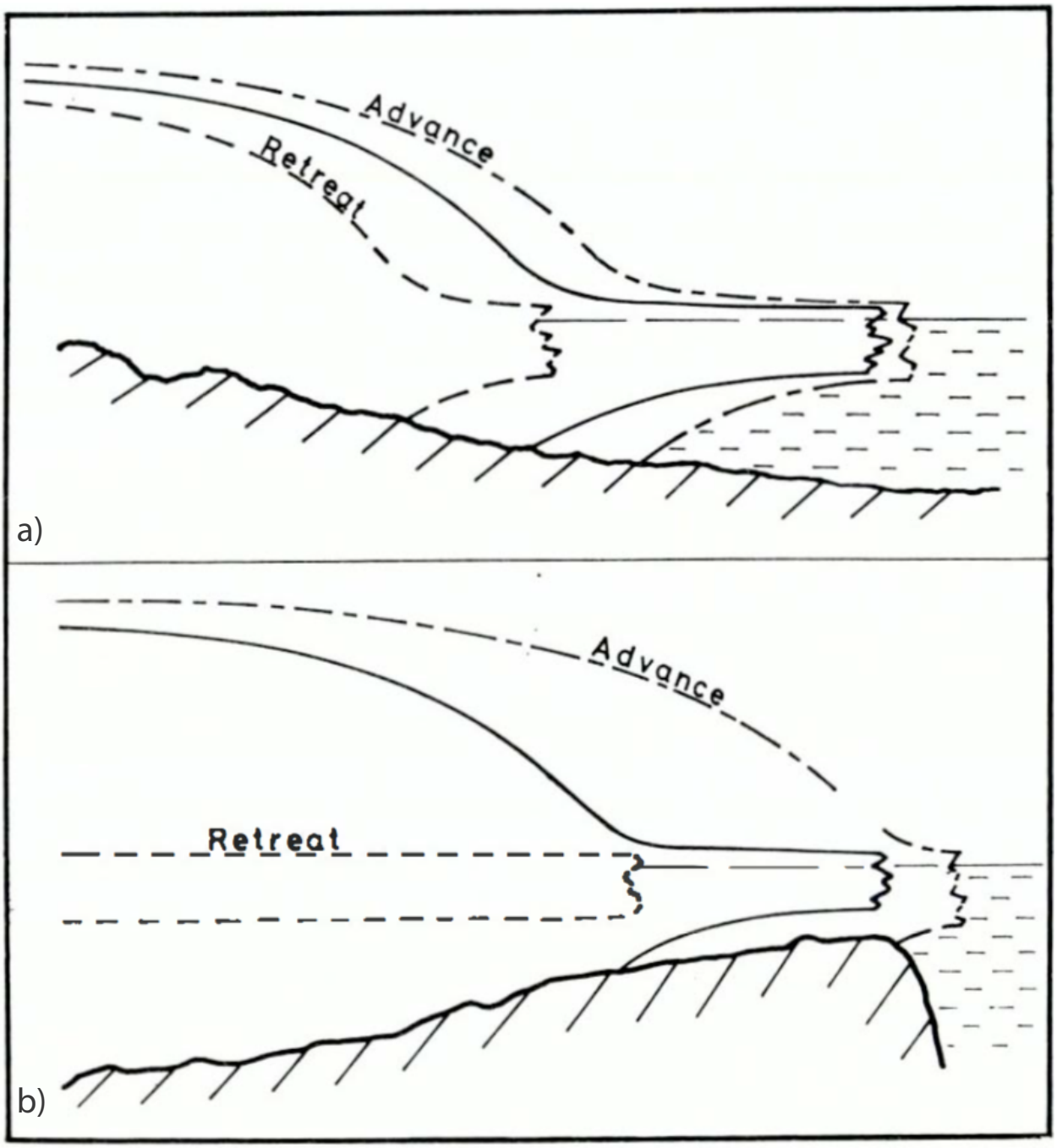

Figure 1.3: Schematic of the Marine Ice Sheet Instability theory with different bed configurations. A) A stable configuration with prograde bed. B) An unstable configuration with retrograde bed. The solid lines are initial ice sheet profile. The dash lines are ice sheet profile if a small grounding line retreat occurs and the dotted dash lines are ice sheet profile if a small grounding line advance occurs. (*Thomas*, 1979)

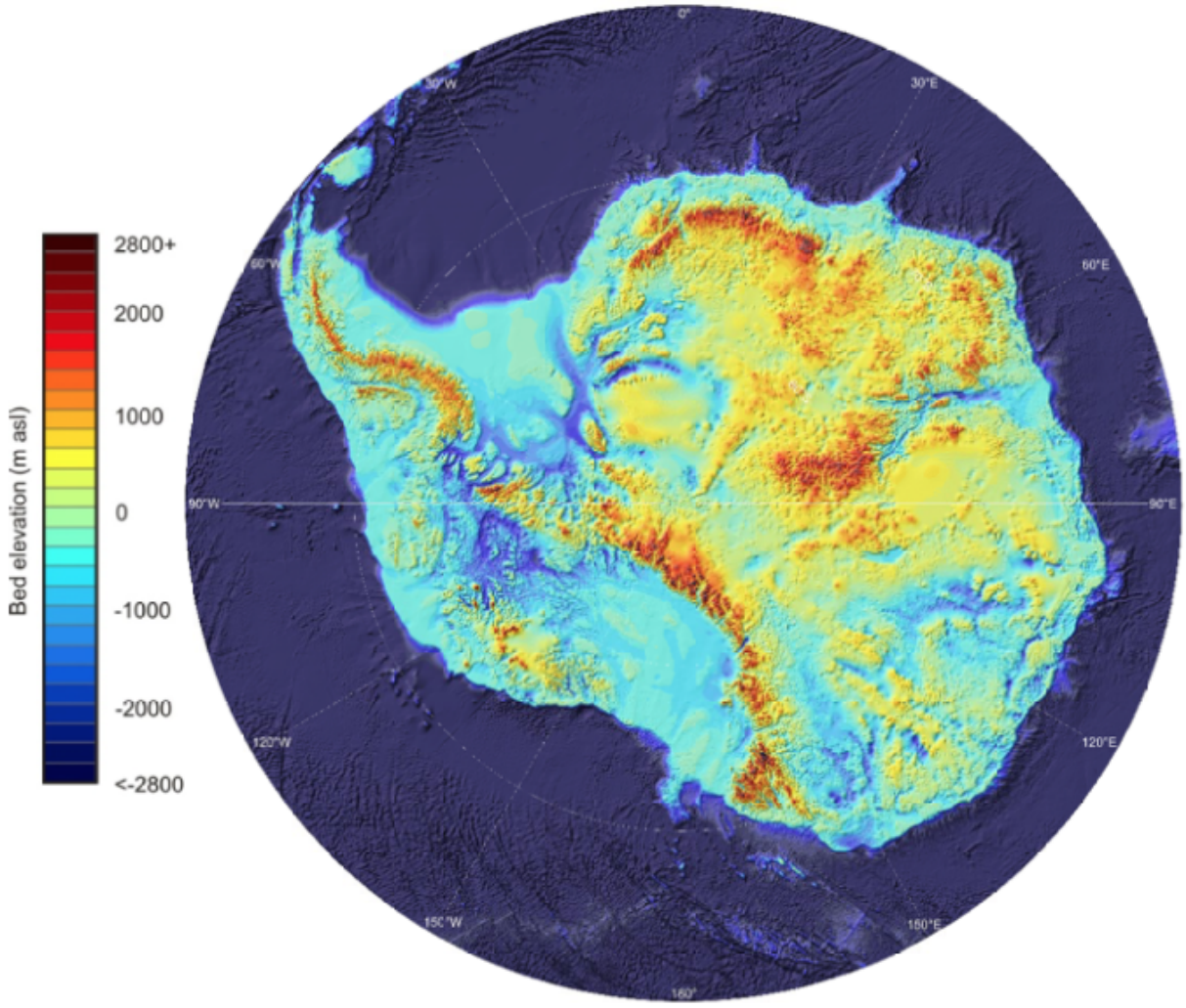

Figure 1.4: Bed elevation of the Antarctica Ice Sheet from BEDMAP2 (*Fretwell et al.*, 2013).

where $\dot{\boldsymbol{\varepsilon}}$ is the strain rate, B the ice hardness, σ the applied stress and n is a constant about 3 (*Glen*, 1952, 1955). This flow law was then confirmed using field observations of the closure of tunnels in glaciers (*Nye*, 1953). *Nye* (1957a) also extended Glen's flow law by writing it into a tensorial form, the details of which will be discussed in Chapter 2 of this thesis. *Weertman* (1957) developed a sliding law for glaciers whose ice bottom temperature is at the melting point, where the sliding velocity is non-linearly dependent on basal drag. After these studies, the glacier flow problem became a fluid mechanics problem and rigorous mathematical analyses started to emerge (*Blatter et al.*, 2010).

Numerical ice sheet modeling started in the 1970s. The first 3D ice sheet model was developed based on Glen's flow law by *Mahaffy* (1976) on the Barnes Ice Cap. Continental scale modeling began when *Jenssen* (1977) applied an ice sheet model to the Greenland Ice Sheet. To solve the ice flow problem requires solving a set of the full-Stokes equations. Due to limited computational resources, these earlier models all try to solve an approximation of the full-Stokes equations, the shallow ice approximation (SIA), a stress balance approximation that was formally derived later by *Hutter* (1983) and *Morland* (1984). With SIA, the only stress component to consider is the vertical shear and the speed of ice is locally determined, which means it requires little computational power. This approximation is good at continental scale paleo-climate reconstructions (*Ritz et al.*, 1997; *Huybrechts et al.*, 2004). However, it breaks down in some key areas, such as the grounding line region, and is therefore inadequate for realistic simulations of smaller glaciers with complex bed topography (*Blatter et al.*, 2010). For this reason, new force balance approximations that can more accurately represent glacier dynamics but are more computationally demanding have been developed since the 1980s.

There are now two other widely used approximations reduced from the full-Stokes equations. The first is the shelfy-stream approximation (SSA), a depth averaged 2D model developed by *MacAyeal* (1989) and *Morland* (1987). The second one is the higher order (HO) approximation, a 3D model developed by *Blatter* (1995) and *Pattyn* (2003). Even though these approximations are much more computationally expensive than SIA, they have been used extensively in the community thanks to the rapid increase of computing power. Studies using these two approximations have made success in simulating ice dynamics in both theoretical and realistic settings (*Joughin et al.*, 2014; *Larour et al.*, 2012; *MacAyeal*, 1992; *Pattyn et al.*, 2013; *Cornford et al.*, 2013; *Seroussi and Price*, 2014). In recent years, models that applied the full-Stokes (FS) equations have also been developed. With no assumptions on the stress field, the FS model is much more computationally expensive than SSA and HO, but it can capture more details of ice dynamics in key regions, such as the grounding line region (*Durand et al.*, 2009b; *Morlighem et al.*, 2010; *Favier et al.*, 2014). Continental scale

modeling with FS, however, is still unavailable due to its high requirement of computing resources and spatial resolution.

1.5 Thwaites Glacier

Thwaites Glacier (TG) is a marine terminating glacier located in the ASE sector of West Antarctica. It drains an area of 1.8×10^5 km^3 with the majority of its bed retrograde and below sea level (Fig. 1.5b). In total, TG contains ice equivalent to 0.59 m of GMSL (*Holt et al.*, 2006). The flow speed of TG is fast (Fig. 1.5a). In the center trunk, the ice speed is approximately 2000 m/yr at the grounding line. The ice shelf of TG can be clearly divided into two parts according to the flow speed. In the western ice shelf, which drains ice from the center trunk, the maximum ice speed can reach 4000 m/yr near the ice front. In the eastern ice shelf, where the ice front terminates at an ice rise, the flow speed is slow, at only few hundreds of meters per year (*Rignot et al.*, 2011a; *Mouginot et al.*, 2014; *Rignot et al.*, 2014). TG is also the widest ice stream in West Antarctica with a width of 120 km. As one of the largest ice discharger in AIS, 126 Gt of ice is discharged into the ocean in 2014, nearly three times of Jakobshavn Isbrae, the largest discharger of ice in Greenland (*Mouginot et al.*, 2014).

Recent satellite observations have shown rapid mass loss of TG in the past few decades. *Rignot* (2001) found that TG is losing mass at a rate of 15 Gt/yr in 1996. Along with this mass loss, the grounding line retreated by 1.4 km from 1992 to 1996. Recent studies revealed that the mass loss of TG is continuing and accelerating. In the past decade, the mass loss rate has increased to 28 Gt/yr in 2006 and then to 50 Gt/yr in 2014 (*Medley et al.*, 2014; *Mouginot et al.*, 2014; *Rignot*, 2008b). Meanwhile, from 1992 to 2011, the grounding line of TG has retreated by 14 km (*Rignot et al.*, 2014). Significant surface thinning is also observed in TG. At the grounding line region, the surface thinning rate is over 4 m/yr and this thinning

signal propagates inland, with over 1 m/yr thinning 100 km upstream of the grounding line (*Pritchard et al.*, 2009). The rate of change in mass loss increased from 2.7 Gt/yr^2 in 1978-2014 to 3.2 Gt/yr^2 in 1992-2014, and 5.6 Gt/yr^2 in 2002-2014 (*Mouginot et al.*, 2014). If these rates maintain over the coming decades, they would raise GMSL by, respectively, 41, 48 and 81 mm by 2100. The rapid mass loss of TG is resulted from dynamical changes.

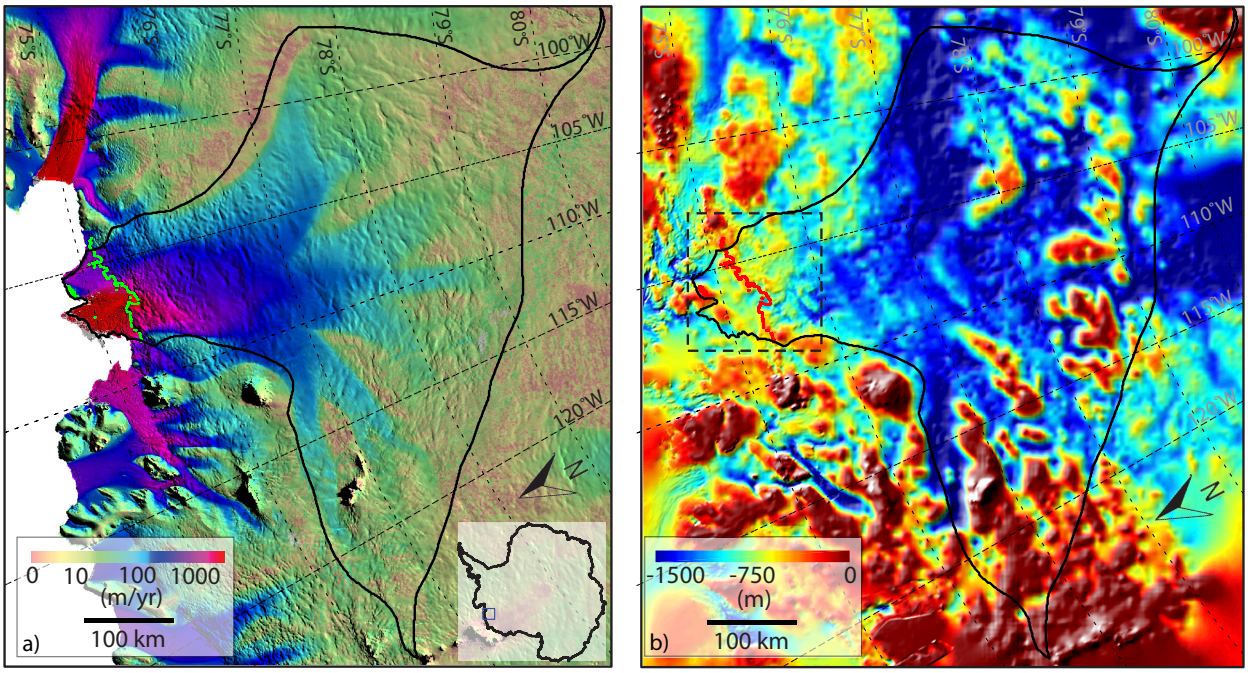

Figure 1.5: Thwaites Glacier, West Antarctica. a) The velocity of Thwaites Glacier and its location in Antarctica (*Rignot et al.*, 2011a). b) The bed elevation of Thwaites Glacier (*Morlighem et al.*, 2013; *Millan et al.*, 2017).

There are currently two main reasons that initialize the dynamical changes of TG, ice shelf melting and calving. In the past few decades, the warm Circumpolar Deep Water (CDW) is able to intrude into the ASE sector due to changes in the wind pattern (*Spence et al.*, 2014; *Scambos et al.*, 2017). This warm water intrusion then enhanced the ice shelf melt under the ice shelf of TG. This process thins the ice shelf, reduces the buttressing to grounded ice sheet and leads to the speed up of TG. Calving has a similar impact on TG. By removing the ice shelf directly, calving reduces the buttressing of the ice shelf to the grounded ice sheet and causes the retreat of TG.

Once the dynamical changes are initiated, the further retreat and mass loss of TG is determined by the bed topography according to MISI. The bed configuration of TG is a typical example for MISI with large area of retrograde bed (Fig. 1.5b). The large width of TG also means the lateral drag that can stabilize the glacier is small. Therefore, an initial speed up and grounding line retreat of TG could trigger further speed up and retreat of the glacier. Some previous modeling studies have suggested that the irreversible retreat of TG may already be underway (*Joughin et al.*, 2014; *Feldmann and Levermann*, 2015)

1.6 Overview of This Dissertation

Due to the rapid changes in the past two decades and the vulnerable bed configuration that favors sustained retreat, TG might be one of the largest contributors in global sea level rise. The ability to simulate the behavior of TG and make reliable projections is therefore necessary. In this thesis, we use state-of-the-art numerical models to model calving of TG and its response to enhanced ice shelf melting.

In the second chapter, we give a description of ice sheet dynamics. We explain in detail the conservation laws of mass, momentum and energy of an ice sheet system and their boundary conditions. We also show the different formulations for both the full-Stokes model and other simplified models of the momentum balance equations. After that, we introduce the inversion method, which is used to infer unknown parameters to ensure that our modeled results match observations.

In the third chapter, we provide a brief introduction of how the ice flow problem is solved numerically. We first explain the numerical solution sequence of the problem. Then we explain the numerical implementation of the governing equations using the finite element method. In the last, we present the validation of our model on benchmark experiments.

In the fourth chapter, we describe our work done in modeling the calving of TG. We first give a brief introduction about calving and the datasets we are using. Then we explain how to combine the ice flow model with a linear elastic fracture mechanics (LEFM) model to simulate the propagation of crevasses in TG. After that, we present our modeling results on crevasse propagation on TG under different scenarios. We then analyze the cause of crevasse propagation and conditions that favor crevasse grow.

In the fifth chapter, we present another modeling work we conducted in simulating the response of TG under enhanced ice shelf melting with various model configurations. We setup our experiment with different ice flow models and different ice shelf melt scenarios based on observations and ocean modeling results. We then show the grounding line migration and mass loss of TG in 100 years under these scenarios. We discuss the difference among different model parameterizations and the stability of TG under enhanced ice shelf melting.

In the last chapter, we summarize this thesis and discuss the limitations and implications for potential future works.

Chapter 2

Ice Sheet Dynamics

In this chapter, we illustrate the physics of ice sheet dynamics. Firstly, we describe the mass balance equations. Secondly, we then discuss the momentum balance equations and their common approximations in the numerical modeling of ice sheets. Thirdly, we present the energy balance of an ice sheet system. Finally, we introduce the inverse method that we used to estimate unknown parameters.

2.1 Mass Balance

2.1.1 Mass Balance Equations

The general law of mass conservation is:

$$\frac{\partial \rho}{\partial t} + \nabla \cdot \rho \boldsymbol{v} = \dot{s} \tag{2.1}$$

where ρ is the density of a material, t is time, $\boldsymbol{v}$ is the velocity vector and $\dot{s}$ is the net rate of mass production (source minus sink).

When applying this law to ice sheets, we assume the net production of ice only happens at the surface (through surface melting and precipitation) and the base (through ice shelf melting and seawater refreeze). Therefore, the term $\dot{s}$ would only exist in boundary conditions and the conservation of mass for the interior of an ice sheet becomes:

$$\frac{\partial \rho}{\partial t} + \nabla \cdot \rho \boldsymbol{v} = 0 \tag{2.2}$$

Moreover, in ice sheet models, the flow of ice is treated as an incompressible flow that satisfies:

$$\frac{d\rho}{dt} = \frac{\partial \rho}{\partial t} + \boldsymbol{v} \nabla \cdot \rho = 0 \tag{2.3}$$

This assumption does not hold at the surface snow and firn layer where the density is much smaller than ice because of the presence of air bubbles. However, the depth of this layer is small ($60 \sim 70$ m), compared to the thickness of an ice sheet that can reach several thousand of meters. Within the ice body, the density of ice can be affected by temperature and pressure. Cold temperature and high pressure within ice sheets both act to increase ice density. Observations, however, have shown that their influence is small. In the mid-depth of ice sheets, where both low temperature and high pressure prevail, ice density is at 923 kg m^{-3}, which is 0.65% more than the usually applied ice density of 917 kg m^{-3}. Therefore, incompressibility is a reasonable assumption for ice sheets (*Hooke*, 2005; *Cuffey and Paterson*, 2010). Combine Eq. 2.2 and Eq. 2.3, the mass conservation equation of ice is simplified to:

$$\nabla \cdot \boldsymbol{v} = 0 \tag{2.4}$$

2.1.2 Boundary Conditions

Using the net production term $\dot{s}$ in Eq. 2.1, we can define the kinematic boundary conditions for the surface and base of an ice sheet.

At the surface, the evolution of surface elevation can be described as:

$$\frac{\partial s}{\partial t} + u_s \frac{\partial s}{\partial x} + v_s \frac{\partial s}{\partial y} - w_s = \dot{M}_s \tag{2.5}$$

where s is the surface elevation, u_s, v_s and w_s are the surface ice velocity and $\dot{M}_s$ is the surface mass balance.

At the base of grounded ice, the ice bottom elevation satisfies the non-penetration condition and is the same as the bedrock elevation unless the ice becomes floating. At the base of ice shelf, we can have similar boundary condition as the surface:

$$\frac{\partial b}{\partial t} + u_b \frac{\partial b}{\partial x} + v_b \frac{\partial b}{\partial y} - w_b = \dot{M}_b \tag{2.6}$$

where b is the ice bottom elevation, u_b, v_b and w_b are the basal ice velocity and $\dot{M}_b$ is the basal mass balance.

2.2 Momentum Balance

2.2.1 Momentum Balance Equations

In a closed system, momentum is conserved according to Newton's laws of motion. Gravity is the only body force that acts on ice sheets (Coriolis force is negligible in the case of ice

flow). In this system, the conservation of momentum can be written as:

$$\rho \frac{d\boldsymbol{v}}{dt} = \nabla \cdot \boldsymbol{\sigma} + \rho \boldsymbol{g} \tag{2.7}$$

where σ is the stress tensor of ice and $\boldsymbol{g}$ is the gravitational acceleration.

The acceleration term $\rho \frac{d\boldsymbol{v}}{dt}$ is small in ice sheets compared to the other terms even in extreme cases (*Reist*, 2005). Therefore, in the general case, this term can be neglected and the momentum balance equation becomes:

$$\nabla \cdot \boldsymbol{\sigma} + \rho \boldsymbol{g} = 0 \tag{2.8}$$

2.2.2 Ice Constitutive Law

As discussed in section 2.1.1, ice can be treated as an incompressible fluid. With the incompressibility, the stress tensor of ice can be decomposed to a deviatoric stress term and a pressure term:

$$\boldsymbol{\sigma} = \boldsymbol{\sigma}' - p\mathbf{I} \tag{2.9}$$

where $\boldsymbol{\sigma}'$ is the deviatoric stress tensor, p is the pressure and $\mathbf{I}$ is the identity matrix.

Despite the incompressibility, ice is also treated as a perfect isotropic viscous material. Such a material satisfies a constitutive relation between deviatoric stress and strain rate:

$$\boldsymbol{\sigma}' = 2\mu\dot{\boldsymbol{\epsilon}} \tag{2.10}$$

where μ is ice viscosity and $\dot{\epsilon}$ is the strain rate.

Glen's flow law states that the strain rate and the stress of ice follows a power-law relation (*Glen*, 1955):

$$\dot{\epsilon}_e = \left(\frac{\sigma_e^{'}}{B}\right)^n \tag{2.11}$$

where B is the ice hardness and n is a parameter, usually taken as 3 (*Cuffey and Paterson*, 2010). $\dot{\epsilon}_e$ and $\sigma_e^{'}$ are the second invariant of the strain rate and deviatoric stress:

$$\begin{cases} \dot{\epsilon}_e = \dfrac{1}{2}(\dot{\epsilon}_{xx}^2 + \dot{\epsilon}_{yy}^2 + \dot{\epsilon}_{zz}^2) + \dot{\epsilon}_{xy}^2 + \dot{\epsilon}_{xz}^2 + \dot{\epsilon}_{yz}^2 \\ \sigma_e = \dfrac{1}{2}(\sigma_{xx}^2 + \sigma_{yy}^2 + \sigma_{zz}^2) + \sigma_{xy}^2 + \sigma_{xz}^2 + \sigma_{yz}^2 \end{cases} \tag{2.12}$$

Glen's flow law was extended to cover multi-axial states of stress by *Nye* (1957a). It is assumed that each strain rate component is proportional to its corresponding deviatoric stress component:

$$\dot{\boldsymbol{\epsilon}} = \lambda \boldsymbol{\sigma}^{'} \tag{2.13}$$

combining with Eq. 2.12, we can get:

$$\dot{\epsilon_e} = \lambda \sigma_e^{'} \tag{2.14}$$

Then by applying Glen's flow law (equation 2.11) to equation 2.14, we have:

$$\lambda = \frac{\sigma_e^{'n-1}}{B^n} \tag{2.15}$$

Thus, using Eq. 2.13:

$$\dot{\boldsymbol{\epsilon}} = \frac{\sigma_e^{'n-1}}{B^n} \boldsymbol{\sigma}^{'} \tag{2.16}$$

Substituting $\sigma_e^{'}$ by $\dot{\epsilon_e}$ using Glen's flow law again, we get:

$$\dot{\boldsymbol{\epsilon}} = \frac{2\dot{\epsilon_e}^{\frac{n-1}{n}}}{B}\boldsymbol{\sigma}^{'} \tag{2.17}$$

Finally, after combining Eq. 2.10 and Eq. 2.17, the viscosity of ice can be identified as:

$$\mu = \frac{B}{2\dot{\epsilon_e}^{\frac{n-1}{n}}} \tag{2.18}$$

The ice hardness B is mostly affected by temperature. Ice is softer when temperature is higher. In practice, the value of B is usually interpolated from *in-situ* observations (*Cuffey and Paterson*, 2010).

2.2.3 Boundary Conditions

The boundary conditions of the mass and momentum balance equations are shown in Fig. 2.1. At the ice-atmosphere interface, a stress-free boundary is applied as the atmospheric pressure is small compared to the ice lithostatic pressure:

$$\boldsymbol{\sigma} \cdot \boldsymbol{n} = \mathbf{0} \tag{2.19}$$

where $\boldsymbol{n}$ is the unit normal vector pointing outward.

At the ice-bedrock interface, a friction law linking basal velocity and basal stress is applied. There are several proposed friction laws and their general form is (*Weertman*, 1957; *Budd et al.*, 1979; *Gagliardini et al.*, 2007):

$$\boldsymbol{\tau_b} = -CN^q \|\boldsymbol{v}_b\|^{1/p-1}\boldsymbol{v}_b \tag{2.20}$$

where $\boldsymbol{\tau_b}$ is the basal drag, $\boldsymbol{v}_b$ is the basal velocity, $N = \rho_i g H + \rho_w g b$ is the effective pressure at the base (ρ_i is ice density, H is ice thickness and ρ_w is water density), C, p, and q are all constant parameters.

In this thesis, we will be using two linear friction laws, one considers the effective pressure and one does not. They are both special cases from the above general equation with $q = 0, p = 1$ and $q = 1, p = 1$, respectively. The basal friction coefficient, C, is computed through inversion so that modeled surface velocity matches observations, which will be discussed in more detail in section 2.4.

At the ice-ocean interface, the normal stress of ice is assumed to be balanced by water pressure:

$$\boldsymbol{\sigma} \cdot \boldsymbol{n} = \rho_w g z \boldsymbol{n} \tag{2.21}$$

where z is the vertical coordinate with sea level at $z = 0$.

At the boundary of the domain of our models, Dirichlet conditions are applied. The ice surface velocity is constrained to be equal to the observed surface ice velocity:

$$\boldsymbol{u} = \boldsymbol{u}_{obs} \tag{2.22}$$

2.2.4 Full-Stokes Model

If we combine the equations of mass conservation (equation 2.4) and momentum conservation (Eq. 2.8), we get a model that solves for the ice velocity and pressure field. Expressing this

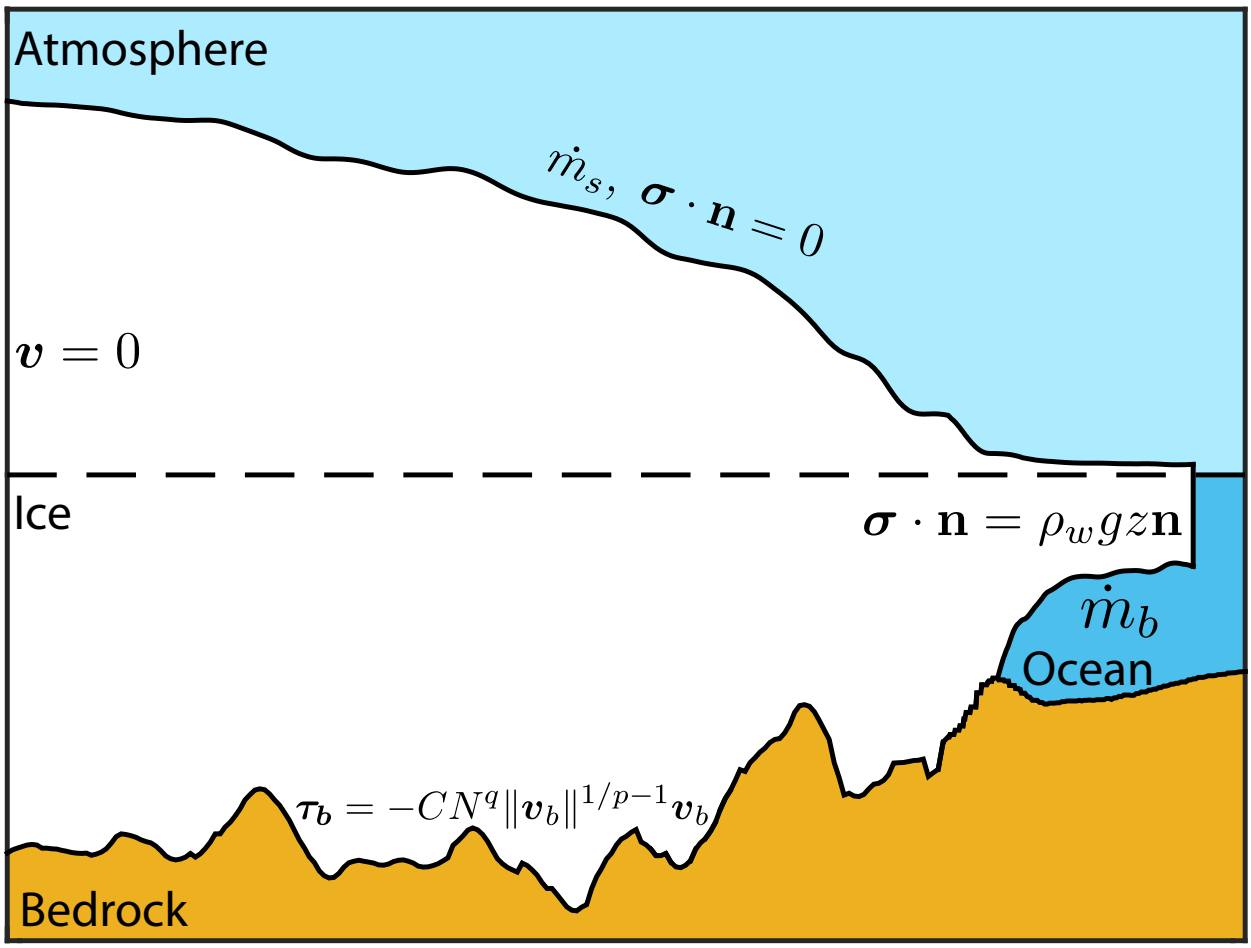

Figure 2.1: Schematic boundary conditions for the mass balance and the momentum balance equations in 2D

model in a Cartesian coordinate system, we get the full-Stokes (FS) model:

$$\begin{cases} \frac{\partial}{\partial x}\left(2\mu\frac{\partial u}{\partial x}\right)+\frac{\partial}{\partial y}\left(\mu\frac{\partial u}{\partial y}+\mu\frac{\partial v}{\partial x}\right)+\frac{\partial}{\partial z}\left(\mu\frac{\partial u}{\partial z}+\mu\frac{\partial w}{\partial x}\right)-\frac{\partial p}{\partial x}=0 \\ \frac{\partial}{\partial x}\left(\mu\frac{\partial u}{\partial y}+\mu\frac{\partial v}{\partial x}\right)+\frac{\partial}{\partial y}\left(2\mu\frac{\partial v}{\partial y}\right)+\frac{\partial}{\partial z}\left(\mu\frac{\partial w}{\partial y}+\mu\frac{\partial v}{\partial z}\right)-\frac{\partial p}{\partial y}=0 \\ \frac{\partial}{\partial x}\left(\mu\frac{\partial u}{\partial z}+\mu\frac{\partial w}{\partial x}\right)+\frac{\partial}{\partial y}\left(\mu\frac{\partial v}{\partial z}+\mu\frac{\partial w}{\partial y}\right)+\frac{\partial}{\partial z}\left(2\mu\frac{\partial w}{\partial z}\right)-\frac{\partial p}{\partial z}-\rho_i g=0 \\ \frac{\partial u}{\partial x}+\frac{\partial v}{\partial y}+\frac{\partial w}{\partial z}=0 \end{cases} \tag{2.23}$$

The FS model does not make assumptions on the stress field, but it is computationally expensive. Because of the high requirement of computational resources, simplified models are always used in the ice sheet modeling community. There are three widely used approxima-

tions: the Higher-Order (HO) approximation, the Shelfy-Stream Approximation (SSA) and the Shallow Ice Approximation (SIA).

2.2.5 Higher-Order Approximation

The HO approximation is derived and proposed by *Blatter* (1995) and *Pattyn* (2003). In HO, two main assumptions are made from the FS model. First, the horizontal gradients of vertical velocity are neglected:

$$\frac{\partial w}{\partial x} \ll \frac{\partial u}{\partial z}, \qquad \frac{\partial w}{\partial y} \ll \frac{\partial v}{\partial z} \tag{2.24}$$

Second, the bridging effect is neglected (Fig. 2.2). In a bridge, the weight of the arches is supported by the abutment, which means the vertical normal stresses are higher than the lithostatic pressure under the abutment. These variations in vertical normal stresses can then alter the shear stresses in the bridge. *van der Veen and Whillans* (1989) stated that in small scale, this bridging effect can be important for glaciers. By neglecting the bridging effect:

$$\frac{\partial \sigma_{xz}}{\partial x} \ll \rho g, \qquad \frac{\partial \sigma_{yz}}{\partial y} \ll \rho g \tag{2.25}$$

The vertical normal stress of ice would be equal to the overburden ice pressure:

$$\frac{\partial \sigma_{zz}}{\partial z} - \rho g = 0 \tag{2.26}$$

The vertical velocity w is also decoupled from the governing equations with these two assumptions:

$$\begin{cases} \frac{\partial}{\partial x}\Big(4\mu\frac{\partial u}{\partial x}+2\mu\frac{\partial v}{\partial y}\Big)+\frac{\partial}{\partial y}\Big(\mu\frac{\partial u}{\partial y}+\mu\frac{\partial v}{\partial x}\Big)+\frac{\partial}{\partial z}\Big(\mu\frac{\partial u}{\partial z}\Big)=\rho g\frac{\partial s}{\partial x} \\ \frac{\partial}{\partial x}\Big(\mu\frac{\partial u}{\partial y}+\mu\frac{\partial v}{\partial x}\Big)+\frac{\partial}{\partial y}\Big(4\mu\frac{\partial v}{\partial y}+2\mu\frac{\partial u}{\partial x}\Big)+\frac{\partial}{\partial z}\Big(\mu\frac{\partial v}{\partial z}\Big)=\rho g\frac{\partial s}{\partial y} \end{cases} \tag{2.27}$$

In the vertical direction, the momentum balance equation is reduced to:

$$\frac{\partial}{\partial z}(2\mu\frac{\partial w}{\partial z})-\frac{\partial p}{\partial z}-\rho g=0 \tag{2.28}$$

The vertical velocity, w, can then be recovered through incompressibility.

2.2.6 Shelfy-Stream Approximation

The second widely used simplified model is the Shelfy-Stream Approximation (SSA) model, which was proposed by *Morland* (1987) and *MacAyeal* (1989). With both the assumptions made in the HO model, SSA makes the further assumption that the vertical shear is negligible:

$$\dot{\epsilon}_{xz}=0, \qquad \dot{\epsilon}_{yz}=0 \tag{2.29}$$

With this assumption, the original 3D model is reduced to a depth-averaged 2D model. The governing equations for the SSA model are:

$$\begin{cases} \frac{\partial}{\partial x}\Big(4H\bar{\mu}\frac{\partial u}{\partial x}+2H\bar{\mu}\frac{\partial v}{\partial y}\Big)+\frac{\partial}{\partial y}\Big(H\bar{\mu}\frac{\partial u}{\partial y}+H\bar{\mu}\frac{\partial v}{\partial x}\Big)=\rho gH\frac{\partial s}{\partial x} \\ \frac{\partial}{\partial x}\Big(H\bar{\mu}\frac{\partial u}{\partial y}+H\bar{\mu}\frac{\partial v}{\partial x}\Big)+\frac{\partial}{\partial y}\Big(2H\bar{\mu}\frac{\partial u}{\partial x}+4H\bar{\mu}\frac{\partial v}{\partial y}\Big)=\rho gH\frac{\partial s}{\partial y} \end{cases} \tag{2.30}$$

where $\bar{\mu}$ is the depth-averaged ice viscosity.

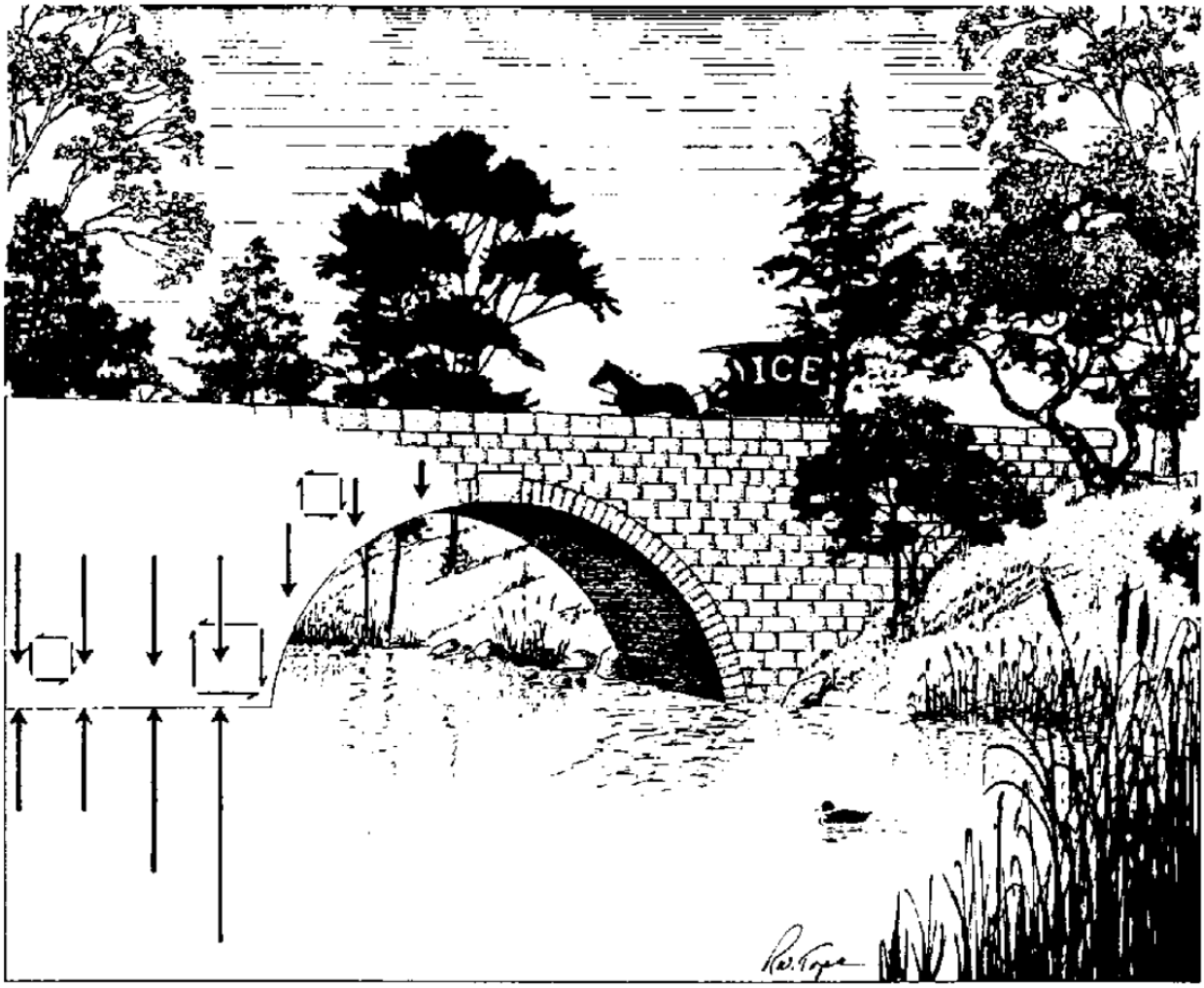

Figure 2.2: The bridging effect: vertical normal stresses is higher than lithostatic pressure under the abutment and lower under the arch (*van der Veen and Whillans*, 1989).

2.2.7 Shallow Ice Approximation

The third simplified model is the Shallow Ice Approximation (SIA) model derived by *Hutter* (1983). This is the simplest and most efficient ice flow model. Unlike SSA, which neglects the vertical shear, SIA assumes that only the vertical shear is important to ice flow and all other components of the stress field are neglected. By applying this assumption, the

governing equations are reduced to a simple form:

$$\begin{cases} \dfrac{\partial}{\partial z}\left(\mu\dfrac{\partial u}{\partial z}\right) = \rho g\dfrac{\partial s}{\partial x} \\ \dfrac{\partial}{\partial z}\left(\mu\dfrac{\partial v}{\partial z}\right) = \rho g\dfrac{\partial s}{\partial y} \end{cases} \tag{2.31}$$

The SIA model is a semi-analytical model as the ice velocity is locally determined. The velocity is only dependent on ice geometry and not on upstream or downstream velocities. This model is valid for grounded ice with limited sliding, which is true for the majority regions of an ice sheet. However, this model breaks down in the key regions of ice sheet, such as grounding line regions or ice shelves. This drawback makes it more suitable for large spatial and temporal scale reconstructions of ice sheets, but not for detailed simulation of specific glaciers with complex geometry on a short temporal scale (*Blatter et al.*, 2010). Therefore, in the following of this thesis, only FS, HO and SSA models are considered.

2.3 Energy Balance

2.3.1 Energy Balance Equations

The viscosity of ice is dependent on ice hardness, which is a function of temperature. Thus, it is crucial to have a realistic temperature field to simulate realistic ice dynamics. However, measuring ice temperature at different depths with high spatial resolution is not possible at present. In practice, the temperature field within an ice body is computed using the energy conservation law with observed surface temperature, geothermal heat flux and ice velocity.

The energy conservation law states that the total energy is constant for an isolated system. According to the Fourier's law, energy balance can be written as:

$$\frac{d}{dt}(\rho c T) = \nabla \cdot (k_{th} \nabla T) + \Phi \tag{2.32}$$

where c is the heat capacity, T is the temperature, k_{th} is the thermal conductivity and Φ is the net energy production.

In the case of an ice sheet, Φ is created through internal deformation heating and can be computed through (*Cuffey and Paterson*, 2010):

$$\Phi = Tr(\boldsymbol{\sigma}\dot{\boldsymbol{\epsilon}}) \tag{2.33}$$

where $Tr()$ is the trace operation of a square matrix.

Moreover, for ice, it is a common and realistic assumption that ρ, c, k_{th} are constant (*Hooke*, 2005). With this assumption, the energy balance equation can be rewritten as:

$$\frac{\partial T}{\partial t} = -\boldsymbol{v} \cdot \nabla T + k_{th} \cdot \Delta T + \frac{\Phi}{\rho c} \tag{2.34}$$

2.3.2 Boundary Conditions

At the ice-atmosphere interface, ice temperature is constrained by observed annual mean surface air temperature:

$$T_s = T_{air} \tag{2.35}$$

This boundary condition is widely used in ice sheet modeling studies because the ice temperature at depth below 15 m in a glacier has limited seasonal variations and is equal to annual

mean air temperature (*Cuffey and Paterson*, 2010; *Hulbe and MacAyeal*, 1999; *Seroussi et al.*, 2013).

At the ice-ocean interface, a heat flux between seawater and ice is imposed, which is assumed to be proportional to the difference between ice temperature and ocean temperature (*Holland and Jenkins*, 1999):

$$k_{th}\nabla T|_b \cdot \boldsymbol{n} = -\rho_w c_{pM}\gamma(T_b - T_{pmp}) \tag{2.36}$$

where T_b is the ice bottom temperature, T_{pmp} is the pressure melting point of ice (assumed to be ocean temperature), c_{pM} is the mixed layer specific heat capacity and γ is the thermal exchange velocity.

At the ice-bedrock interface, ice gains energy from the geothermal heat flux and frictional heating:

$$k_{th}\nabla T|_b \cdot \boldsymbol{n} = G + |\boldsymbol{\tau}_b \cdot \boldsymbol{u}_b| \tag{2.37}$$

where G is the geothermal heat flux.

2.4 Inversion

In the process of ice sheet modeling, there are some necessary ice properties that cannot be obtained from direct observations, such as the basal friction coefficient and the ice hardness. The accuracy of these parameters are, however, critical to model results. Therefore, to model realistic ice sheet dynamics, these parameters need to be computed from known data through inversion. The basic idea of inversion is to find a set of basal friction coefficients and ice

hardness so that modeled results can match direct observations (surface ice velocity). Then this set of parameters is applied to the model to simulate the future evolution of ice sheets.

In the scope of this thesis, we infer the basal friction coefficient, C, (Eq. 2.20) and ice hardness, B, (Eq. 2.18) by matching observed surface velocity (*MacAyeal*, 1992, 1993; *Morlighem et al.*, 2010, 2013). Increases in ice hardness reduces ice velocity, which is the same as increase basal friction coefficient. This indicates that if we infer both ice hardness and basal friction coefficient for grounded ice, the result will not be unique. Therefore, we assume that the temperature computed from the thermal model is correct for grounded ice and only infer B for floating ice.

To match observed surface velocity, we compute a cost function that measures the difference between modeled surface velocity and observed surface velocity:

$$\mathcal{J}(u,v,\alpha) = \int_{\Gamma_s} c_1 \frac{1}{2}\left((u-u_{obs})^2 + (v-v_{obs})^2\right) d\Gamma + \int_{\Gamma_s} c_2 \frac{1}{2} \ln\left(\frac{\sqrt{u^2+v^2}+\epsilon}{\sqrt{u_{obs}^2+v_{obs}^2}+\epsilon}\right)^2 d\Gamma + \int_{\Gamma_b} c_3 \frac{1}{2}\left(\left(\frac{\partial\alpha}{\partial x}\right)^2 + \left(\frac{\partial\alpha}{\partial y}\right)^2\right) d\Gamma \tag{2.38}$$

where u, v and u_{obs}, v_{obs} are the modeled and observed surface velocity in x and y directions, α is the inferred variable (C or B), ϵ is a small number (10^{-8} m/yr) to avoid zero velocity and c_1, c_2 and c_3 are all constants.

In Eq. 2.38, the cost function is determined by three terms. The first term is a measure of the misfit between modeled and observed surface velocity. This term alone favors the match of velocity in fast regions as the mismatch $(u - u_{obs})$ is high in fast regions even when the relative difference is small. To take more account of the slow regions, we add the second logarithm term so that the mismatch is in the same magnitude for both fast and slow speed regions. The third term is a regularization term, which acts to avoid non-physical short-scale

spatial variations of the inferred variable α (*Vogel*, 2002). While doing inversion, we first calibrate c_1 and c_2 so that the first two terms are in the same magnitude. Then, we calibrate c_3 to make sure the modeled velocity is close to observation and α is smooth in space.

With this cost function, we use the adjoint method to compute its gradient to the inferred parameters and apply gradient descent to reduce it. The details of the adjoint method can be found in *Morlighem* (2011).

2.5 Conclusion

In this chapter, we presented an overview of ice sheet dynamics. We illustrated the three conservation laws (mass, momentum and energy) that govern the behavior of ice sheets. For each conservation law, we discussed its general expression, specific assumptions made for ice and its boundary conditions. We also showed that there are several ways to solve the momentum balance equations with varying complexity. The FS model is the most complete model but requires a high amount of computational resources. The HO, SSA and SIA are all models simplified from the FS model and require less resources. Finally, we discussed the use of inversion to infer important parameters that cannot be observed directly.

Chapter 3

Numerical Ice Sheet Modeling

In this chapter, we describe the numerical implementation of the governing equations we introduced in Chapter 2. In the first section, we present the solution sequence for the three conservation laws. Then, in the second section, we briefly explain the finite element method that we use to implement the equations numerically. In the last section, we discuss how we validate our model using model intercomparision projects.

3.1 Solving Sequence of Ice Flow Models

With the three sets of conservation laws and their corresponding boundary and initial conditions, we formed a complete system and are capable to model the evolution of an ice sheet in time. The solving sequence of this system is illustrated in Fig. 3.1 and discussed in detail below.

3.1.1 Thermal Model

Within the scope of this thesis, we will only simulate the evolution of an ice sheet in 100 years. In this time scale, it is reasonable to assume that the internal temperature field stays constant. Therefore, we compute the thermal regime of an ice sheet first and keep it fixed in the entire transient simulation to reduce computational cost.

Before computing the thermal regime from energy balance, we first do inversion for the basal friction coefficient over grounded ice and ice hardness over floating ice with a default ice temperature field. Then we assume the modeled ice velocity is the correct ice velocity and use it to compute the temperature field through:

$$\frac{\partial T}{\partial t} = -\boldsymbol{v} \cdot \nabla T + k_{th} \cdot \Delta T + \frac{\Phi}{\rho c} \tag{3.1}$$

constrained by boundary conditions:

$$\begin{cases} T_s = T_{air} & \text{Ice upper surface} \\ k_{th} \nabla T|_b \cdot \boldsymbol{n} = G + |\boldsymbol{\tau}_b \cdot \boldsymbol{u}_b| & \text{Grounded ice sheet bottom} \\ k_{th} \nabla T|_b \cdot \boldsymbol{n} = -\rho_w c_{pM} \gamma (T_b - T_{pmp}) & \text{Ice shelf bottom} \end{cases} \tag{3.2}$$

3.1.2 Mechanical Model

After the thermal regime is computed, inversion of the basal friction coefficient and the ice hardness is conducted again to better match observations. After this inversion, we can use

the conservation of momentum and mass to compute the velocity and pressure field of ice:

$$\begin{cases} \nabla \cdot \boldsymbol{\sigma} + \rho \boldsymbol{g} = 0 \\ \nabla \cdot \boldsymbol{v} = 0 \\ \boldsymbol{\sigma}' = 2\mu\dot{\boldsymbol{\epsilon}} \end{cases} \tag{3.3}$$

constrained by boundary conditions:

$$\begin{cases} \boldsymbol{\sigma} \cdot \boldsymbol{n} = 0 & \text{Ice sheet surface} \\ \boldsymbol{\tau_b} = -CN^q \|\boldsymbol{v}_b\|^{1/p-1} \boldsymbol{v}_b & \text{Grounded ice sheet bottom} \\ \boldsymbol{\sigma} \cdot \boldsymbol{n} = \rho_w g z \boldsymbol{n} & \text{Ice shelf bottom and ice front} \\ \boldsymbol{u} = \boldsymbol{u}_{obs} & \text{Domain boundary} \end{cases} \tag{3.4}$$

For the FS model, a modification of the above boundary conditions is needed. During the solving process, the ice shelf bottom elevation, $z_b(t)$, is unknown when applying the boundary condition at ice shelf bottom. A replacement with $z_b(t-dt)$, with dt the time step, produces large vertical velocities that destabilize the system (*Durand et al.*, 2009a). Therefore, a shelf dampening term based on ice velocity and geometry is added to $z_b(t-dt)$ to approximate $z_b(t)$:

$$z_b(t) = z_b(t-dt) + \boldsymbol{v} \cdot \mathbf{n}\sqrt{1 + (\partial z_b(t-dt)/\partial x)^2}dt \tag{3.5}$$

For HO and SSA, this dampening term is not necessary because hydrostatic equilibrium is an inherent assumption.

Since the equations are nonlinear, the solving procedure is an iterative process. Once the velocity field is computed, it is used to compute a new viscosity field, which in turn is used to

computed a new velocity field. The system is considered solved when the computed velocity converges to a unique solution.

3.1.3 Mass Transport Model

When a converged solution of velocity is found, we evolve the model forward in time by updating the geometry of an ice sheet through a mass transport model.

For HO and SSA, because hydrostatic equilibrium is assumed, the mass transport model updates the ice thickness field first through:

$$\frac{\partial H}{\partial t} + \nabla \cdot H\bar{\boldsymbol{v}} = \dot{M}_s - \dot{M}_b \tag{3.6}$$

Then the model computes the surface and bottom elevation using the flotation criterion:

$$\begin{cases} \left.\begin{array}{l} s = H\dfrac{\rho_w - \rho_i}{\rho_w} \\ b = -H\dfrac{\rho_i}{\rho_w} \end{array}\right\} & h < -r\dfrac{\rho_w}{\rho_i} \\ \left.\begin{array}{l} s = H - r \\ b = r \end{array}\right\} & h \geq -r\dfrac{\rho_w}{\rho_i} \end{cases} \tag{3.7}$$

For FS, the upper and lower surface is treated as free surfaces and the computed velocity is directly applied to the boundary conditions of the mass balance equations (equation 2.5 and 2.6):

$$\begin{cases} \dfrac{\partial s}{\partial t} + u_s\dfrac{\partial s}{\partial x} + v_s\dfrac{\partial s}{\partial y} - w_s = \dot{M}_s & \text{upper surface} \\ \dfrac{\partial b}{\partial t} + u_b\dfrac{\partial b}{\partial x} + v_b\dfrac{\partial b}{\partial y} - w_b = \dot{M}_b & \text{lower surface} \end{cases} \tag{3.8}$$

under the constrain that ice cannot penetrate the bedrock:

$$b \geq r \tag{3.9}$$

where r is the elevation of the bedrock.

3.1.4 Grounding Line Migration

After updating the geometry of ice, the grounding line position may also change, which affects the boundary conditions at the lower surface. The methods for migrating the grounding line are different between FS and the simplified models.

For HO and SSA, the grounding line position is solely controlled by hydrostatic equilibrium. Therefore, the new grounding line position is actually already computed in the mass transport model when the flotation criterion is applied. Ice is considered to be floating if the ice bottom is higher than bedrock and grounded otherwise.

For FS, the assumption of hydrostatic equilibrium is not applied and the grounding line position is computed by solving a contact problem (*Nowicki and Wingham*, 2008; *Durand et al.*, 2009b). If the ice bottom is higher than bedrock, the ice would be considered as floating as in the simplified models. However, if the ice bottom is equal to the bedrock, the normal stress, $\sigma_{nn} = \boldsymbol{n} \cdot (\boldsymbol{\sigma} \cdot \boldsymbol{n})$, and water pressure, p_w, will be compared at the base. The ice will also be considered as floating if the water pressure is higher than the normal stress.

Now, we run the mechanical model again with the new ice geometry and grounding line position to compute a new velocity and pressure field at this new time step and iterate this process until the model is run for our desired time span.

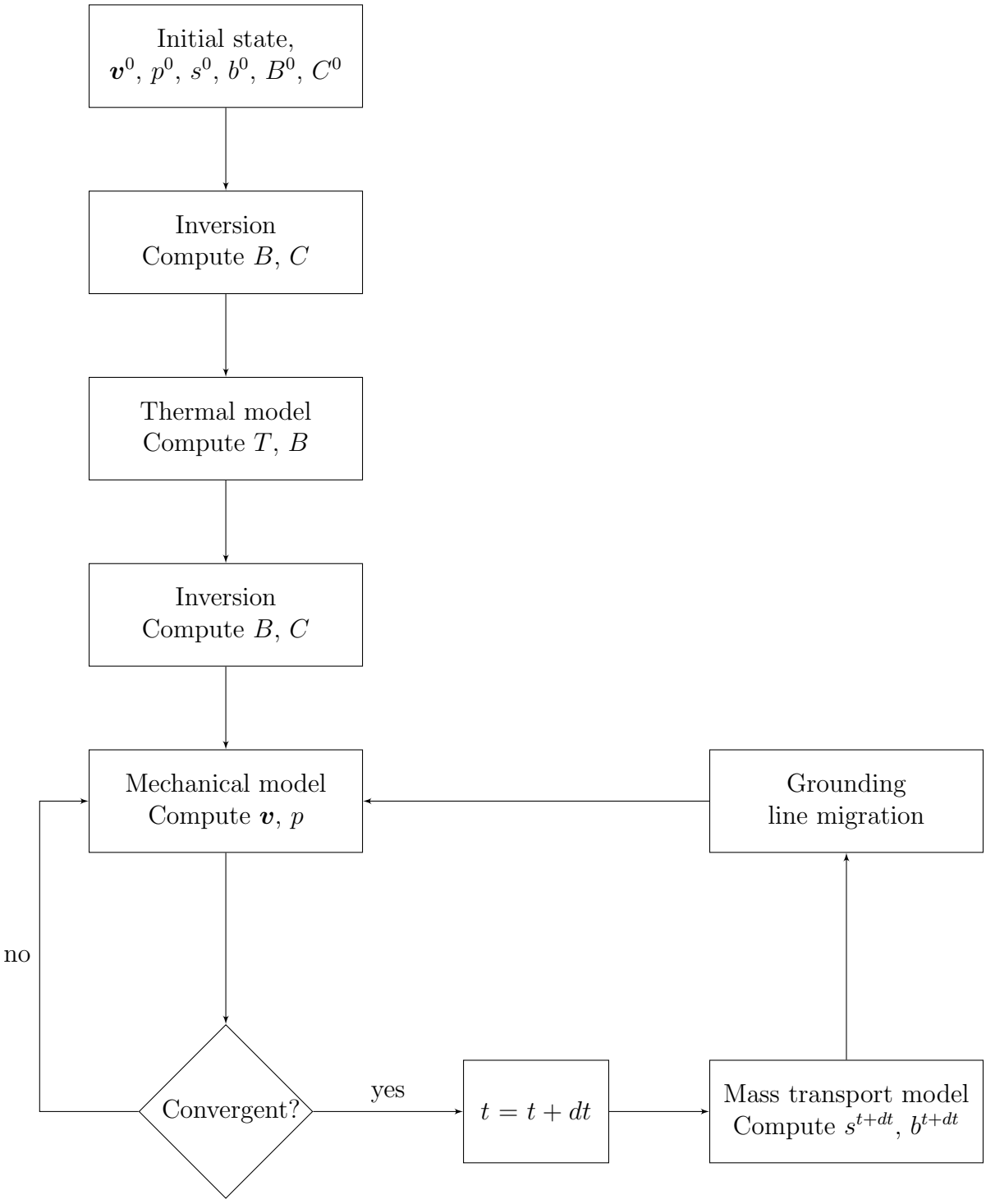

Figure 3.1: Schematic solution sequence of a transient ice flow model.

3.2 Finite Element Method

The above equations are implemented with the finite element method (FEM) numerically. The basic idea of FEM is to discretize a domain into smaller, simpler elements. Simple equations are built for each element and then they are assembled together to model the entire domain (*Zienkiewicz and Codina*, 1995). For a given set of partial differential equations:

$$L\boldsymbol{u} - f = 0 \tag{3.10}$$

The goal of FEM is to find a set of solution $\widetilde{\boldsymbol{u}}$ that minimizes the residual of these equations:

$$R = L\widetilde{\boldsymbol{u}} - f \tag{3.11}$$

using the weak formulation, which is the integration form of the above differential equations:

$$\int_{\Omega} R \mathrm{d}\Omega = 0 \tag{3.12}$$

In general, there is more than one degree of freedom to solve. Therefore, the residual is weighted by a shape function ϕ_i so that every degree of freedom will have one equation:

$$\int_{\Omega} \phi_i R \mathrm{d}\Omega = 0, \quad i = 1, 2...N \tag{3.13}$$

In numerical ice sheet modeling, we first convert the conservation laws into their weak formulation. Then we use the Galerkin discretization method to get equations for each element. Finally, we assemble all elements to build global equations to solve. Here, we use the FS mechanical model as an example to show how FEM is implemented.

3.2.1 Weak Formulation

As illustrated in section 2.2.4, the FS mechanical model is:

$$\begin{cases} \frac{\partial}{\partial x}\Big(2\mu\frac{\partial u}{\partial x}\Big)+\frac{\partial}{\partial y}\Big(\mu\frac{\partial u}{\partial y}+\mu\frac{\partial v}{\partial x}\Big)+\frac{\partial}{\partial z}\Big(\mu\frac{\partial u}{\partial z}+\mu\frac{\partial w}{\partial x}\Big)-\frac{\partial p}{\partial x}=0 \\ \frac{\partial}{\partial x}\Big(\mu\frac{\partial u}{\partial y}+\mu\frac{\partial v}{\partial x}\Big)+\frac{\partial}{\partial y}\Big(2\mu\frac{\partial v}{\partial y}\Big)+\frac{\partial}{\partial z}\Big(\mu\frac{\partial w}{\partial y}+\mu\frac{\partial v}{\partial z}\Big)-\frac{\partial p}{\partial y}=0 \\ \frac{\partial}{\partial x}\Big(\mu\frac{\partial u}{\partial z}+\mu\frac{\partial w}{\partial x}\Big)+\frac{\partial}{\partial y}\Big(\mu\frac{\partial v}{\partial z}+\mu\frac{\partial w}{\partial y}\Big)+\frac{\partial}{\partial z}\Big(2\mu\frac{\partial w}{\partial z}\Big)-\frac{\partial p}{\partial z}-\rho_i g=0 \\ \frac{\partial u}{\partial x}+\frac{\partial v}{\partial y}+\frac{\partial w}{\partial z}=0 \end{cases} \tag{3.14}$$

To convert this equation into its weak formulation, we need to first multiply the equations by the shape functions (ϕ_x, ϕ_y, ϕ_z for velocity and ψ for pressure) and integrate over the domain Ω:

$$\begin{aligned} &\int_\Omega\Big(\frac{\partial}{\partial x}\Big(2\mu\frac{\partial u}{\partial x}\Big)+\frac{\partial}{\partial y}\Big(\mu\frac{\partial u}{\partial y}+\mu\frac{\partial v}{\partial x}\Big)+\frac{\partial}{\partial z}\Big(\mu\frac{\partial u}{\partial z}+\mu\frac{\partial w}{\partial x}\Big)-\frac{\partial p}{\partial x}\Big)\phi_x d\Omega \\ &+\int_\Omega\Big(\frac{\partial}{\partial x}\Big(\mu\frac{\partial u}{\partial y}+\mu\frac{\partial v}{\partial x}\Big)+\frac{\partial}{\partial y}\Big(2\mu\frac{\partial v}{\partial y}\Big)+\frac{\partial}{\partial z}\Big(\mu\frac{\partial w}{\partial y}+\mu\frac{\partial v}{\partial z}\Big)-\frac{\partial p}{\partial y}\Big)\phi_y d\Omega \\ &+\int_\Omega\Big(\frac{\partial}{\partial x}\Big(\mu\frac{\partial u}{\partial z}+\mu\frac{\partial w}{\partial x}\Big)+\frac{\partial}{\partial y}\Big(\mu\frac{\partial v}{\partial z}+\mu\frac{\partial w}{\partial y}\Big)+\frac{\partial}{\partial z}\Big(2\mu\frac{\partial w}{\partial z}\Big)-\frac{\partial p}{\partial z}\Big)\phi_z d\Omega \\ &-\int_\Omega\Big(\frac{\partial u}{\partial x}+\frac{\partial v}{\partial y}+\frac{\partial w}{\partial z}\Big)\psi d\Omega=\int_\Omega\rho_i g\phi_z d\Omega \end{aligned} \tag{3.15}$$

After applying integration by parts and the divergence theorem, the above equation can be rewritten as:

$$\begin{aligned} &\int_\Omega\Big(2\mu\frac{\partial u}{\partial x}\Big)\frac{\partial\phi_x}{\partial x}+\Big(\mu\frac{\partial u}{\partial y}+\mu\frac{\partial v}{\partial x}\Big)\frac{\partial\phi_x}{\partial y}+\Big(\mu\frac{\partial u}{\partial z}+\mu\frac{\partial w}{\partial x}\Big)\frac{\partial\phi_x}{\partial z}-p\frac{\partial\phi_x}{\partial x} \\ &+\Big(\mu\frac{\partial u}{\partial y}+\mu\frac{\partial v}{\partial x}\Big)\frac{\partial\phi_y}{\partial x}+\Big(2\mu\frac{\partial v}{\partial y}\Big)\frac{\partial\phi_y}{\partial y}+\Big(\mu\frac{\partial w}{\partial y}+\mu\frac{\partial v}{\partial z}\Big)\frac{\partial\phi_y}{\partial z}-p\frac{\partial\phi_y}{\partial y} \\ &+\Big(\mu\frac{\partial u}{\partial z}+\mu\frac{\partial w}{\partial x}\Big)\frac{\partial\phi_z}{\partial x}+\Big(\mu\frac{\partial v}{\partial z}+\mu\frac{\partial w}{\partial y}\Big)\frac{\partial\phi_z}{\partial y}+\Big(2\mu\frac{\partial w}{\partial z}\Big)\frac{\partial\phi_z}{\partial z}-p\frac{\partial\phi_z}{\partial z} \\ &-\Big(\frac{\partial u}{\partial x}+\frac{\partial v}{\partial y}+\frac{\partial w}{\partial z}\Big)\psi d\Omega+\int_\Gamma\phi\boldsymbol{n}\cdot\boldsymbol{\sigma}d\Gamma=\int_\Omega\rho_i g\phi_z d\Omega \end{aligned} \tag{3.16}$$

where the term $\int_\Gamma \phi \boldsymbol{n} \cdot \boldsymbol{\sigma} d\Gamma$ includes all the Neumann boundary conditions described in Eq. 3.4.

3.2.2 Galerkin Discretization

The above weak formulation integrates the differential equations over the whole domain. To apply FEM, we need to discretize the domain into small elements and to find solutions for each node of these elements. By assuming equation 3.15 is true for all elements, we have for each element:

$$\begin{aligned}
&\int_\Omega \Big(2\mu\frac{\partial u}{\partial x}\Big)\frac{\partial \phi_{ix}}{\partial x} + \Big(\mu\frac{\partial u}{\partial y} + \mu\frac{\partial v}{\partial x}\Big)\frac{\partial \phi_{ix}}{\partial y} + \Big(\mu\frac{\partial u}{\partial z} + \mu\frac{\partial w}{\partial x}\Big)\frac{\partial \phi_{ix}}{\partial z} - p\frac{\partial \phi_{ix}}{\partial x} \\
&+\Big(\mu\frac{\partial u}{\partial y} + \mu\frac{\partial v}{\partial x}\Big)\frac{\partial \phi_{iy}}{\partial x} + \Big(2\mu\frac{\partial v}{\partial y}\Big)\frac{\partial \phi_{iy}}{\partial y} + \Big(\mu\frac{\partial w}{\partial y} + \mu\frac{\partial v}{\partial z}\Big)\frac{\partial \phi_{iy}}{\partial z} - p\frac{\partial \phi_{iy}}{\partial y} \\
&+\Big(\mu\frac{\partial u}{\partial z} + \mu\frac{\partial w}{\partial x}\Big)\frac{\partial \phi_{iz}}{\partial x} + \Big(\mu\frac{\partial v}{\partial z} + \mu\frac{\partial w}{\partial y}\Big)\frac{\partial \phi_{iz}}{\partial y} + \Big(2\mu\frac{\partial w}{\partial z}\Big)\frac{\partial \phi_{iz}}{\partial z} - p\frac{\partial \phi_{iz}}{\partial z} \\
&-\Big(\frac{\partial u}{\partial x} + \frac{\partial v}{\partial y} + \frac{\partial w}{\partial z}\Big)\psi_i d\Omega + \int_\Gamma \phi_i \boldsymbol{n} \cdot \boldsymbol{\sigma} d\Gamma = \int_\Omega \rho_i g \phi_{iz} d\Omega
\end{aligned} \tag{3.17}$$

Then, we assume the solution of the problem can be approximated by a linear combination of the shape functions and the unknowns:

$$\begin{cases}
u = \sum_{j=1}^{M_u} u_j \phi_{jx} + \sum_{j=1}^{N_u} u_j \phi_{jx} \\
v = \sum_{j=1}^{M_v} v_j \phi_{jy} + \sum_{j=1}^{N_v} v_j \phi_{jy} \\
w = \sum_{j=1}^{M_w} u_j \phi_{jz} + \sum_{j=1}^{N_w} w_j \phi_{jz} \\
p = \sum_{j=1}^{N_p} p_j \psi_j
\end{cases} \tag{3.18}$$

where M_u, M_v and M_w are the unknowns with Dirichlet boundary conditions and N_u, N_v, N_w and N_p are the remaining unknowns. For simplicity, we assume all the Dirichlet conditions

are zero and can be neglected in the equations. Then, the weak formulation becomes:

$$\begin{aligned}
&\sum_{j=1}^{N_u} u_j \int_\Omega \Big(2\mu\frac{\partial\phi_{jx}}{\partial x}\Big)\frac{\partial\phi_{ix}}{\partial x} + \Big(\mu\frac{\partial\phi_{jx}}{\partial y} + \mu\frac{\partial\phi_{jy}}{\partial x}\Big)\frac{\partial\phi_{ix}}{\partial y} + \Big(\mu\frac{\partial\phi_{jx}}{\partial z} + \mu\frac{\partial\phi_{jz}}{\partial x}\Big)\frac{\partial\phi_{ix}}{\partial z} - p\frac{\partial\phi_{ix}}{\partial x} \\
&+\sum_{j=1}^{N_v} v_j \int_\Omega \Big(\mu\frac{\partial\phi_{jx}}{\partial y} + \mu\frac{\partial\phi_{jy}}{\partial x}\Big)\frac{\partial\phi_{iy}}{\partial x} + \Big(2\mu\frac{\partial\phi_{jy}}{\partial y}\Big)\frac{\partial\phi_{iy}}{\partial y} + \Big(\mu\frac{\partial\phi_{jz}}{\partial y} + \mu\frac{\partial\phi_{jy}}{\partial z}\Big)\frac{\partial\phi_{iy}}{\partial z} - p\frac{\partial\phi_{iy}}{\partial y} \\
&+\sum_{j=1}^{N_w} w_j \int_\Omega \Big(\mu\frac{\partial\phi_{jx}}{\partial z} + \mu\frac{\partial\phi_{jz}}{\partial x}\Big)\frac{\partial\phi_{iz}}{\partial x} + \Big(\mu\frac{\partial\phi_{jy}}{\partial z} + \mu\frac{\partial\phi_{jz}}{\partial y}\Big)\frac{\partial\phi_{iz}}{\partial y} + \Big(2\mu\frac{\partial\phi_{jz}}{\partial z}\Big)\frac{\partial\phi_{iz}}{\partial z} - p\frac{\partial\phi_{iz}}{\partial z} \\
&-\sum_{j=1}^{N_p} p_j \int_\Omega \Big(\frac{\partial\phi_{jx}}{\partial x} + \frac{\partial\phi_{jy}}{\partial y} + \frac{\partial\phi_{jz}}{\partial z}\Big)\psi_i d\Omega + \int_\Gamma \phi_i \boldsymbol{n}\cdot\boldsymbol{\sigma} d\Gamma = \int_\Omega \rho_i g \phi_{iz} d\Omega
\end{aligned} \tag{3.19}$$

The above formulation has the same number of unknowns and equations. By assembling the equations of all elements together according to every degree of freedom, the whole problem can be arranged into a matrix form and solved numerically:

$$\begin{bmatrix} \boldsymbol{K} & \boldsymbol{C} \\ \boldsymbol{C^T} & 0 \end{bmatrix} \begin{bmatrix} \boldsymbol{U} \\ P \end{bmatrix} = \begin{bmatrix} \boldsymbol{f} \\ 0 \end{bmatrix} \tag{3.20}$$

The direct solution of the above matrix equation is generally not the final converged solution as the viscosity in this system is non-linear. Picard's iteration is therefore used to find the true solutions. In each iteration, viscosity is updated using the velocity from the previous iteration. The iteration is finished until pre-defined convergence threshold are reached.

3.3 Model Validation

The simulations in this thesis are all conducted using the Ice Sheet System Model (ISSM) framework. ISSM is a coupled, thermo-mechanical, finite element, ice flow model (*Larour*

et al., 2012). The three models, FS, HO and SSA are all implemented in ISSM, which makes it practical to compare their performance (*Morlighem et al.*, 2010; *Seroussi et al.*, 2011).

The Marine Ice Sheet Model Intercomparison Project (MISMIP) experiment is an intercomparison project for marine ice-sheet models conducted in 2011 (*Pattyn et al.*, 2012). With a large number of participated models, its sets of experiments are used as benchmarks for marine ice sheet models that try to resolve grounding line dynamics. The MISMIP experiment is designed for 2D flowline models. In 2013, the MISMIP3D experiments is conducted as an extension to 3D marine ice sheet models (*Pattyn et al.*, 2013). The SSA and HO models of ISSM participated in these two projects and are shown to be reliable in capturing grounding line dynamics (*Pattyn et al.*, 2012, 2013). Here, we validate the FS model of ISSM using these two projects.

3.3.1 MISMIP Experiment

We first validate our 2D FS flowband model with the MISMIP experiments. The original MISMIP contains three sets of experiments. Here, we only conducted Exp.3 of MISMIP because it has a complicated bed geometry and its grounding line migration undergoes hysteresis.

In this experiment, the model is first run to steady state on an ideal bed that contains an overdeepening (Fig. 3.2b). Then, the ice rheology is changed by 13 steps. In each step, the model is run to steady state and the grounding line positions are compared between different models. Our results, shown in Fig . 3.2, indicate that the grounding line is unstable on a retrograde bed and displays a hysteresis behavior in response to perturbations in ice rheology, which is consistent with the MISI theory (*Weertman*, 1974). The steady state grounding line positions obtained by ISSM agree with the FS solution obtained by Elmer/Ice (*Durand et al.*, 2009a), to within 15 km. Our results are also in agreement with the analytical so-

lution of *Schoof* (2007), especially in the retreating phase (step 7-13), to within 20 km. In the advancing phase, the difference is larger, ∼50 km. However, this level of discrepancy in grounding line position is considered to be satisfactory and has been attributed to numerical issues associated with mesh resolution (*Durand et al.*, 2009a; *Pattyn et al.*, 2012). We therefore conclude that the FS model of ISSM is capable of reproducing the results of MISMIP Exp 3.

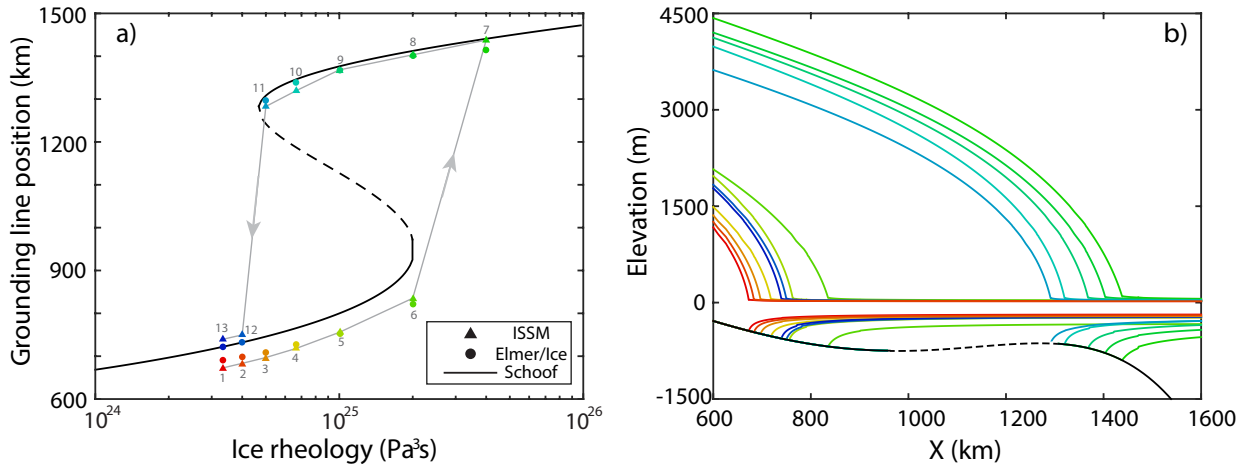

Figure 3.2: Results of MISMIP Exp 3. a) Steady state grounding line positions of MISMIP Exp 3. Triangles are results of ISSM; circles are results of the FS solution of Elmer/Ice *Durand et al.* (2009a) and the black curve is *Schoof* (2007) solution (*Pattyn et al.*, 2012). The gray arrow shows the sequence of ice rheology perturbation at each step. b) Steady state profile at each step obtained by ISSM. Each color represents each individual step as indicated in a). The retrograde part of the bed is shown in dashed line.

3.3.2 MISMIP3D Experiment

After the validation of our 2D model, we conduct the MISMIP3D experiments to validate our 3D FS model. The MISMIP3D experiments are constructed on a bed with constant slope with three phases. First, the model is run to steady state (experiment Stnd). Then, a perturbation (maximum at 75%) is introduced to the basal friction coefficient field to make the grounding line migrate (experiment P75S). Finally, the initial uniform basal friction

coefficient is restored to check if the grounding line migrates back to the initial steady state position (experiment P75S).

The results of our model and other models that participate in these experiments are summarized below in Fig. 3.3. In all three experiments, our model results (HYU in Fig. 3.3) are consistent with the majority of other models, especially with other FS models. In Exp. Stnd, we show a steady state grounding line position that is similar to most SSA models and FS models. In Exp. P75S, the grounding line of our model displays an advance in the y<25 km region and a slightly retreat in the y>25 km region. Finally, in Exp. P75R, our results display the reversibility of grounding line, which is consistent with the analysis done by *Schoof* (2007). Therefore, we conclude our FS model is capable of reproducing the MISMIP3D results and is reliable for applications on real glaciers.

3.4 Conclusion

In this chapter, we discussed the numerical implementation of a transient ice flow model. We first described the solving sequence of the ice flow problem using conservation laws. Then, we gave a brief explanation of the finite element method and how it is used to implement the ice flow model. Finally, we present our model results on the MISMIP experiments to show our model is validated.

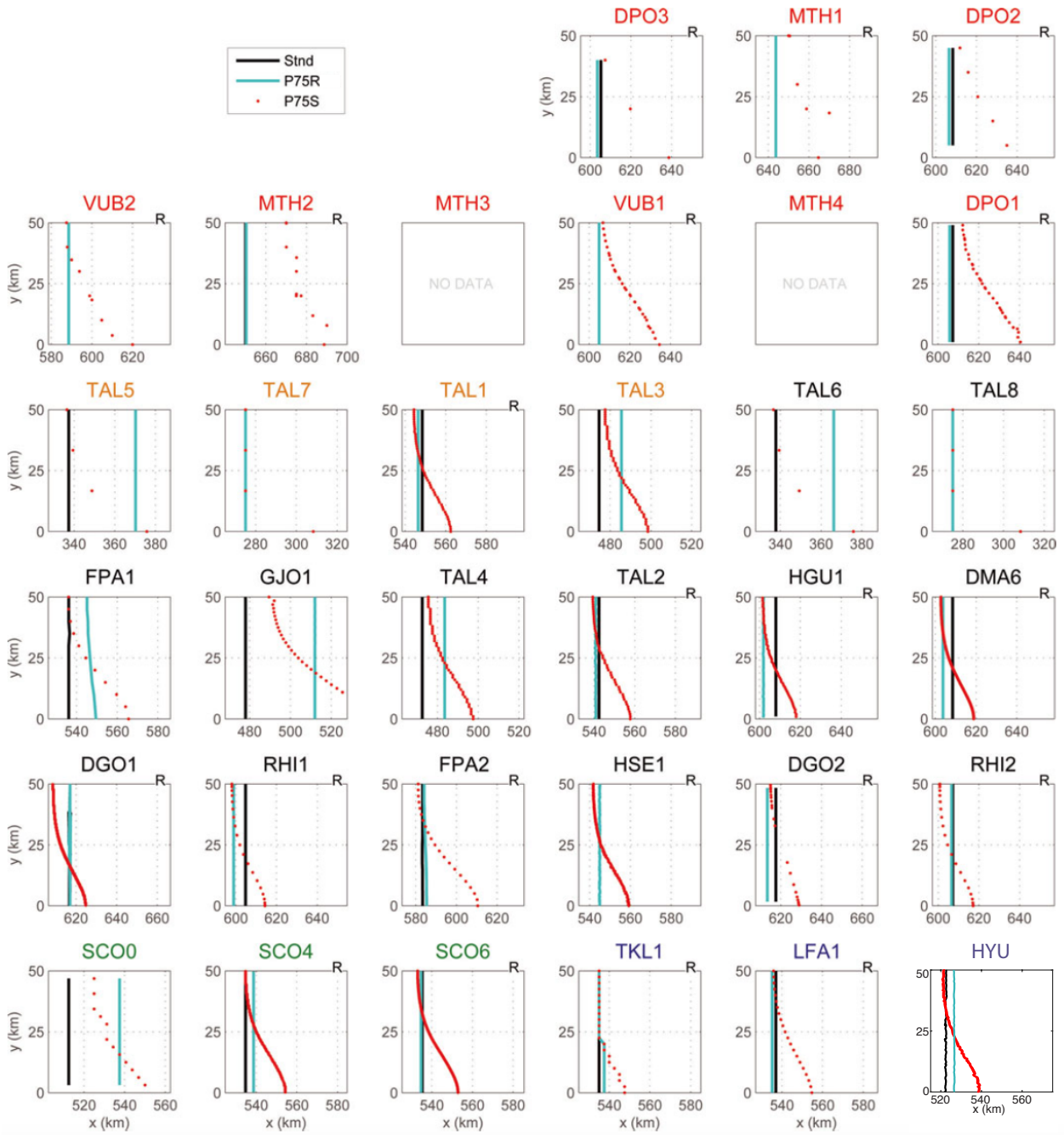

Figure 3.3: Results of MISMIP3D experiments from our FS model and all other participating models (our result, shown as HYU, is added to Fig. 5 of *Pattyn et al.* (2013)). Each panel represents one model. In each panel, black line is the steady state position for Exp. Stnd (covered by green line in some panels); red dotted line is for Exp. P75S and the green line is for Exp. P75R. The color of the name of each model represents model types. Black is for SSA model and dark blue is for FS model.

Chapter 4

Modeling Calving of Thwaites Glacier

In this chapter, we present a study on the calving dynamics of Thwaites Glacier (TG) combining a two-dimensional flowband full-Stokes (FS) model of its viscous flow with the linear elastic fracture mechanics (LEFM) theory to model crevasse propagation and ice fracturing. We first give an introduction about calving and the input data of our simulations. We then compare the FS results and those obtained with simplified models with crevasses observed from radar depth sounders. We discuss the importance of using the FS model to model crevasse propagation and the conditions that favor the growth of crevasses.

4.1 Calving

Calving is the separation of ice blocks from glacier margins. The calved ice blocks become icebergs in the ocean. Calving is an important process that accounts for a significant portion of the mass loss from ice sheets. In AIS, the mass loss from calving is estimated to be 755–1321 Gt/yr (*Depoorter et al.*, 2013; *Liu et al.*, 2015). This corresponds to a third to a half of the total mass loss of AIS. Although the loss of ice shelves via calving has almost

negligible direct impact on global mean sea level rise, its indirect impact is crucial. By directly removing part of the ice shelves, calving reduces the buttressing of ice shelves to grounded ice sheets. In this way, calving results in speeding up of glaciers, which leads to further dynamical mass loss and grounding line retreat (*MacGregor et al.*, 2012).

Large calving events have been observed on the floating ice shelf of TG (Fig. 4.1b) by satellites (*MacGregor et al.*, 2012). Densely distributed surface and bottom crevasses have been revealed by radar depth sounders (Fig. 4.2). The calving rate of TG is currently at ∼60 Gt/yr (*Depoorter et al.*, 2013; *Rignot et al.*, 2013). As the glacier retreats further inland and loses its floating section, its rate of iceberg calving is likely to increase, which would enhance the glacier's contribution to global sea level rise (*Deconto and Pollard*, 2016). It is therefore essential to better understand and simulate the calving dynamics of TG. The calv-

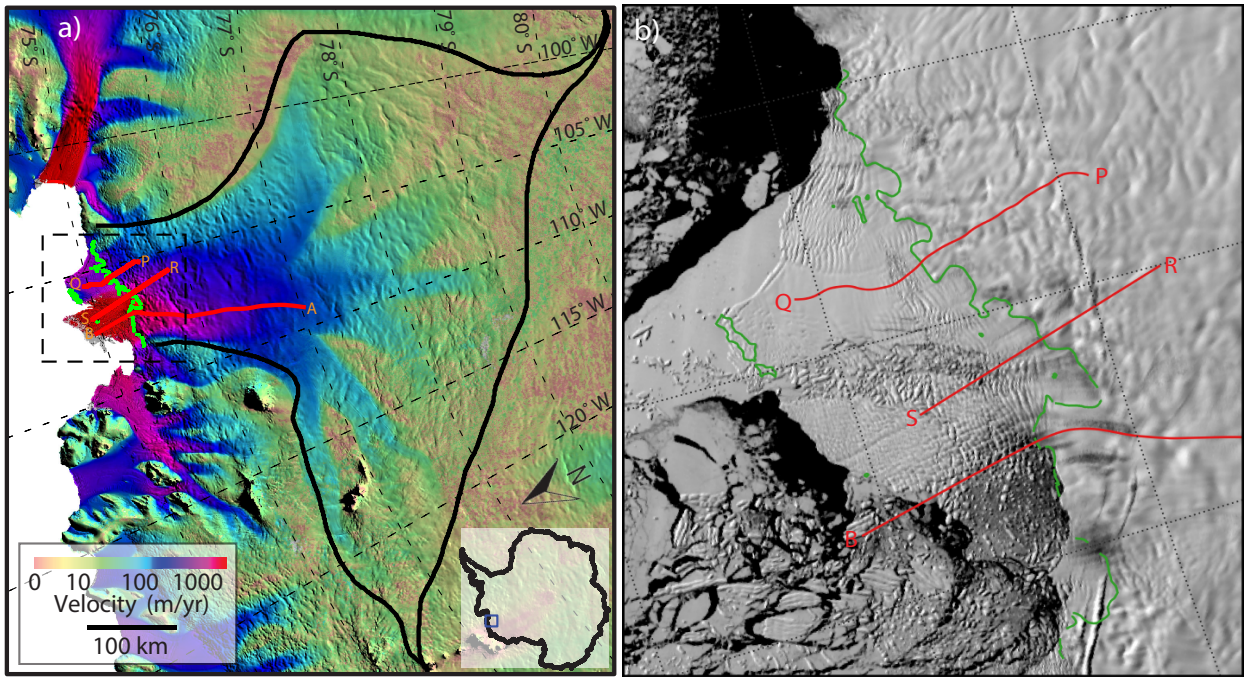

Figure 4.1: Velocity map and MODIS image of TG. a) Velocity field of TG in 2008 (*Rignot et al.*, 2011a). The black contour is the drainage basin of TG. b) MODIS image of the dashed box region in a) on Nov. 01, 2012. PQ and RS are the flight tracks of the echograms shown in Fig. 4.2. AB is the selected flowline of this study. The green line is the grounding line of TG in 2011 (*Rignot et al.*, 2011b).

ing of icebergs is difficult to model because of the processes involved, such as the initiation, propagation and orientation of crevasses, are not well understood and direct observations are rare (*Benn et al.*, 2007). A universal calving law is therefore missing. Most prior studies of crevasse propagation follow the work of *Nye* (1957b), where crevasses propagate based on the balance between longitudinal stress and the overburden pressure of ice (*Bassis and Walker*, 2012; *Nick et al.*, 2013; *Cook et al.*, 2014). Although this criterion helps reproduce ice front calving, it does not take into account the stress concentration at the rupture tip of the crevasses. This criterion corresponds to the case of multiple closely spaced crevasses (*Weertman*, 1973; *Bassis and Walker*, 2012; *Ma et al.*, 2017), but it underestimates the penetration depth of isolated crevasses (*van der Veen*, 1998a; *Plate et al.*, 2012). To simulate crevasse propagation at the rupture tip, it is necessary to use a fracture theory, such as the linear elastic fracture mechanics (LEFM). This theory has been successfully applied in prior studies to the case of crevasse propagation. *van der Veen* (1998a,b) used LEFM to model penetration depth of surface and bottom crevasses. *Larour et al.* (2004a,b) employed LEFM along the rupture tips of ice shelves and showed that the modeled deformation around rupture tips matched observations of ice deformation from fine-scale radar interferometry. *Krug et al.* (2014) combined LEFM with damage mechanics and reproduced the observed calving front position of Helheim Glacier in Greenland. In their study, however, the crevasse propagation process is not modeled. The crevasses were either zero in size or propagating through the entire ice thickness to create a calving event.

In order to obtain a description of stresses that control crevasse propagation in a time dependent fashion, our approach is to model the viscous flow of ice using an ice flow model and employ the LEFM theory for crevasse propagation. We apply this approach to study the calving dynamics of TG using the Ice Sheet System Model (ISSM) (*Larour et al.*, 2012). The model simulations are conducted in two dimensions (2D) along a flowline, with geometry based on remote sensing observations. We combine various ice flow models with the LEFM theory to investigate crevasse propagation and iceberg calving. We compare the calving

behavior of TG using different initial geometries and different levels of complexity of the numerical ice flow models used to calculate the stress field. We conclude on the importance of using FS for modeling the calving processes of TG and the conditions that are conducive to calving.

4.2 Data and Methods

4.2.1 Data

To model TG in 2D, we select a flowline at the center of its fast flowing region as shown in Fig. 4.1. The flowline is 238 km long, with a 38 km long floating ice tongue (Fig. 4.3). BEDMAP-2 is used for ice surface, ice bottom and bed elevation (*Fretwell et al.*, 2013). Over grounded ice, the bed elevation is replaced by the bed elevation computed from a mass conservation method (*Morlighem et al.*, 2011, 2013). At the grounding line, the two datasets display discrepancies in the order of 100 m in a few places, but not along the particular flowline that we selected. The ice temperature field is the steady state temperature computed from the thermal model in ISSM (*Larour et al.*, 2012; *Seroussi et al.*, 2013). The thermal model is constrained by surface temperature from the regional atmospheric climate model RACMO2 (*Lenaerts et al.*, 2012) and geothermal heat flux from *Maule et al.* (2005) and includes both conduction and advection processes (*Morlighem et al.*, 2010; *Seroussi et al.*, 2013). The ice surface velocity derived from interferometric synthetic aperture radar (InSAR) data collected in 2008 is used to constrain the ice flow model (*Rignot et al.*, 2011a).

The NASA Airborne Topographic Mapper (ATM) (*Krabill*, 2014) surface elevation data and the CReSIS MCoRDS ice thickness data (*Gogineni*, 2012) provide ice surface and ice shelf bottom elevation, respectively, along flight tracks. We use these observations to evaluate our modeling results. Firn correction is applied to each flight track to ensure that the

hydrostatic ice bottom calculated from surface elevation matches the observed ice bottom along the ice shelf. Fig. 4.2 shows the echograms of two flight tracks along the ice shelf of TG, superimposed by the bed picks from CReSIS, surface from ATM and the hydrostatic ice bottom calculated from these datasets.

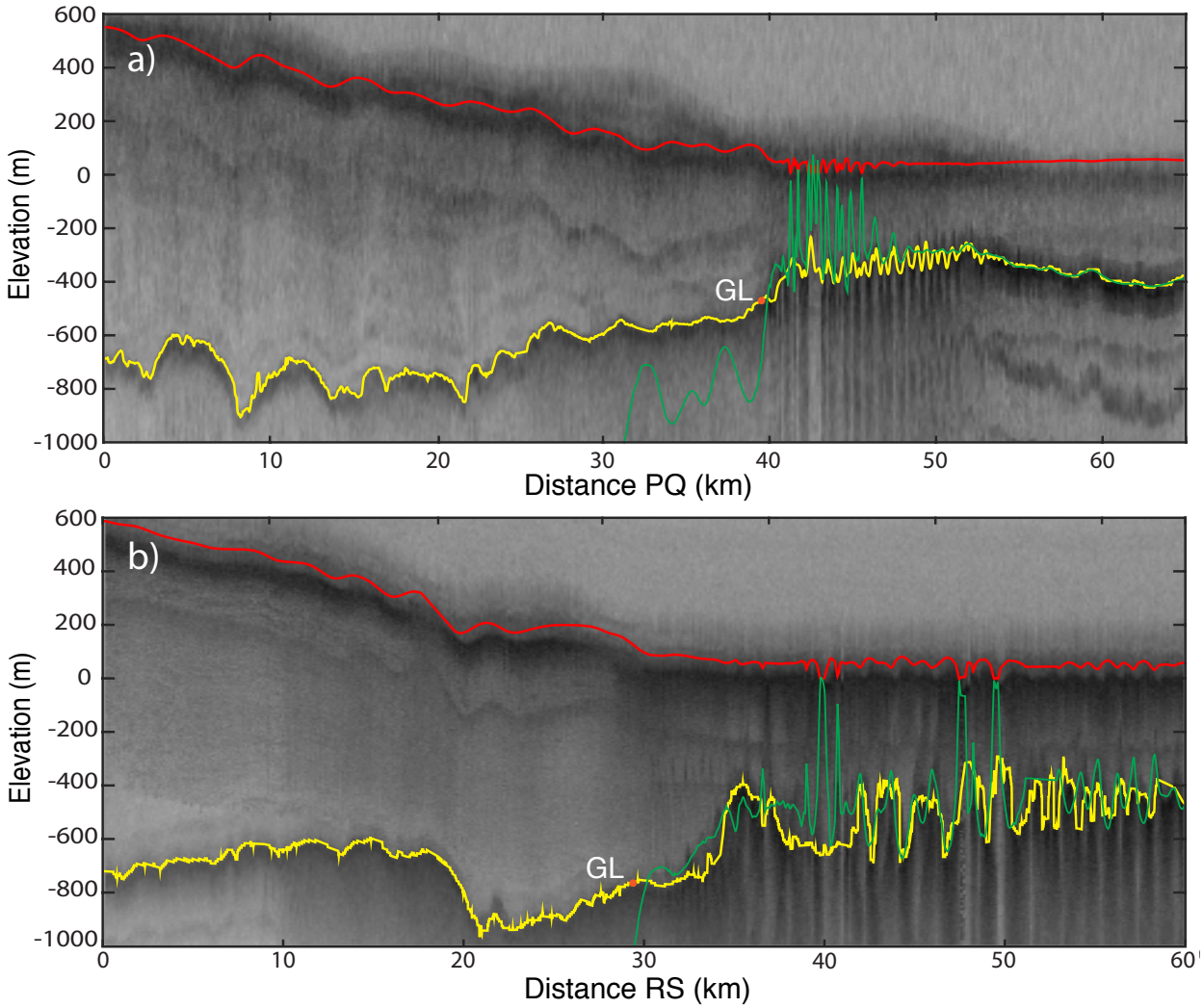

Figure 4.2: Two echograms of Thwaites Glacier (TG). a) Echogram of flight track PQ on Nov.02, 2009. b) Echogram of flight track RS on Nov.19, 2010. The red lines are ice surface elevation measured by Airborne Topographic Mapper (ATM) (*Krabill*, 2014) and the green lines are bed elevation calculated from hydrostatic equilibrium. The yellow lines are the elevation of ice bottom measured by ice radar depth sounder (*Gogineni*, 2012). The orange dots are the grounding line positions in 2011 (*Rignot et al.*, 2011b).

4.2.2 Ice Flow Model

We use the solution sequence described in Chapter 3 to compute the viscous flow of ice (Fig. 3.1). The geometry and boundary conditions of our model are shown in Fig. 4.3. For every experiment, we run with FS, HO and SSA and compare their results.

Since this study is conducted in 2D, several adjustments to the 3D equations are needed. First, in the governing equations (Eq. 2.24, 2.28, 2.31), the y direction is neglected. Second, since the y direction is neglected, the lateral drag has to be parameterized so that buttressing from the ice shelf can be included in the model. Here, the lateral drag is represented by adding a body force on the ice shelf in the governing equation, as in *Gagliardini et al.* (2010):

$$f = -\frac{2(n+1)^{\frac{1}{n}}B}{W^{\frac{n+1}{n}}}u^{\frac{1}{n}}; \tag{4.1}$$

where W is the width of glacier, taken here as 130 km. Third, the convergence of ice from upstream to downstream also needs to be taken into account to conserve mass. Here, we first calculate the ice mass flux along the flowline. Then, we add an artificial surface mass balance term, $\dot{m}_a$, to the original surface mass balance, $\dot{m}_s$, to ensure that the ice mass flux is constant from the inflow boundary to the grounding line.

At the bed, we choose to use a linear friction law (q =0 and p=1 in Eq. 2.20):

$$\boldsymbol{\tau_b} = -\alpha^2 \boldsymbol{v}_b \tag{4.2}$$

where $\boldsymbol{\tau_b}$ is the basal drag, $\boldsymbol{v}_b$ the velocity tangential to the bed, and α the friction coefficient. Here, α is inferred from an inversion so that the modeled surface velocity matches the observed surface velocity (Section 2.4). In this study, the simulation time is short, the grounding line does not migrate, and the changes in ice thickness are small. The impact of

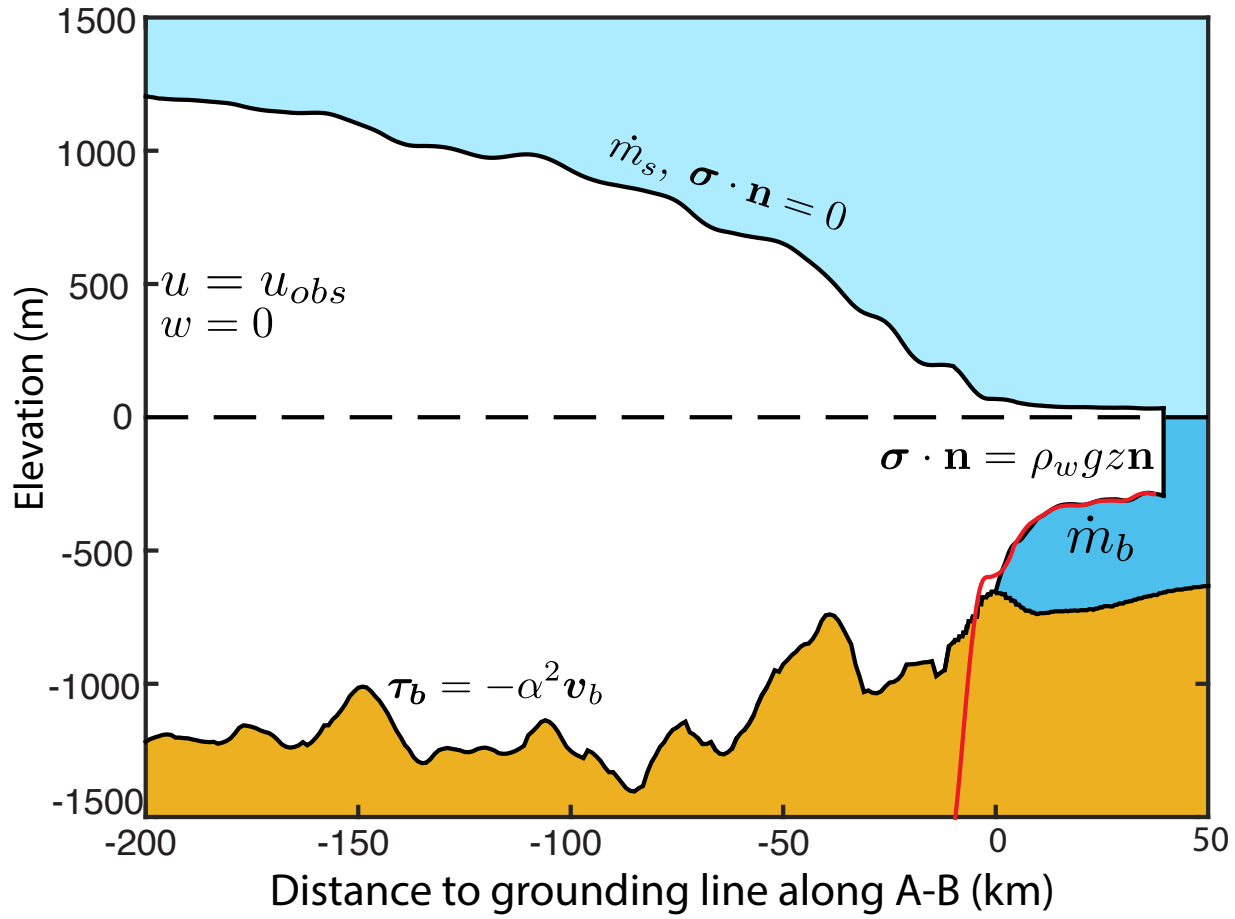

Figure 4.3: Geometry of the selected flowline AB and boundary conditions of the model. The black lines are ice surface elevation, ice bottom elevation and bed elevation. The red line is the hydrostatic bottom elevation calculated from surface elevation.

the sliding law is therefore limited and we choose to use this linear sliding law for simplicity.

4.2.3 Linear Elastic Fracture Mechanics Model

A physically-based LEFM model is used to simulate crevasse propagation. In the LEFM theory, there are three modes to open a crevasse: mode I opening, mode II sliding and mode III tearing (*Anderson*, 2005). Only mode I is considered here. The key variables in LEFM are the stress intensity factor, $K(x, z, t)$, and the fracture toughness, K_c. If K is larger than

K_c, a crevasse will propagate. For a crevasse at a given location with a given stress field, K is computed through the integration of the normal stress from the bottom of the crevasse to the tip of the crevasse (*van der Veen*, 1998a). For bottom crevasses, the equations are:

$$K = \int_b^{b+h} \frac{2\sigma_n(z)}{\sqrt{\pi h}} G(z, h, H) dz \tag{4.3}$$

$$\sigma_n(z) = \sigma'_{xx}(z) + \rho_w g z - \rho_i g (s - z) \tag{4.4}$$

where h is the height between the tip and the bottom of the crevasse, b the elevation of the ice shelf bottom, H the ice thickness, $\sigma'_{xx} = \sigma_{xx} + p$ the deviatoric stress, with σ_{xx} the longitudinal stress and p the pressure and G a weighting function (*Krug et al.*, 2014). For surface crevasses, the equations are similar with the water pressure term equal to zero since we assume no melt water production at the surface. K_c is a material property and previous studies showed that K_c ranges from 0.1 to 0.4 MPa $m^{1/2}$ for ice (*Fischer et al.*, 1995; *Rist et al.*, 1996, 2002). Here, K_c is set to 0.2 MPa $m^{1/2}$ following *Krug et al.* (2014).

A simple algorithm for the combination of ISSM and LEFM is described in Fig. 4.4. First, a position is chosen arbitrarily as the initial crevasse position. ISSM is used to calculate the stress field. With this stress field at the location of the initial crevasse, the LEFM theory is used to find the maximum heights of the surface and bottom crevasses that satisfy $K > K_c$. However, this criterion is never satisfied when the crevasse depth is small (cm scale) and a minimum depth is required. Here, we assume that a crevasse can propagate if its minimum required depth is smaller than 1 m. This process is assumed to be instant and the stress field is assumed to be unchanged (*Duddu et al.*, 2013; *Ma et al.*, 2017). Once the crevasse is opened, its width is assumed to grow to 20 m instantaneously (our mesh resolution is 5 m). The geometry is then updated to include the new crevasses. Numerically, this is done by migrating each node vertically, but none of the nodes are removed from the mesh. The new ice geometry is allowed to adjust viscously with ISSM for a period of 0.01 yr during which the crevasse becomes wider, shallower, and smoother due to the viscous deformation

of ice. The computed pressure also becomes close to the hydrostatic pressure during this period as the singularity in the pressure field near the crevasse tip is diminished. When the shape of a crevasse is adjusted viscously, its width violates LEFM assumptions. The pre-existing crevasse is therefore considered as a feature on the ice shelf and affects the stress field computed from the viscous model. When LEFM is called again, it is applied to an infinitesimal crevasse at the apex of the pre-existing crevasse. The new crevasse, if it propagates, grows to 20 m wide instantly and then merges into the pre-existing crevasse through viscous deformation. Calving is assumed to occur when the surface crevasse reaches sea level or when the bottom crevasse reaches the ice surface (*Benn et al.*, 2007).

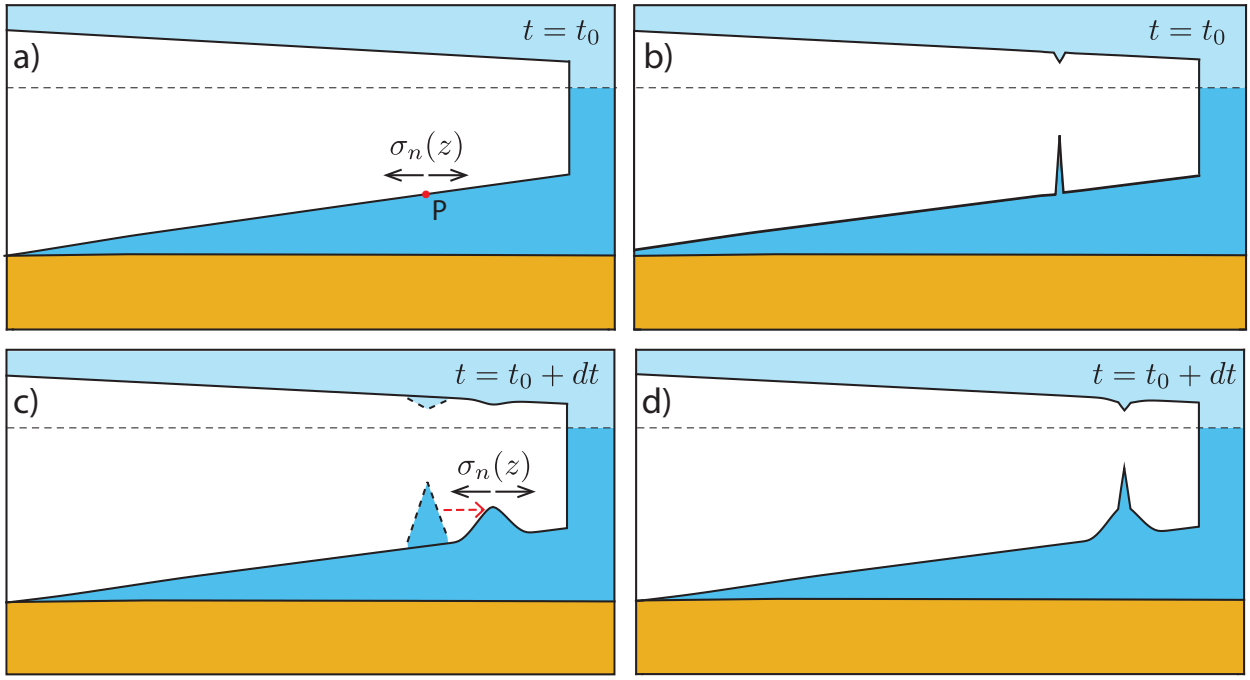

Figure 4.4: Schematic of the combination of ISSM and LEFM. a) Initial condition, b) Crevasses propagate, c) Crevasses advect downstream, d) Crevasses grow.

4.3 Model Setup

In our simulations, the horizontal resolution of the mesh is 100 m, refined to 5 m within 3 km of the initial crevasse position. Vertically, the domain is uniformly discretized into 40 layers. In total, the domain has 281,680 elements. The time step we chose is 0.0005 yr (∼4.4 hr) and the LEFM model is called every 0.01 yr. The simulations are run for 0.3 yr or until calving occurs, whichever happens first. In all the following experiments, the ice shelf melt rate is chosen so that the grounding line does not migrate and the ice shelf bottom has a stable elevation (within few meters).

Five sets of experiments, labeled Exp. A–E, are conducted to simulate the propagation of crevasses (Table. 4.1). In the first set, eleven experiments, Exp. A1–A11, are run with infinitesimal initial crevasses, zero crevasse depth and width, at both the surface and the bottom. In these experiments, the numbers 1–7 indicate crevasses initiated near the grounding line (at distances x = 0.5, 1, 1.5, 2, 2.5, 3, 3.5 km downstream of the grounding line); the numbers 8 and 9 indicate crevasses initiated in the middle of the ice shelf (x= 18, 28 km); and the numbers 10 and 11 indicate crevasses near the ice front (x = 35, 36 km). The initial crevasse positions are chosen to be more densely spaced in the grounding line region as the stress conditions in this region are more complicated and exhibit more spatial variations.

In the next four sets of experiments, the initial glacier geometry is altered to evaluate its impact on crevasse propagation. The second (Exp. B1–B7) and the third (Exp. C1–C3) sets are designed to test the stability of TG with a shortened ice shelf. The length of the ice shelf is reduced from 38 to 4 km (Exp. B) and 2 km (Exp. C), respectively. In the fourth set of experiments (Exp. D1–D7), a 3 m deep, 100 m wide initial surface crevasse is added to the initial geometry while the initial bottom crevasse is still kept as an infinitesimal crevasse. In the last set (Exp. E1–E7), we undercut the ice shelf front of a 4 km–long ice shelf by 400 m

Experiment Set	Number of Experiments	Experiment Characteristics
A	11	Current geometry with infinitesimal initial crevasses
B	7	4 km ice shelf
C	4	2 km ice shelf
D	7	3 m initial surface crevasse
E	7	4 km ice shelf with 400 m high, 400 m wide undercutting

Table 4.1: Summary of the initial set up of experiments.

over the last 400 m. The initial crevasse positions for experiments B-E are the same as Exp. A.

4.4 Results

4.4.1 Inversion

The inversion results of FS, HO and SSA are shown in Fig. 4.5. For all three models, the inferred basal friction coefficient, α, has similar values and spatial patterns. The modeled ice surface velocities are in reasonable agreement. The modeled surface velocity after inversion closely matches the observed surface velocity over grounded ice. However, there remains a 200 m/yr, or 6%, difference in the grounding line region and on the ice shelf. We attribute this discrepancy to errors in ice rheology and uncertainties associated with the parameterization of the lateral drag.

4.4.2 Observed Crevasses

In the data acquired by NASA ATM and CReSIS MCoRDS from 2009 to 2014 (*Gogineni*, 2012; *Krabill*, 2014), we find that surface and bottom crevasses are densely distributed on the ice shelf of TG (Fig. 4.1b and Fig. 4.2). With these data, we estimate the height and width

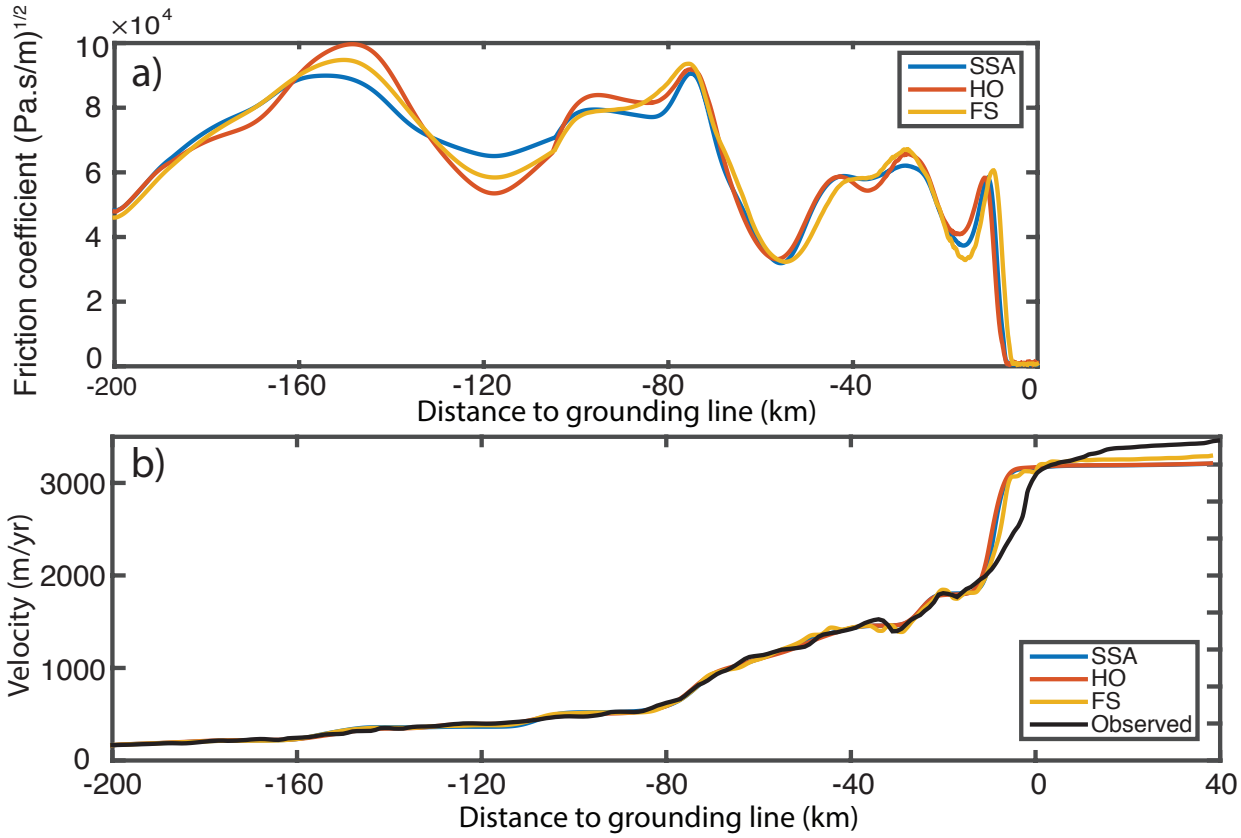

Figure 4.5: Inversion results of basal friction on flowline AB. a) Friction coefficient inferred with all three models (FS, HO and SSA). b) Comparison of modeled surface velocity and observed surface velocity for all three models.

of each surface and bottom crevasse (crevasses narrower than 200 m are neglected because of the high uncertainties in their depth and width). The results are shown in Fig. 4.6. We find that the mean height is 18.7 m for surface crevasses and 103.1 m for bottom crevasses. The height of surface crevasse ranges from 2–82 m, but 90% of them are within 2–40 m. The height of bottom crevasses ranges from 20–270 m. The mean width for surface and bottom crevasses are 821 m and 724 m, respectively, and 80% of the crevasses have a width ranging from 300 m to 1000 m. The nominal measurement error is 10 cm for the ATM-derived ice surface elevation. However, at some data points, especially on the ice shelf, the error can reach a few meters (*Krabill*, 2014). The measurement error for the MCoRDS-derived ice bottom elevation is 14 m (*Gogineni*, 2012).

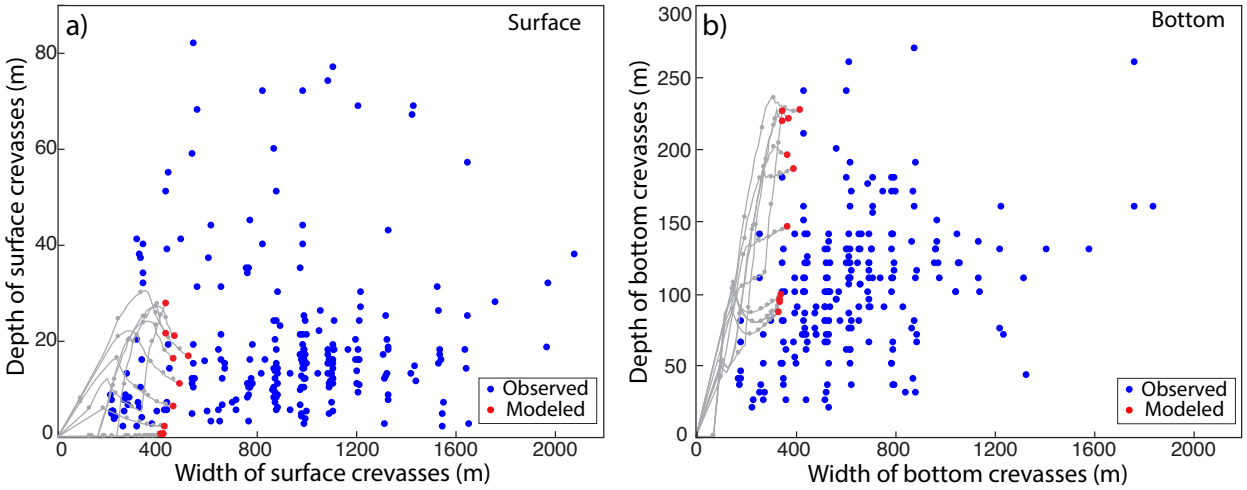

Figure 4.6: Comparison of the shape of observed and modeled crevasses. a) Depth and width of surface crevasses. b) Depth and width of bottom crevasse. Blue dots are observed crevasses and red dots are modeled crevasses from Exp. A. Gray lines and gray dots are the evolution of the shape of modeled crevasses.

4.4.3 Deviation from Hydrostatic Equilibrium

In the grounding line region, i.e. within 5–10 km downstream of the grounding line, ice is pushed down below hydrostatic equilibrium because of a bending moment applied on the ice that arises as the basal regime changes abruptly across the grounding line. In TG, the ice is tens of meters below hydrostatic equilibrium (*Fretwell et al.*, 2013). In our selected flowline, the maximum deviation is 85 m. In the two flight tracks shown in Fig. 4.2, we find a maximum deviation of 130 m for track PQ and 122 m for track RS. In addition, in the region where surface and bottom crevasses are present, the deviation is larger and measured in hundreds of meters (Fig. 4.2). In the FS solution, it is possible to account for this non-hydrostatic condition. For instance, we obtain a maximum deviation of 68 m in a steady state solution for our selected flowline.

4.4.4 Crevasse Propagation

The evolution of K for selected experiments with different models is shown in Fig. 4.7. For HO and SSA, the crevasses do not propagate if the initial crevasse position is >2000 m downstream of the grounding line. When the crevasse propagates, the stress intensity factor decreases. The crevasse then stops growing when $K < K_c$ and closes up due to the viscous deformation. At the end of the simulations, the bottom crevasse never exceeds 50 m, which is small compared to observations (Fig. 4.6). In other words, the combination of LEFM with HO and SSA cannot produce deep crevasses and calving events due to their inherent assumption of hydrostatic equilibrium. In the remainder of the study, we therefore only discuss the FS case.

In the first set of experiments (Exp. A1–A11), with the initial geometry and infinitesimal crevasses on the top and the bottom of the ice shelf, the crevasses of all eleven cases stop growing at the end of the simulations and none produce a calving event (Fig. 4.8). The final height of bottom crevasses is 200–300 m near the grounding line (Exp. A1–A7) and 50–100 m downstream (Exp. A8–A11). The surface crevasses are one order of magnitude smaller, 10–15 m near the grounding line and 2–5 m downstream. The width of all crevasses is between 400 and 500 m. The results of the experiments with varying initial geometries are shown in Fig. 4.9. With an ice shelf shortened to 4 km, calving occurs within 1 km of the ice front (Exp. B6 and B7, Fig. 4.9a) and the other experiments (Exp. B1–B5) have results similar to the initial 38 km long ice shelf (Exp. A1–A5), i.e. the final bottom crevasse height does not exceed 200–300 m. With an ice shelf shortened to 2 km, calving occurs in all three experiments (Exp. C1–C3, Fig. 4.9b). In Exp. D1–D7, where we add a 3 m deep, 100 m wide, initial surface crevasse, calving occurs for crevasses located within 1.5 km of the grounding line (Exp. D1–D3, Fig. 4.9c). Further downstream (Exp. D4–D7), the crevasse propagation is identical to the case with infinitesimal surface crevasses (Exp. A4–A7).

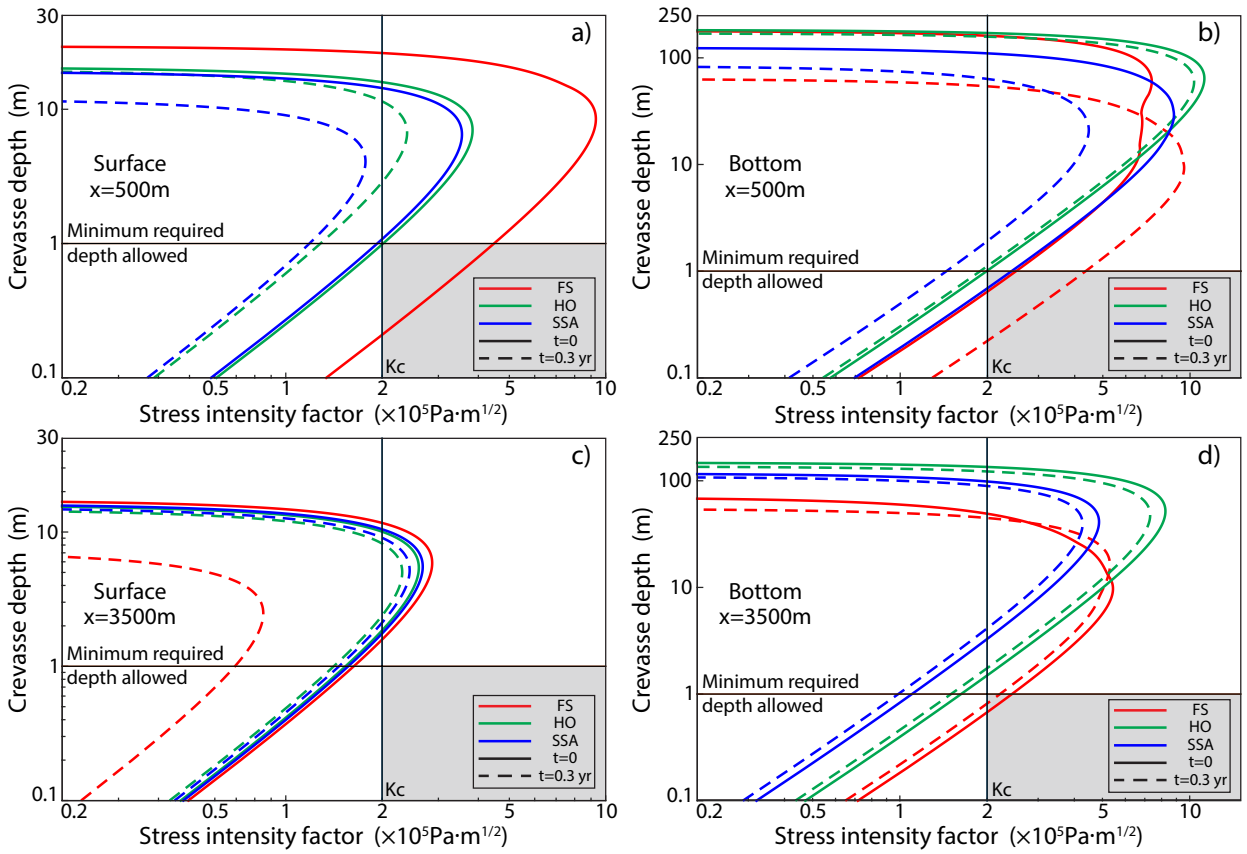

Figure 4.7: Stress intensity factor as a function of depth. a) Surface crevasse with initial crevasse position at x=500 m. b) Bottom crevasse with initial crevasse position at x=500 m. c) Surface crevasse with initial crevasse position at x=3500 m. d) Bottom crevasse with initial crevasse position at x=3500 m. Red, green and blue lines are corresponding to the FS, HO and SSA model. Solid and dashed lines are corresponding to the beginning and the end of each simulation. (The stress intensity factor for surface crevasse of FS at x=500 m, t=0.3 yr is not shown because it is negative at all depth.) The crevasse propagates if its minimum required depth is smaller than 1 m, (i.e., if the curve passes through the fourth quadrant).

In the last set, where the ice shelf is shortened and undercut, we find that calving occurs within 1.5 km of the ice front (Exp. E5–E7, Fig. 4.9d). In regions where calving does not occur, undercutting vanishes slowly within 0.1 yr due to the viscous deformation and downstream advection of ice.

Among all experiments, only Exp. B6 produces calving caused by a surface crevasse propagating to sea level and it takes 0.24 yr for the calving to occur. For all other calving cases, calving occurs because a bottom crevasse propagates to sea level and the process is five times

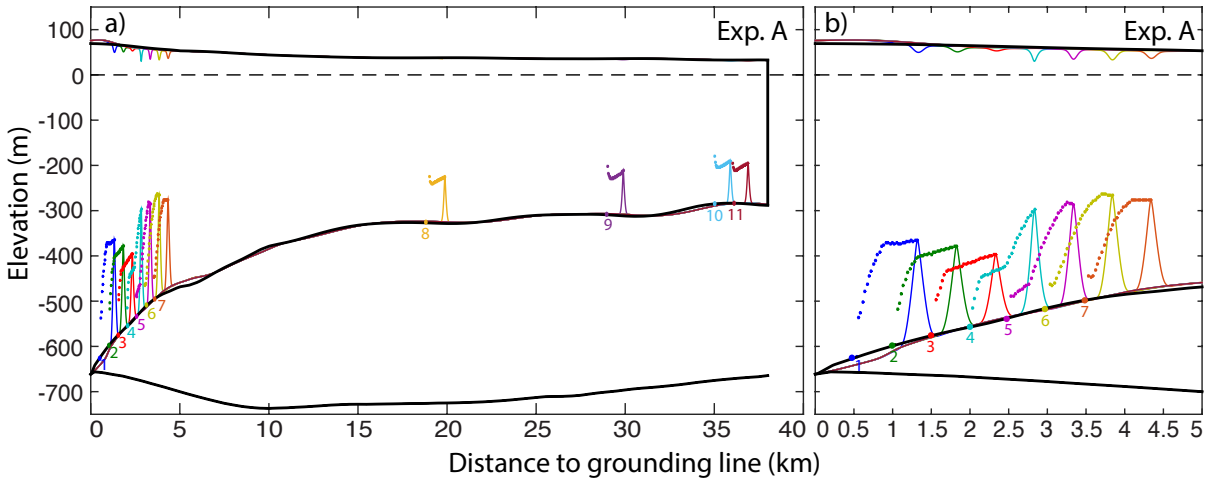

Figure 4.8: Crevasse propagation with the initial geometry of flowline AB. a) Crevasse propagation of Exp. A1–A11 with FS. Each color corresponds to one initial crevasse position, indicated by the number. The solid lines are the shape of final crevasses. The dotted lines are the evolution of the tips of bottom crevasses. b) Details of the grounding line region for Exp. A1-A7. The black lines are the initial geometry for ice surface, ice bottom and seafloor.

more rapid, i.e. within 0.05 yr. For the cases that calving does not take place, the crevasses stop growing before the end of the simulations. In Exp. A5–A11, the modeled crevasses undergo a non-monotonic evolution where the depth of the crevasses decrease in a few time steps during the simulation (Fig. 4.8). This evolution is caused by the temporal change in K. K decreases when the crevasse propagates until it stops growing. K then increases when the crevasse become shallower viscously until it can propagate again.

4.5 Discussion

The width and depth of surface and bottom crevasses produced by our crevasse propagation experiments with FS are within the range of the width and depth of surface and bottom crevasses observed by ice radar sounders (Fig. 4.6). This suggests that the combination of FS with the LEFM theory is a realistic way to model crevasse propagation and iceberg calving.

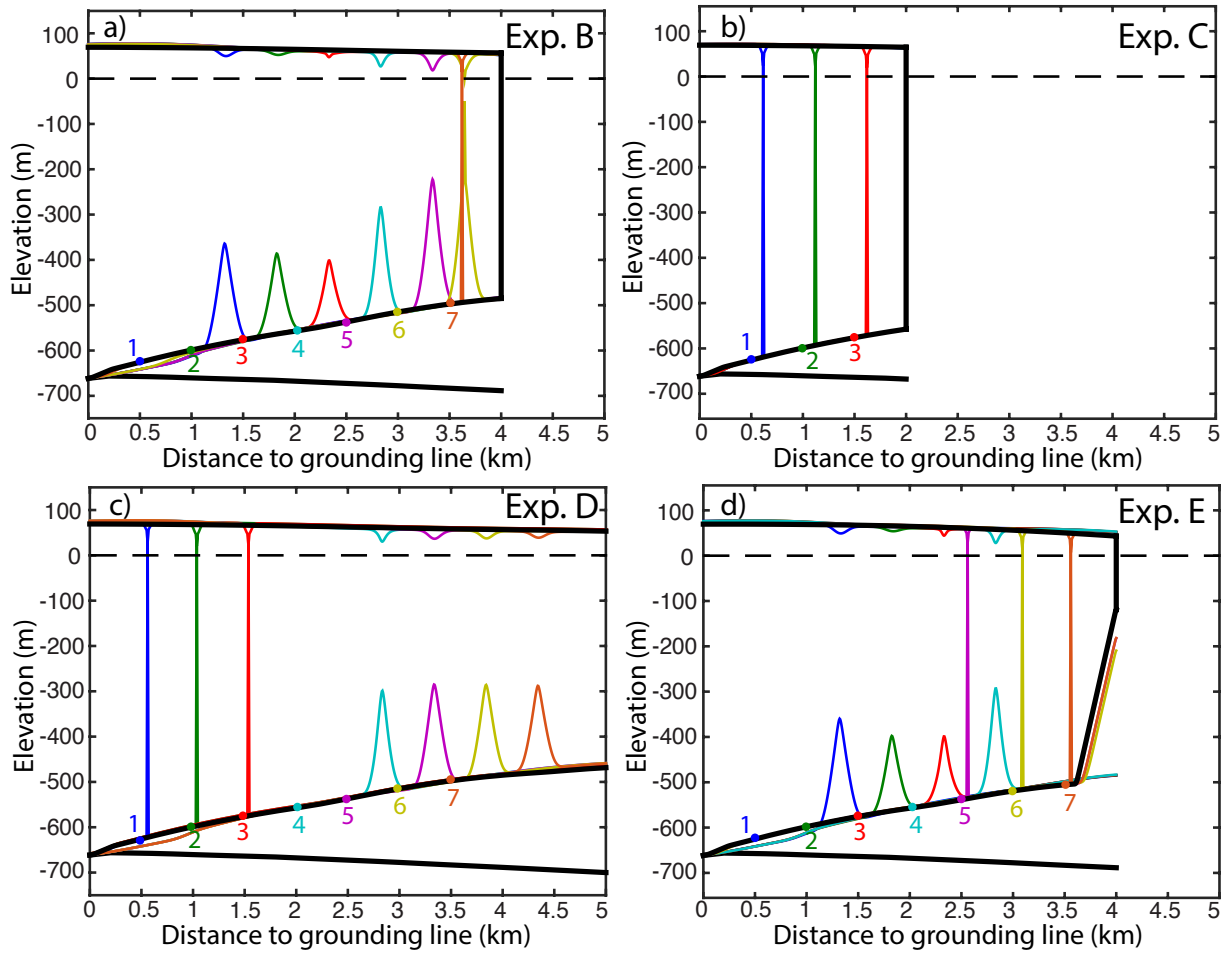

Figure 4.9: Crevasse propagation in the grounding line region with varying initial geometry. In each panel, solid lines are the shape of final crevasses with a) 4 km long ice shelf (Exp. B1–B7), b) 2 km long ice shelf (Exp. C1–C3), c) 3 m deep, 100 m wide initial surface crevasse (Exp. D1–D7), and d) 4 km long ice shelf with a 400 m wide and 400 m high undercut ice front (Exp. E1–E7). The black lines are the initial geometry for ice surface, ice bottom and seafloor.

Some observed crevasses are wider than our modeled crevasses because the width of the crevasse is still increasing at the end of our simulations (the depth is stable). Furthermore, we do not include ocean forcing in our model, which could affect crevasse growth. There are also some observed surface crevasses that are much deeper than our modeled crevasse. However, a number of these surface crevasses correspond to rift, i.e. ice surface is close to sea level, hence nearly equivalent to calving events. With HO and SSA, however, because of the assumption of hydrostatic equilibrium, the water pressure term and the overburden ice

pressure term in Eq. (20) cancel each other at the bottom of the ice shelf and thus the bottom crevasses are unable to grow to a size that matches observations. With the non-hydrostatic condition included, the two pressure terms in Eq. (20) do not cancel each other with FS in the region near the grounding line or the region with crevasses, which helps propagate the crevasses. In the radar echograms, large bottom crevasses (over 100 m) are also observed along the ice shelf, tens of kilometers downstream of the grounding line. According to our results from Exp. A, the crevasses formed in the grounding line region stop growing once they reach a stable size. Therefore, we posit that these crevasses are the result of advection of crevasses formed upstream. In summary, the non-hydrostatic condition plays a major role in crevasse formation. Not accounting for this condition makes it difficult to explain the observed crevasse pattern.

In our simulations, we find that crevasses propagate significantly faster near the ice front when the ice shelf is shortened. In principle, the length of a nearly non-confined ice shelf, such as the floating ice tongue of TG, should not have a major impact on the buttressing that the ice shelf exerts on grounded ice. Here, we find that the propagation of crevasses near the ice front, while limited for the initial 38 km-long ice shelf, becomes significantly enhanced with a shortened ice shelf. When the ice shelf is shortened, the longitudinal stress near the ice front increases at the surface and decreases at the bottom. The increase in the surface stress makes it easier for the surface crevasse to propagate, while the decrease in bottom stress prevents the propagation of the bottom crevasse. Over time, the stress at the bottom increases and the surface crevasse grows. The bottom crevasse is then able to propagate quickly through the entire ice column to cause calving because of the large difference between the water pressure and the overburden ice pressure. If calving takes place and creates a shorter ice shelf, our model predicts that the new ice shelf will be more prone to calving, i.e. a positive feedback.

When an initial crevasse of 3 m depth and 100 m width is added to the surface, we find that the surface crevasse grows quickly to 35 m before the bottom crevasse starts to propagate. The large difference between the water pressure and the overburden ice pressure at the bottom however, makes the bottom crevasse propagate rapidly through the entire ice thickness and produces calving. This is consistent with *Bassis and Walker* (2012), who suggested that ice shelves are difficult to form in the presence of pre-existing crevasses. However, long ice shelves calving at the grounding line region is not something commonly observed on TG. Three reasons might explain this result. One reason is that we assume that a surface crevasse aligns perfectly with an infinitesimal crevasse at the bottom, which is not certain. A second one is that bottom crevasses could also form from thermal cracking (*Humbert and Steinhage*, 2011; *Vaughan et al.*, 2012), in particular not aligned with a surface crevasse. Thermal cracking would facilitate the propagation of a bottom crevasse. If the corresponding surface crevasse remains shallow, the seawater-filled bottom crevasse formed by thermal cracking will not propagate far because the difference between the water pressure and the overburden ice pressure will be smaller than in the presence of a deep surface crevasse. The third reason is that most surface crevasses are formed in train, whereas here we only model one. A train of crevasses creates a shielding effect, which effectively reduces the stress concentration at rupture tips and anneals the propagation of crevasses (*van der Veen*, 1998a; *Krug et al.*, 2014).

Undercutting on the ice front is a common feature, especially for tidewater glaciers with a short to non-existent floating section (*Rignot et al.*, 2010). In a prior study, *O'Leary and Christoffersen* (2013) suggested that undercutting leads to significant changes in the stress field that enhances calving. *Cook et al.* (2014) argued, however, that the changes in stress field are only significant in diagnostic simulations and is much smaller in prognostic simulations. *Krug et al.* (2015) also showed that undercutting has no effect on the glacier mass balance on annual time scales. Here, we find that undercutting does affect the stress field significantly near the ice front but its impact on calving depends on the time scale of

calving events. Undercutting increases the surface stress and decreases the bottom stress just as in the case of a shorter ice shelf and thus induces a similar type of calving. The influence of the stress field is however time dependent due to the viscous adjustment of ice. In our simulations, we find that if the undercutting is not large enough to produce calving within about 0.1 yr, then it will have no impact on calving. If calving occurs on shorter time scales, then undercutting significantly enhances the process. The high melt that produces undercutting, however, is not considered in our simulation. If the high melt is sustained, which depends on the seasonal variability of thermal forcing from the ocean, the time scale of undercutting will be longer. This conclusion may help reconcile the previous studies because it shows that the impact of undercutting depends on the time scale of calving events. We conclude that the impact of undercutting will be more significant for fast-moving glaciers with high calving rates than for slow moving glaciers with low calving rates. A high calving rate will give less time for the glacier to adjust viscously to the undercutting than for a slow calving glacier. As a conjecture, since glaciers with a high calving rate have more impact on the total mass balance, we conclude that undercutting is an important factor in the study of calving dynamics.

In this study, the simulations are conducted in a 2D flowband model with one crevasse propagation event. It would be of interest to generalize the present simulation to a 3D geometry with the inclusion of multiple crevasses and a moving ice front. In 3D, a better representation of the lateral shear and a complete surface/bed geometry will provide a more realistic context for the models. The simulation of a series of calving events with a train of crevasses over a long time period would provide more realistic information about how a glacier will respond to a calving event in terms of the migration of its grounding line and the evolution of its ice speed. It would also be useful to include in the current model the subcritical propagation or the damage mechanics, which is needed to improve the simulation of the initial propagation from an infinitesimal crevasse to a $\sim$1 m deep, $\sim$10 m wide crevasse

(*Weiss*, 2004; *Krug et al.*, 2014). With these additions, we would be in a better position to project calving events.

4.6 Conclusions

In this chapter, we presented our results on simulating calving and the crevasse propagation of TG using a two-dimensional flowband full-Stokes model coupled with the LEFM theory. We found that FS combined with LEFM produces crevasses consistent in width and depth with observations and produces calving events, whereas the HO and SSA models do not. The reason for the propagation of crevasses is the existence of a non-hydrostatic condition of ice immediately downstream of the grounding line, which is not accounted for in simplified models that assume hydrostatic equilibrium on the ice shelf. We also found that calving is enhanced in the presence of pre-existing surface crevasses, shorter ice shelves, or if the ice front is undercut. We conclude from our results that it is important to consider the full stress regime of ice in the grounding line region to replicate the conditions conducive to calving events, especially the non-hydrostatic condition that is critical to the propagation the crevasses.

Chapter 5

Modeling the Retreat of Thwaites Glacier under Enhanced Ice Shelf Melting

In this chapter, we present a study that simulates the evolution of Thwaites Glacier (TG) under enhanced ice shelf melting with various model configurations. First, we give an introduction of the importance of ice shelf melting to TG, the input data we use, and the setup of our simulations. Next, we describe our model results with different ice flow models and different ice shelf melt scenarios. We then discuss the cause of the differences among different model configurations and the stability of TG over the next century.

5.1 Ice Shelf Melting of Thwaites Glacier

Ice shelf melting is an important process for the ablation of the Antarctic Ice Sheet (AIS). The total amount of ice shelf melt is estimated to be 1454–1516 Gt/year, which is larger than

the estimated 755–1321 Gt/yr mass loss from calving (*Depoorter et al.*, 2013; *Liu et al.*, 2015; *Rignot et al.*, 2013). Similarly to calving, the direct impact of ice shelf melting on global sea level rise is negligible. However, the thinning of ice shelves reduces the buttressing to grounded ice sheet, speeds up the ice sheet and leads to grounding line retreat and mass loss over the entire ice sheet.

Thwaites Glacier (TG), located in the Amundsen Sea Embayment (ASE) of West Antarctica, is one of the glaciers experiencing the highest ice shelf melt rate in Antarctica. In the past few decades, the warming of the tropical Atlantic Ocean, the Indian Ocean and the cooling of the eastern Pacific changed the atmospheric circulation in West Antarctica and deepens the Amundsen Sea low through teleconnection (*Li et al.*, 2015). The deepening of the Amundsen Sea low strengthens the westerly wind, which modifies the ocean circulation and helps the warm Circumpolar Deep Water (CDW) to intrude into the ASE (*Spence et al.*, 2014; *Scambos et al.*, 2017). *In-situ* measurements in ASE conducted in 2007 have shown that the thermal forcing (difference between *in-situ* ocean temperature and the *in-situ* freezing point of seawater) at the ice front of TG is over $2°C$ below -300 m and reaches $4.34°C$ below -1200 m (Fig. 5.1). This warm water intrusion enhanced ice shelf melt under the ice shelf of TG. The mass loss from ice shelf melt is currently $\sim$97.5$\pm$7 Gt/yr (*Rignot et al.*, 2013).This process thins the ice shelf and triggers the dynamic mass loss of TG (*Schoof*, 2007; *Goldberg et al.*, 2009).

For a marine-terminating glacier, bed topography also plays a crucial role in controlling the grounding line stability. According to the marine ice sheet instability (MISI) theory, in 2D, a grounding line position is stable when sitting on a prograde bed, i.e., a bed elevation that increases in the inland direction, and unstable when sitting on a retrograde bed (*Weertman*, 1974). In 3D, glaciers on retrograde bed are conditional stable due to the buttressing from ice shelves and lateral drag (*Gudmundsson et al.*, 2012). The grounding line of the central trunk of TG is currently sitting on a subglacial ridge on the western part of the glacier.

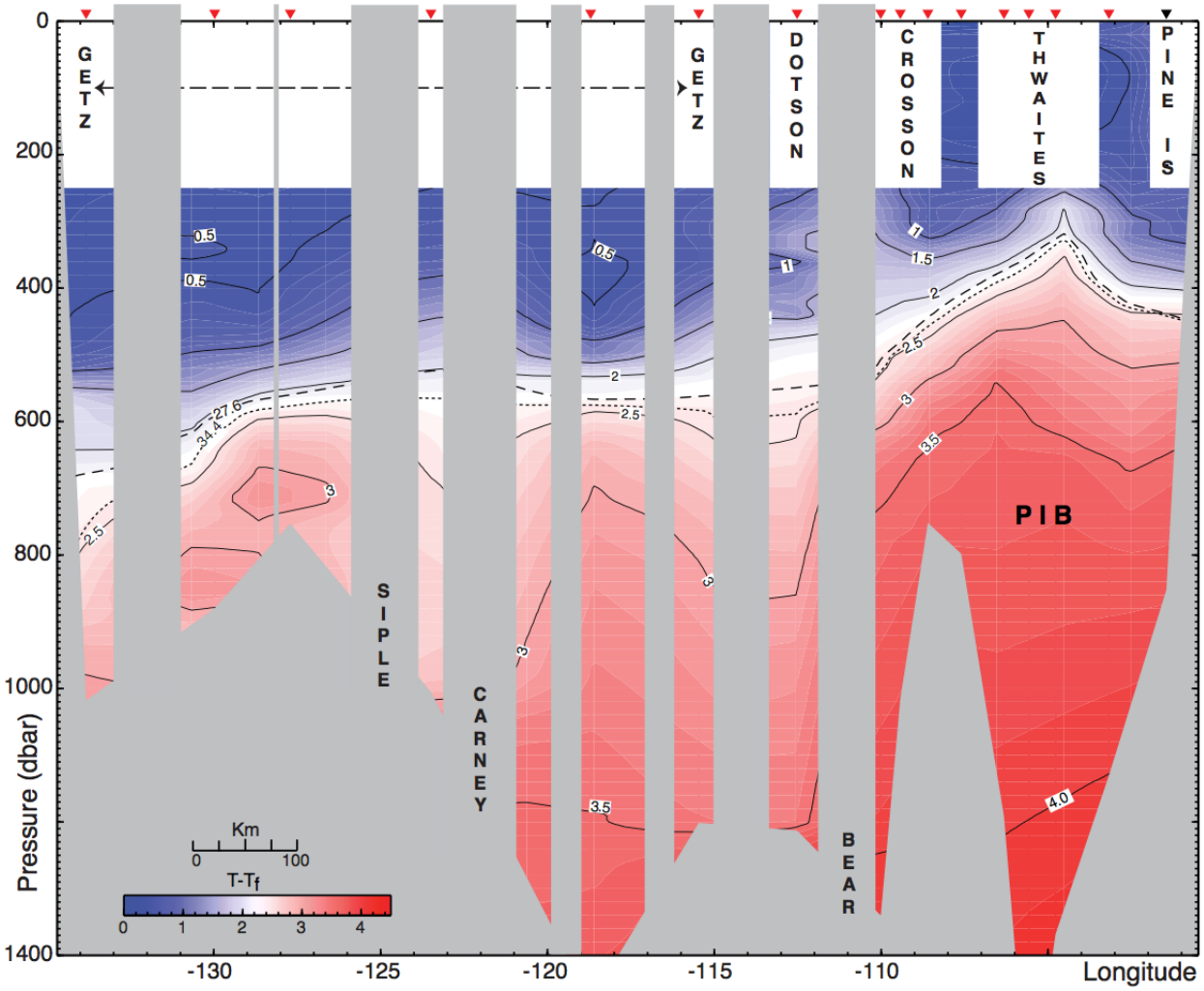

Figure 5.1: Thermal forcing across Amundsen Sea Embayment from conductivity-temperature-depth (CTD) measurements conducted in summer 2007 and 2009 (*Jacobs et al.*, 2012).

Upstream of the ridge, the bed is mostly retrograde until the ice divide (Fig. 5.2b), which indicates limited stability to changes (*Hughes*, 1981; *Rignot et al.*, 2014; *Joughin et al.*, 2014). Therefore, the initiation of retreat from enhanced ice shelf melting may lead to self-sustained retreat of the glacier. According to prior studies, TG may experience continuous and rapid mass loss in the future and may have already entered the phase of collapse, which would mean a 59 cm increase of global mean sea level (*Parizek et al.*, 2013; *Joughin et al.*, 2014; *Feldmann and Levermann*, 2015; *Seroussi et al.*, 2017).

To assess the future of TG, we need numerical models. Based on prior studies, TG will experience continuous and rapid retreat, however, the timing and extent of the projected retreat varies significantly among models (*Parizek et al.*, 2013; *Joughin et al.*, 2014; *Feldmann and Levermann*, 2015; *Seroussi et al.*, 2017; *Rignot et al.*, 2014; *Cornford et al.*, 2015). One important factor explaining the differences among models is that they employ different model configurations and ocean forcings, so it is not clear which model best captures the behavior of TG. To simulate the evolution of TG, it is important to model the grounding line migration accurately. The grounding line position is key to the stability of marine-terminating glaciers, but it is difficult to model numerically because the sharp transition from grounded ice to floating ice involves a transition in stress field (*Vieli and Payne*, 2005; *Nowicki and Wingham*, 2008; *Favier et al.*, 2012). A full-Stokes (FS) model is required in this transition region to capture the complete ice physics (*Durand et al.*, 2009a; *Morlighem et al.*, 2010). Most prior ice sheet models applied to TG, however, used simplified physics (*Seroussi et al.*, 2017; *Joughin et al.*, 2014). In that context, the treatment of ice shelf melt near the grounding line and the choice of the friction law may have a significant impact on the rate of grounding line retreat and glacier mass loss (*Seroussi et al.*, 2014; *Golledge et al.*, 2015; *Arthern and Williams*, 2017; *Brondex et al.*, 2017).

In this chapter, we simulate the dynamics and evolution of TG for 100 years using the Ice Sheet System Model (ISSM) (*Larour et al.*, 2012). To investigate the impact of different configurations, we apply three different stress balance models (FS and two approximations), two treatments of ice shelf melt near the grounding line, and two friction laws. For each of these twelve models, we employ six different ice shelf melt scenarios parameterized to match prior ocean model results and satellite observations and to encompass a realistic regime of ice shelf melt ranging from cold conditions with low access of CDW to the glacier to warm conditions with enhanced access of CDW. We compare the results from the different models and conclude on the evolution of TG over the coming century based on the model results.

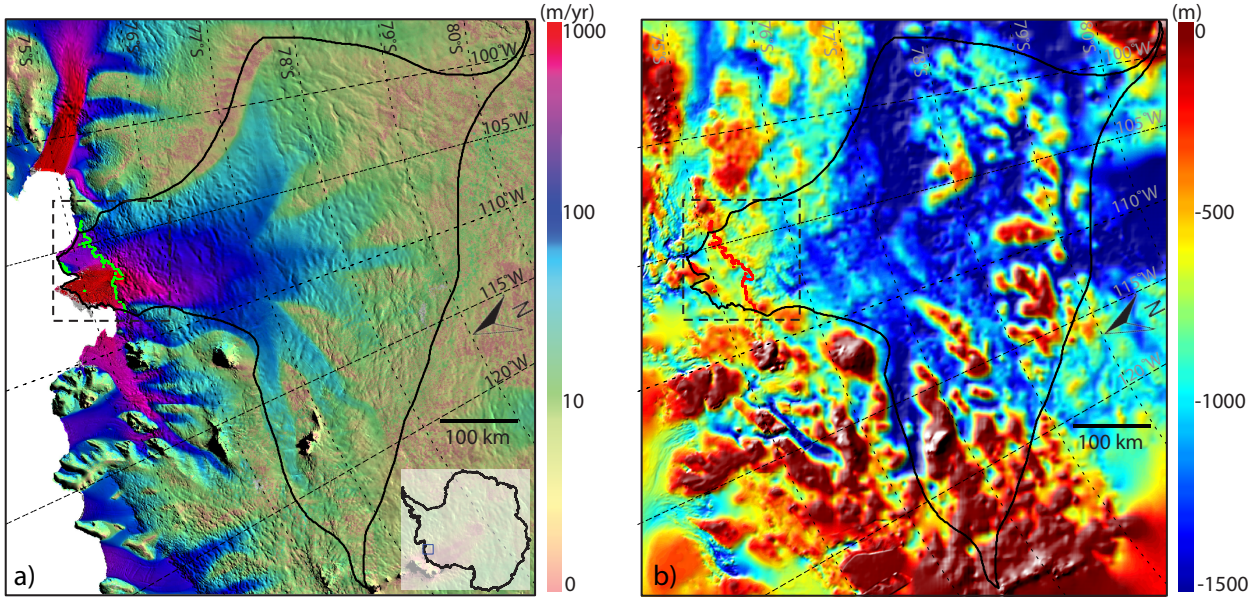

Figure 5.2: (a) Surface velocity of Thwaites in 2008 derived from InSAR (*Rignot et al.*, 2011a). (b) Bed elevation of Thwaites (*Morlighem et al.*, 2011; *Millan et al.*, 2017). The green line in (a) and the red line in (b) are the grounding line position in 2011 (*Rignot et al.*, 2011b). The black contour is the drainage basin of Thwaites and the black dashed box is the region shown in Fig. 5.7

5.2 Data and Methods

5.2.1 Data

We conduct numerical simulations of the ice flow of TG over its entire drainage basin (Fig. 5.2). We use BEDMAP-2 data for ice surface elevation and ice shelf draft elevation (*Fretwell et al.*, 2013), the bed elevation from mass conservation on grounded ice (*Morlighem et al.*, 2011, 2013) and the sea floor bathymetry from a gravity inversion beneath floating ice (*Millan et al.*, 2017). We use the surface temperature field from the regional atmospheric climate model RACMO2.3 (*Lenaerts and van den Broeke*, 2012) and the geothermal heat flux from *Shapiro and Ritzwoller* (2004) to compute the steady state temperature field of TG (*Seroussi et al.*, 2017). The surface mass balance is from the RACMO 2.3 (*Lenaerts and*

van den Broeke, 2012). The ice surface velocity (Fig. 5.2a) is from interferometric synthetic aperture radar for the year 2008 (*Rignot et al.*, 2011a).

5.2.2 Ice Flow Model

In this study, we follow the solution sequence described in Chapter 3 to solve the ice flow problem (Fig. 3.1). The three stress balance models, FS, HO and SSA are run and their results are compared.

During the simulation, the position of the grounding line lies within the elements of the mesh. Numerical models implement ice shelf melt in these partially floating elements differently. Some models apply melt in proportion to the floating area fraction of each element, while some models only apply melt to fully floating elements. In our simulations, we quantify the difference between these two types of implementations by running both of them. We refer these two sets of experiments as Melt and Nomelt in this thesis.

We also apply two different friction laws. The first one is a linearzed Weertman friction law, where the basal drag is proportional to basal velocity (q=0 and p=1 in equation 2.20):

$$\boldsymbol{\tau_b} = -C\boldsymbol{v}_b \tag{5.1}$$

The second one is a Budd friction law, where the basal drag is proportional to both the basal velocity and the effective pressure (the difference between overburden ice pressure and hydrostatic pressure) at the base (q=1 and p=1)

$$\boldsymbol{\tau_b} = -CN\boldsymbol{v}_b \tag{5.2}$$

$$N = \rho_i g H + \rho_w g b \tag{5.3}$$

Here, to focus on the impact of the effective pressure, we choose to use linear friction laws (p=1). However, non-linear friction laws could lead to different model behaviors. We refer to these two sets of experiments as Weertman and Budd experiments.

The ensemble of stress balance models, ice shelf melt implementations, and friction laws lead to 12 different sets of experiments.

The boundary conditions are the same for all sets of experiments apart from the friction law as described in chapter 2. The calving front position is kept constant throughout our simulations.

5.2.3 Ice shelf melt scenarios

To simulate the response of TG to enhanced ice shelf melting, we run the model with six different ice shelf melt scenarios. In all scenarios, the ice shelf melt rate is parameterized as a function of ice shelf basal elevation and is set to 0 above 150 m depth. In the first scenario, the ice shelf melt rate linearly increases to a maximum of 80 m/yr at 1000 m depth. Below 1000 m depth, the ice shelf melt rate is kept constant at 80 m/yr. This scenario originates from simulations using the coupled ISSM/MITgcm ice-ocean model for year 1992 (Fig. 5.3) (*Seroussi et al.*, 2017). Year 1992 was a cold year with a low ice shelf melt rate in ASE compared to the average over the past 30 years (*Schodlok et al.*, 2012), which makes this scenario representative of relatively cold ocean conditions. With this parameterization, the mass loss from ice shelf melt for TG is 73.7 Gt/yr at the beginning of the simulation. This value is close to the estimated ice shelf melt of 69 Gt/yr from *Depoorter et al.* (2013) and 24% less than the 97.5 Gt/yr for the years 2003-2008 in *Rignot et al.* (2013) .

In the other five scenarios, we change the maximum ice shelf melt rate and the depth where the maximum melt occurs. To constrain the range of ice shelf melt rates, we compute the

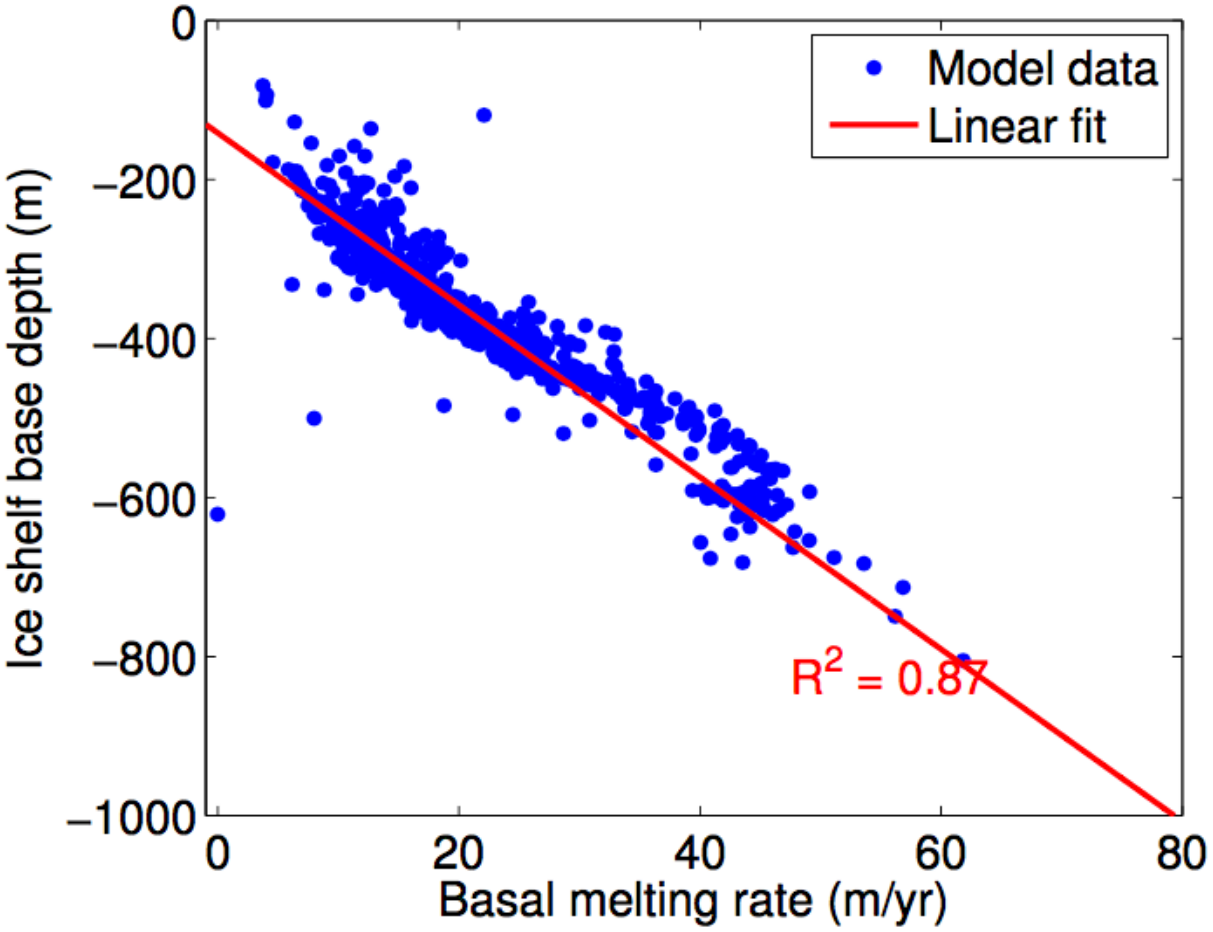

Figure 5.3: Ice shelf melt rate computed from a coupled ice-ocean model as a function of ice bottom depth (blue dots) and parameterized ice shelf melt rate (red line) from linear regression (*Seroussi et al.*, 2017).

ice shelf melt rate using the mass conservation method as in (*Rignot et al.*, 2013):

$$\dot{m}_s - \dot{m}_b = \frac{\partial H}{\partial t} + \nabla \cdot (H\bar{\boldsymbol{v}}) \tag{5.4}$$

where $\dot{m}_b$ is the ice shelf melt rate, $\dot{m}_s$ the surface mass balance, H the ice thickness and $\bar{\boldsymbol{v}}$ the depth average velocity. We use the same dataset in this computation as we used in our simulations: 2008 surface velocity from InSAR, ice thickness from Bedmap2, and the bathymetry of ASE (*Rignot et al.*, 2011c; *Fretwell et al.*, 2013; *Millan et al.*, 2017). We then make the assumptions that the depth-averaged velocity is equal to the surface velocity

and $\frac{\partial H}{\partial t}$ (one magnitude smaller than $\dot{m}_b$ in TG) is equal to 0. In this way, we found the maximum ice shelf melt rate is ∼125 m/yr, or 50% larger than the first scenario, and the high melt mostly occurs near the grounding line (Fig. 5.4). Field measurements are also used to estimate the ice shelf melt rate of TG. In 2007, which is a warm year, the nearby Pine Island Glacier experienced ∼50% more melt compared to 1992 (*Schodlok et al.*, 2012). Therefore, in the second scenario, we increase the maximum ice shelf melt rate by 50% to 120 m/yr to represent warm ocean conditions.

As *Jacobs et al.* (2012) showed in 2007, the thermal forcing, which is the difference between the *in-situ* ocean temperature and the *in-situ* freezing point of seawater, exceeded +4°C at the ice front of TG, which implied almost undiluted CDW (Fig. 5.1). This indicates that the potential of further increase in ice shelf melt rate is limited. Therefore, in the third scenario, we choose to increase the maximum ice shelf melt rate by another 40 m/yr to 160 m/yr to represent extreme warmth.

We also vary the depth at which the ice shelf melt rate reaches its maximum. Ocean observations show that the bottom of the thermocline has been relatively constant at 700 m depth in the past two decades in ASE (*Dutrieux et al.*, 2014). Accordingly, we run three additional ice shelf melt scenarios with the maximum ice shelf melt rate (80 m/yr, 120 m/yr, 160 m/yr) occurs below 700 m instead of 1000 m (Fig. 5.5).

Overall, we run a total of 72 simulations (6 ice shelf melt scenarios by 12 models). We name our simulations from the combination of their ice shelf melt scenario, stress balance equation, ice shelf melt treatment and friction law. For instance, Exp. 80_1000_FS_Nomelt_Budd represents the experiment conducted with a maximum of 80 m/yr ice shelf melt rate below 1000 m depth, FS stress balance model, ice shelf melt only applied to fully floating elements, and a Budd friction law.

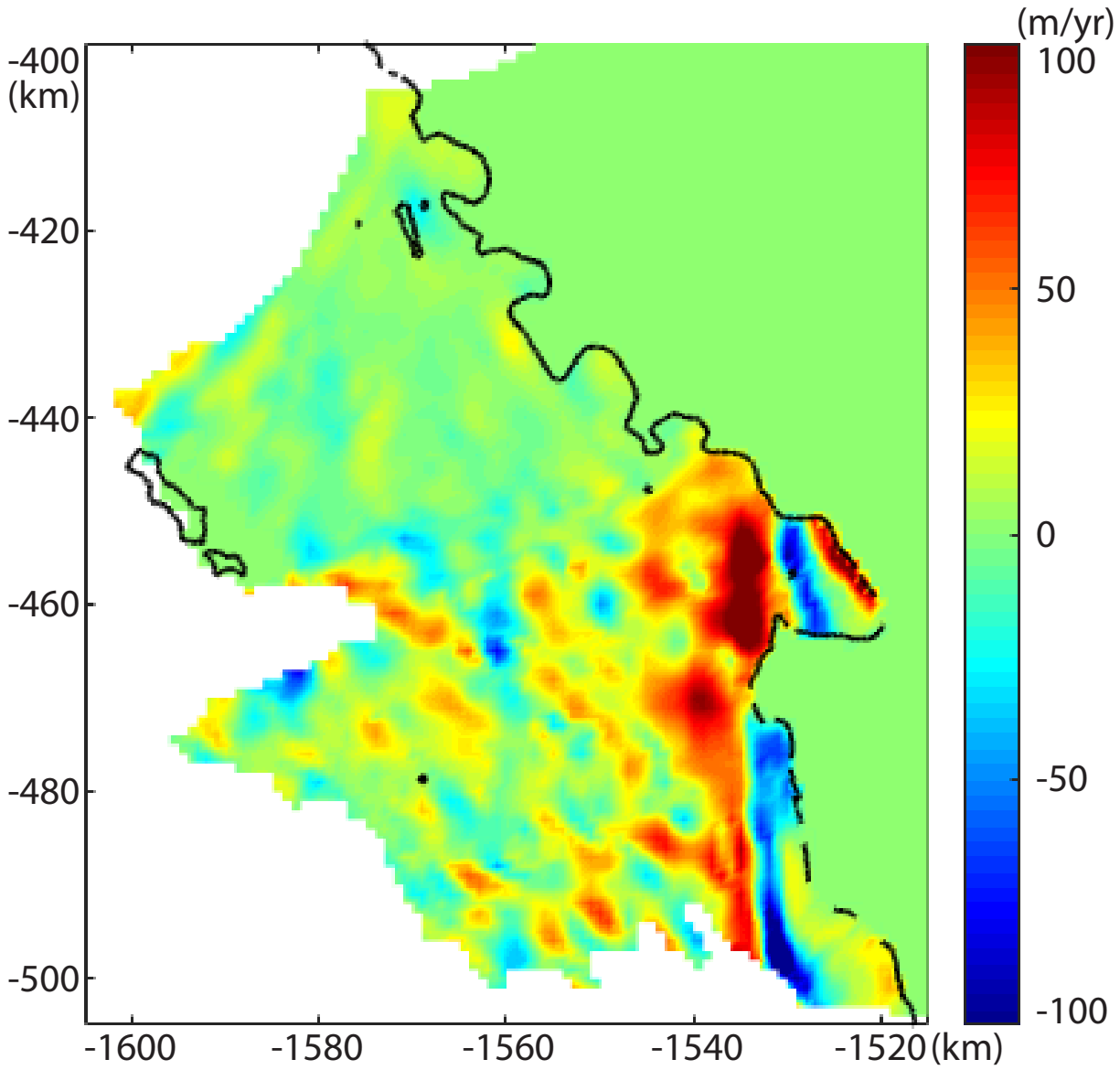

Figure 5.4: Ice shelf melt rate of Thwaites Glacier computed from mass conservation.

5.2.4 Initial model setup

The mesh is constructed using an anisotropic metric based on ice surface velocity and distance to the grounding line, and comprises the entire drainage basin of TG. The horizontal mesh spacing is 300 m in the grounding line region, progressively increasing to 10 km in the interior

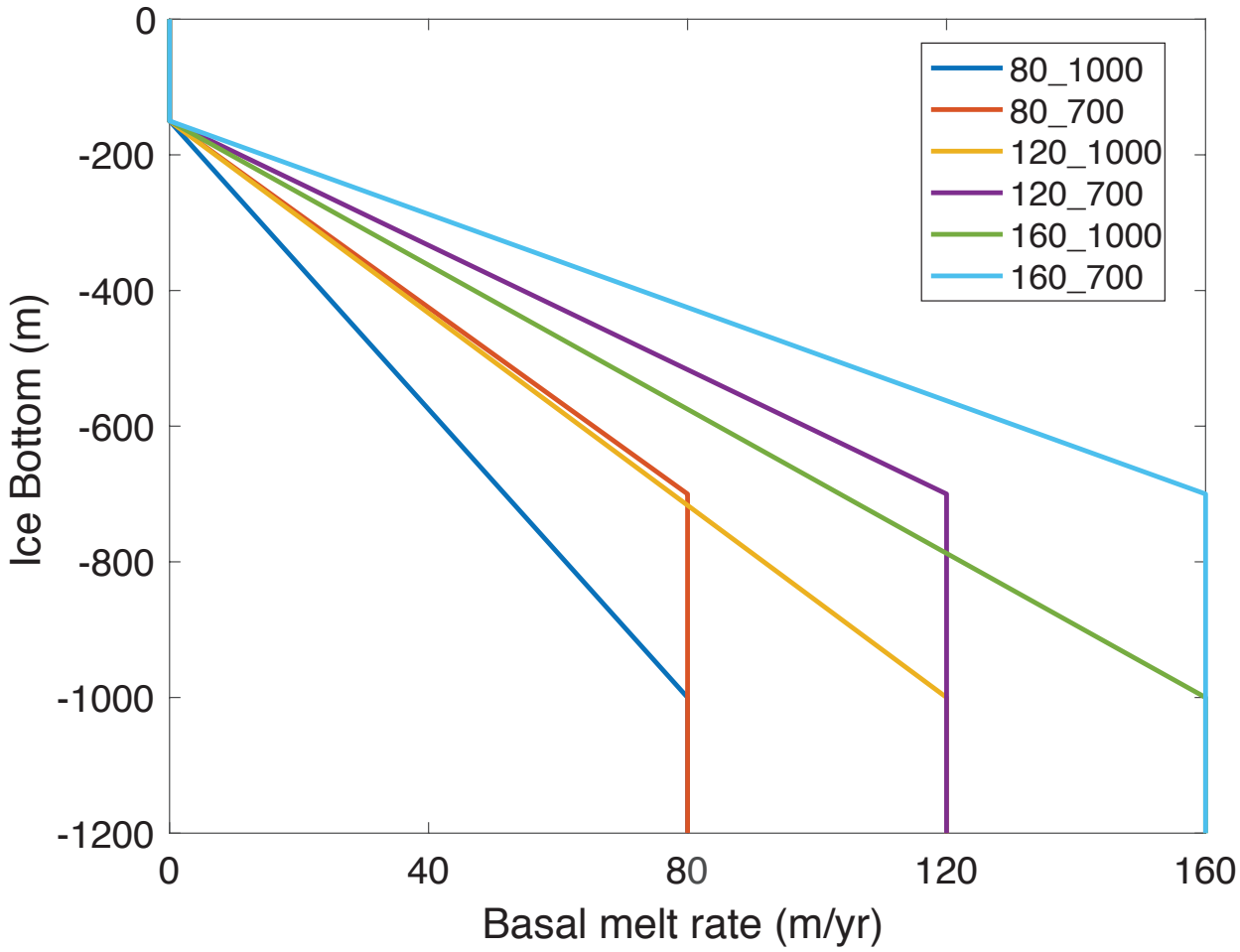

Figure 5.5: Ice shelf melt rate parameterization for all sets of experiments.

of the ice sheet. Vertically, the domain is divided into 8 vertical layers that are denser at the bottom. In total, our mesh includes 561,799 triangular prismatic elements.

In order to relax the model while maintaining a good fit with surface observations, we adopt the following procedure. We first conduct an inversion of the basal friction coefficient over the grounded ice and of the ice viscosity parameter over the floating ice to best match modeled surface velocity with the observed surface velocity (*Morlighem et al.*, 2010). After the inversion, we find a rapid change in ice velocity of a few 100 m/yr at the grounding line in transient simulations due to inconsistencies between datasets (*Seroussi et al.*, 2011). To avoid this problem, we run the model for 0.5 yr to relax the model and perform a second inversion. We repeat this procedure 4 times until we reach a stable solution. After these

iterative steps, the modeled velocity is consistent with observations at the beginning of transient simulations, within 50 m/yr (Fig. 5.6). Note that the inversions for ice viscosity parameter and basal friction are conducted independently for the three ice flow models so that each model has its own, self-consistent initial set up. The inversions are conducted with the Weertman friction law. For the Budd friction law, the friction coefficient is computed directly through $C_b = C_w/N$ to ensure same initial basal conditions for the two sets of experiments.

FS is more sensitive to mesh resolution than HO and SSA and requires a higher mesh resolution in the interior than other models in order to converge. To avoid the computational cost of a high resolution FS modeling over the entire basin, we use a tiling method to apply FS within 150 km of the grounding line and HO in the interior (*Seroussi et al.*, 2012). In this manner, we insure that the FS model is computationally efficient, the results are reliable, and the regions where the grounding line retreats are modeled using FS.

5.3 Results

5.3.1 Inversion

The inversion results are shown in Fig. 5.6. The inversion is not supported with the tiling method. Therefore, for the FS model, we do inversion with FS over the whole domain. Then, we combine the inferred basal friction coefficient from HO and FS for the basal friction coefficient of the FS model. Therefore, the inferred basal friction coefficient is the same for HO and FS in the interior of TG. The pattern of basal friction coefficient is the same for all models, with high friction near the ice divide and low friction in the deep basin. SSA needs a smaller friction coefficient than HO and FS to match observed velocity because of the neglected vertical shear. The inferred ice viscosity parameter over floating ice is also

similar for the three models with stiff ice near the grounding line and soft ice at the junction between the eastern ice shelf and the main trunk.

After the inversion, the mismatch between modeled and observed surface velocity is small, i.e. within 200 m/yr in the fast moving region and within 30 m/yr for HO and SSA in the interior. For FS, the difference is large in the interior, about 100 m/yr due to the tiling method, but this difference has limited impact on our results since it takes place far from the grounding line region (>100 km) and the changes in that region are relatively small.

5.3.2 Grounding line retreat and mass loss

In transient simulations, the results display a consistent, general pattern of retreat, with different magnitude of mass loss and rates of grounding line retreat. Overall, the grounding line retreats faster on the eastern side of the glacier and tends to remain stable on the western side. A sustained mass loss is obtained for all simulations.

The evolution of the grounding line position for all 12 models with the lowest (80_1000) and highest ice shelf melt (160_700) scenarios is shown in Fig. 5.7. The grounding line retreat shows distinct features on the eastern and western sides due to bed topography. On the eastern side, the grounding line retreats continuously in all experiments for 30-65 km. The main difference among the simulations is whether and when the grounding line retreats over the subglacial ridge 35 km upstream of its present location. On the western side, the grounding line is stable with only small retreat in all cases except for the Melt experiments in high ice shelf melt scenarios. However, once the grounding line starts to retreat in the west, it retreats rapidly at more than 1 km/yr. The changes in grounded area are consistent with the grounding line migration (Fig. 5.9), i.e., limited change when the grounding line sits on a subglacial ridge and faster change when the grounding line retreats along retrograde or flat bed.

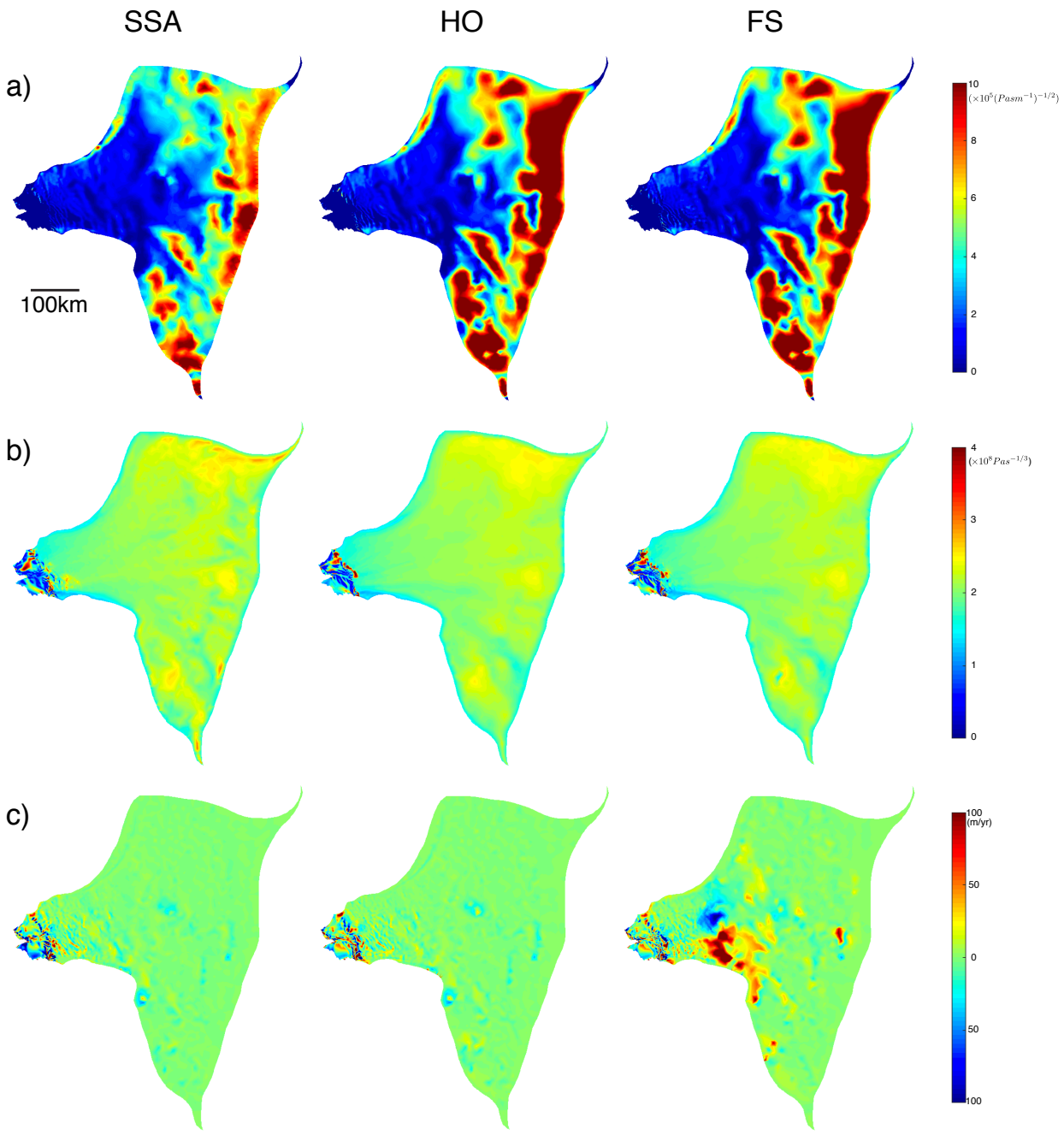

Figure 5.6: Inversion results. a) Inferred basal friction coefficient for SSA, HO and FS models. b) Depth average of inferred ice rheology for the three models. c) Difference between inferred surface velocity and observed surface velocity for the three models.

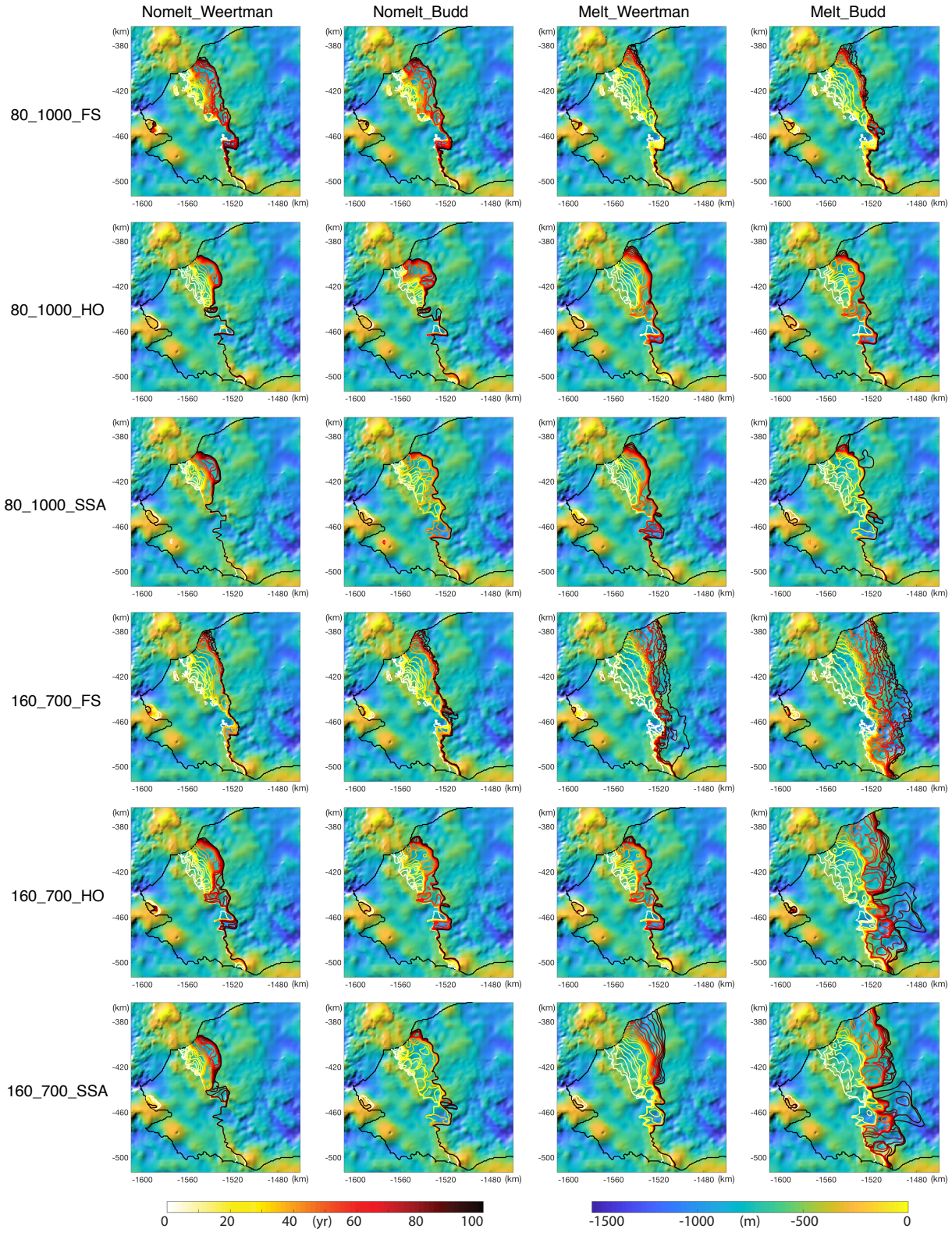

Figure 5.7: Grounding line evolution of all models with the two end members ice shelf melt scenarios, overlaid on the bed elevation map of Thwaites Glacier, West Antarctica. Each panel represents one simulation. Within each panel, the grounding line positions are plotted every 5 years.

Along with the retreat of the grounding line, strong surface thinning and mass loss is produced during all simulations. The average surface thinning rate is shown in Fig. 5.8. In the region where the grounding line retreats, the average surface thinning rate is over 5 m/yr. The thinning signal also propagates upstream. In all simulations where the grounding line does not retreat over the western subglacial ridge, > 1 m/yr thinning rate is found within 70–150 km upstream of the initial grounding line position on the eastern side. On the western side, the thinning rate is relatively small. In the experiments where the western ridge is retreated over, surface thinning becomes more uniform and spread more upstream. At the end of these simulations, the average thinning rates are > 1 m/yr 160-220 km upstream of the current grounding line across the whole glacier width.

The mass loss is significant and rapid in all simulations (Fig. 5.9). The loss in volume above flotation (VAF) is closer to linear than grounded area loss due to the relatively constant thinning rate in the interior. Combining all simulations, the VAF loss is equivalent to a 15–42 mm global mean sea level (GMSL) rise in 100 years.

5.3.3 Difference among simulations

The response of TG to ocean melting differs when using different stress balance models, ice shelf melt implementations and friction laws. Among the three stress balance models, FS shows more grounding line retreat than HO and SSA, except in the Melt_Weertman experiments, where HO retreats the most. In the Nomelt and Melt_Budd experiments, FS produces 5-40% more grounded area loss than HO and SSA. In the Melt_Weertman experiments, FS has 10% less retreat than HO and 15% more than SSA. In the VAF loss perspective, the three models are closer to each other. SSA shows more VAF loss in the Budd experiments, while FS shows more VAF loss in the Weertman experiments. The overall differences are within 20%.

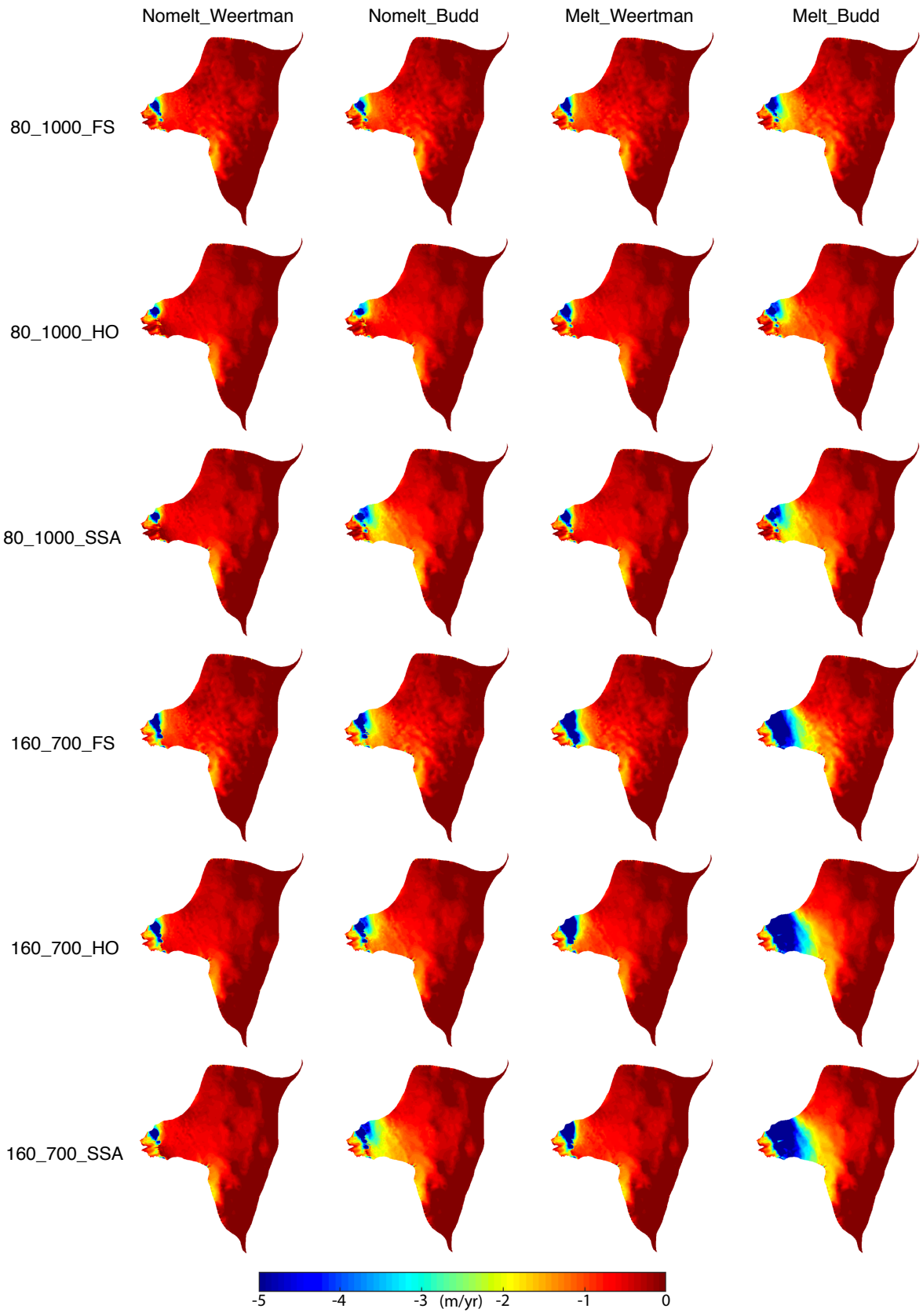

Figure 5.8: Average surface thinning rate over the whole simulations of all model configurations with the two end member ice shelf melt scenarios.

The grounding line retreat rate is significantly reduced in the Nomelt experiments compared to the Melt experiments. The total grounded area loss is reduced by 35-65% and the VAF loss is reduced by 15-40%. The choice of friction law also has a significant impact on the results. The Budd friction law produces more grounding line retreat (10-50%) and more VAF loss (15-90%) than the Weertman friction law. The Budd experiments also display a higher sensitivity to ocean forcing than the Weertman experiments.

Different ice shelf melt scenarios have significant impact on the behavior of TG. A higher ice shelf melt rate always leads to more retreat. However, the sensitivity to changes in ice shelf melt rate varies among the models. The Melt experiments with FS or HO and Budd friction law are more sensitive to ocean forcing than the Nomelt experiments with SSA and Weertman friction law.

5.4 Discussion

5.4.1 Impact of the stress balance models

In our simulations, the stress balance models produce different results for several reasons. First, the model physics are different. With the inclusion of vertical shear and bridging effects in the stress field, the ice viscosity in FS is lowered, which leads to a larger acceleration as the grounding line retreats. In the MISMIP3D experiments, for example, using the same initial setting, the modeled ice velocity of FS is faster than HO by 0-5%, and HO is faster than SSA by another 0-5% (*Pattyn et al.*, 2013). Second, the grounding line positions are computed differently. For HO and SSA, it is computed through hydrostatic equilibrium, which compares the bottom water pressure with the overburden ice pressure. For FS, the bottom water pressure is compared with the normal stress at the base, which deviates from the overburden ice pressure by a few percent. In the grounding line region, and in particular,

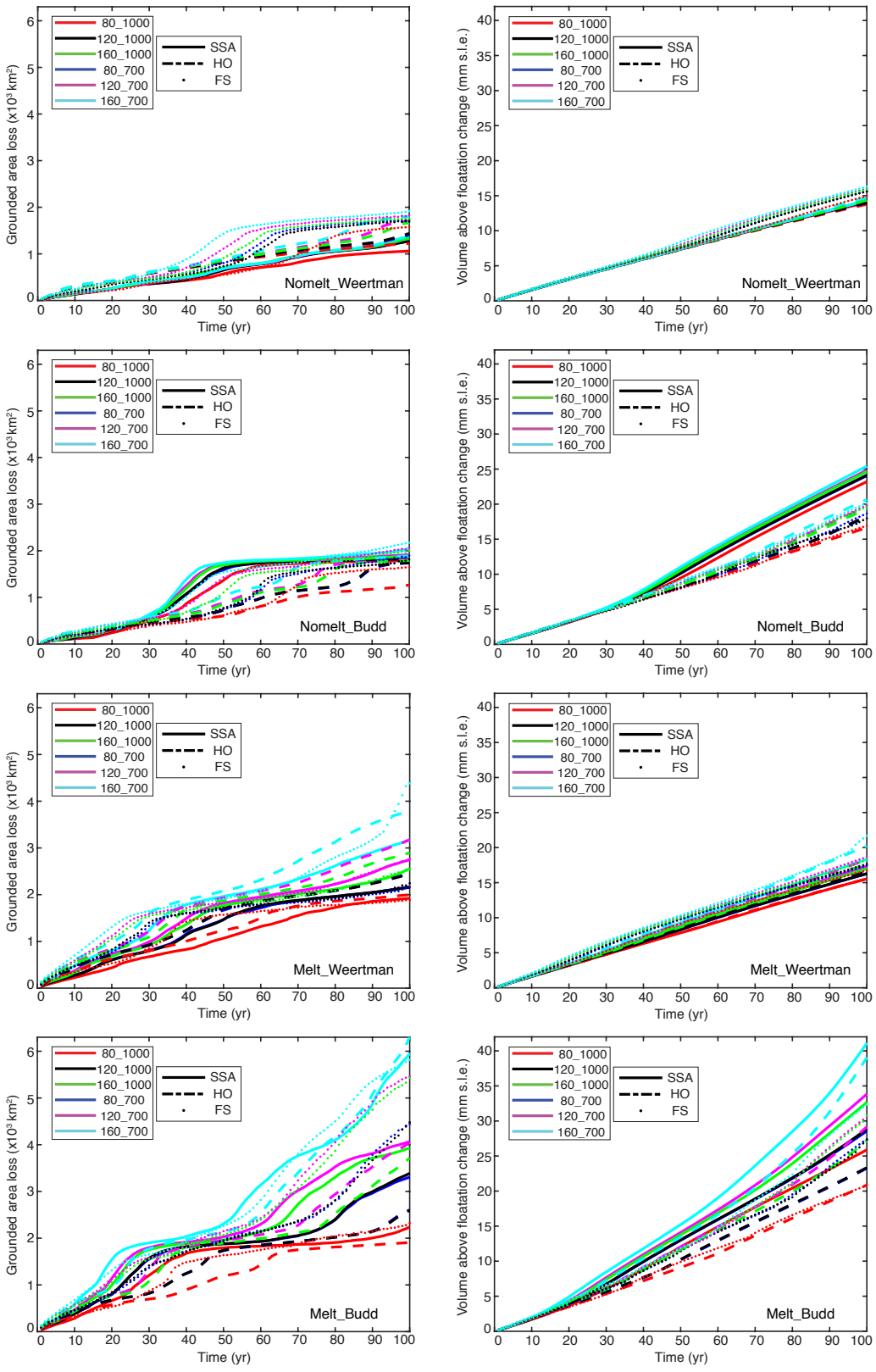

Figure 5.9: Grounded area and volume above flotation (VAF) loss of Thwaites Glacier, West Antarctica in all experiments.

in the bending zone of the glacier, ice is pushed below hydrostatic equilibrium because of the bending moment of the ice as it tries to reach hydrostatic equilibrium in the ocean water (*Rignot*, 2001; *Yu et al.*, 2017). As a result of this non-hydrostatic condition, the vertical velocity is high downstream of the grounding line, which produces high vertical shear that decreases the normal stress at the base. Moreover, the horizontal stretching of ice is large in the grounding line region, which reduces the normal stress at the ice base (*van der Veen and Whillans*, 1989; *Pattyn et al.*, 2013).

Numerical issues also contribute to the differences among the models. We conduct inversions for each model separately to make sure that they best fit the observations. Hence, the initial conditions are slightly different for each model, which sets them up on different trajectories. In transient simulations, small differences in initial conditions may accumulate with time and lead to further significant differences in the model outcomes. Here, SSA has a higher rate of VAF loss than grounded area loss with respected to HO and FS. This is due to the higher thinning rate in the interior simulated by SSA. This sensitivity to initial conditions indicates that we need better constraints for the inversion process. For instance, we should infer the basal friction coefficient and ice viscosity parameter using a series of observed velocities, as in *Goldberg et al.* (2015), rather than a single velocity map.

In summary, the FS model has more complex physics compared to HO and SSA and leads to faster grounding line retreat, especially over subglacial ridges. The difference between FS and simplified models depends on the bed topography. The limitation of FS is computational. FS is 10 times slower than HO and 100 times slower than SSA. In our results, however, the impact of different stress balance models is smaller than the impact of ice shelf melt treatment and friction law. Meanwhile, initial conditions are also critical to consider when comparing model results.

5.4.2 Impact of the ice shelf melt treatment near grounding line

Our results also show that whether to apply ice shelf melt in the partially floating elements changes the results significantly, which is consistent with previous studies (*Golledge et al.*, 2015; *Arthern and Williams*, 2017). Theoretically, these two methods should have the same results if the mesh resolution is small enough. However, this is not achieved with our 300 m resolution and may therefore be difficult to achieve numerically. For the partially floating elements, it is expected that some ice shelf melt would occur in the floating portion, so not applying any ice shelf melt might underestimate the mass loss. In the newly ungrounded cavity, the ice shelf melt rate may not be as high as the previously floating area due to its limited access to warm water. The removal of ice at the base in partially floating elements may also lead to unrealistic thinning upstream of the grounding line due to the implementation of the mass transport equation. Therefore, the model may overestimate mass loss if ice shelf melt is applied in the partially floating elements. We also conducted the same simulation with coarser and finer mesh resolutions with SSA and the Nomelt experiments are showing less sensitivity to mesh resolutions than the Melt experiments.

5.4.3 Impact of the friction laws

The introduction of an effective pressure term in the Budd friction law produces more retreat and mass loss compared to the Weertman experiments. With the Budd friction law, the basal drag is reduced when the ice is thinning, which in turn accelerates further retreat and thinning, forming a positive feedback. In our results, the difference between Weertman and Budd experiments is larger in VAF loss than grounded area loss due to the changes in the interior. Once the friction is reduced with the Budd friction law, ice thinning increases and propagates inland to produce more VAF loss than with the Weertman experiments.

This result indicates that the difference in grounding line retreat between these two sets of experiments diverges with time as the upstream thinning signal evolves.

The underlying assumption for the Budd friction law is the existence of a subglacial drainage system. Previous studies have revealed that such systems exist in West Antarctica and are connected to the ocean (*Gray et al.*, 2005; *Fricker et al.*, 2007; *Le Brocq et al.*, 2013). Therefore, it might be more reasonable to use a Budd friction law in the grounding line region of TG. However, in the interior ice sheet, such drainage system may not be present and the use of the Budd friction law could overestimate the total mass loss. Recently, *Tsai et al.* (2015) proposed a friction law that incorporates both a Weertman friction law and a Coulomb friction law, which might work for both the grounding line and the interior regions. This method requires two sets of basal friction coefficients, which is difficult to infer in a real glacier and remains beyond the scope of this study.

5.4.4 Impact of bed topography and ocean forcing

Despite the differences among these models, the overall results are similar as the glacier retreats along the same preferred path. The major difference among the models is on the time it takes for each model to overcome ridges in bed topography along the pathway of the retreat. In all simulations, TG experiences grounding line retreat and mass loss over the entire period, which is consistent with previous studies (*Joughin et al.*, 2014; *Feldmann and Levermann*, 2015; *Seroussi et al.*, 2017). The retreat rate is highly dependent on bed topography. On the eastern side, there are three subglacial ridges that provide temporary stability to the glacier. The current grounding line position is on the retrograde side of the first ridge on the east. The second ridge is 35 km upstream. In the Nomelt experiments, the grounding line positions are still sitting on this ridge after 100 years. In the Melt experiments, all simulations except the 80_1000 ones have their grounding line retreat over this ridge, with

the timing varying from 55 to 90 years. The third ridge is another 25 km upstream. None of our simulations show grounding line retreats over this ridge within one century. The slope of the third ridge is similar to the second ridge. We therefore expect this ridge to have a similar stabilizing effect as the second ridge.

The subglacial ridge that has the strongest stabilizing effect is the western subglacial ridge where the grounding line is currently sitting on. In the Nomelt experiments, the grounding lines are stable in the west. In the Melt_Weertman experiments, only the FS model with the highest ice shelf melt rate has its grounding line retreat over the ridge at year 95. In the Melt_Budd experiments, the grounding line retreats over this ridge for the three high ice shelf melt scenarios (160_700, 160_1000, 120_700). Further upstream, the bed slope of TG is retrograde until the ice divide. Once the grounding line retreats over the western ridge, it is not clear how the retreat of the grounding line could be stopped.

The impact of ocean forcing is most significant in the Melt_Budd experiments and is relatively small in the Nomelt experiments. The difference is due to the grounding line retreat rate in these experiments. In the scenario where the grounding line is constantly retreating, a higher ice shelf melt rate will remove ice in the newly ungrounded area more rapidly and reduce the buttressing force on the inland ice faster, which leads to further retreat. If the grounding line position is relatively stable, however, a higher ice shelf melt rate will only act in areas where the ice is already floating. The removal of ice is limited in this region as the ice bottom evolves to a steady shape and the reduction of buttressing becomes limited.

In our simulations, the effect of changing the depth of maximum melt from 1000 m to 700 m is similar to increasing the maximum ice shelf melt rate by 50% (80_700 v.s. 120_1000 and 120_700 v.s. 160_1000). This is because the bed elevation between the current grounding line and the upstream subglacial ridges is between 800 and 500 m depth, which makes the melt rate at this depth particularly important. If warm ocean water intrudes at 700 m depth, as observed on Pine Island Glacier, or above, the retreat of TG will be more rapid, even

without increasing the maximum ice shelf melt rate. Indeed, the bathymetry in *Millan et al.* (2017) suggests that the main points of entry of CDW into the sub-ice-shelf cavities of TG have a maximum depth of 700 m.

5.4.5 Contribution to global sea level rise

The contribution to global sea level rise revealed by our simulations spread a large range from 14 to 42 mm in the next 100 years. However, in the first 30 years, all models suggests a global sea level rise of 5 mm, or 0.18 mm/yr. This rate is consistent with the satellite observations of 0.14 mm/yr in 2014, which kept increasing in the past decades. Previous modeling studies also have similar estimations, ranging from 0.15 mm/yr to 0.25 mm/yr (*Joughin et al.*, 2010; *Cornford et al.*, 2015; *Seroussi et al.*, 2017). After 30 years, the retreat of TG would continue, whether the retreat rate will accelerate is highly dependent on the numerical model used and a longer time record of observations is needed to know which model best reproduce the observational period.

5.5 Conclusions

In this chapter, we simulate the response of Thwaites Glacier, West Antarctica to varying model configurations and ice shelf melt scenarios. We find that the stress balance approximations, the treatment of ice shelf melt near the grounding line, the friction law, and the ice shelf melt rate parameterization all affect the retreat of TG significantly. Different model configurations affect the results mainly through the timing for the grounding line to retreat past subglacial ridges; different ice shelf melt rates mainly affect the retreat rate when the grounding line is retreating along retrograde portions of the bed. Despite the differences, however, all models follow similar trajectories and concur to indicate that TG will continue

to retreat at a rapid rate over the next century, under both cold and warm ocean water scenarios. The retreat is controlled by the bed topography. Subglacial ridges on the eastern side will only moderately delay the retreat, whereas the western ridge provides the most stability for the glacier, for at least the next several decades. Once the grounding line retreats past the western subglacial ridge, our simulations suggest that there will be no further stabilization of the glacier and the retreat will become unstoppable over the next 100 years. Our simulations project a 5 mm global mean sea level contributions from TG in the next 30 years, and 14-42 mm in the next 100 years.

Chapter 6

Conclusions

6.1 Summary of Major Results

Thwaites Glacier (TG), West Antarctica, is experiencing dramatic changes and is one of the largest sources for the mass loss in the Antarctic Ice Sheet (AIS). Making reliable estimation of the future evolution of TG is crucial for global sea level projections. The rapid mass loss of TG is mainly caused by the dynamical changes induced from the loss of buttressing from its ice shelf through calving and ice shelf melting.

Numerical ice sheet modeling has developed rapidly in the last decade. There are various model configurations can be adopted. However, their differences and the impact of numerical implementations are unclear. The full-Stokes (FS) model is now affordable to solve due to the growth of computing power. Compared to the widely used simplified models, the FS model fully captures the stress field of ice which makes it more accurate in modeling the non-hydrostatic behavior of ice, i.e. crevasse propagation and grounding line dynamics.

In this study, we present the validation of the FS model and its application on TG. We simulate the calving dynamics of TG combining FS model with the linear elastic fracture mechanics (LEFM) theory. We also simulate the response of TG to enhanced ice shelf melting while investigating the impact of different model configurations.

We first complete the MISMIP and MISMIP3D experiments with our model. Our model results are consistent with other models (especially other FS models) and theoretical analyses. In the 2D experiments, the grounding line position of our model displays hysteresis over an overdeepening on the bed. In the 3D experiments, our model displays accurate grounding line migration in response to the changes in the basal friction coefficient. The reversibility of the grounding line is also validated.

We then combine our 2D flowband model with LEFM to model the propagation of crevasses of TG. We use the ice flow model to compute the ice velocity and stress field. The LEFM is then applied to compute the propagation of surface and basal crevasses according to the stress field of ice.

The steady state crevasse depth from the FS model matches well with observed crevasses on TG, while results from simplified models do not. We find that crevasses that initiated near the grounding line have greater depth than crevasse initiated downstream. We propose that this condition is caused by the non-hydrostatic condition near the grounding line, where the ice is below hydrostatic equilibrium, which results in larger water pressure that tends to propagate basal crevasses.

To better understand what conditions favor crevasse propagation and calving, we conduct more experiments with altered initial geometry. We find that the shortening of ice shelves facilitates crevasse propagation and calving, which forms a positive feedback. We also find that crevasses grow rapidly with the presence of initial surface crevasses near the grounding line. This indicates that the ice shelf is difficult to form with pre-existing surface crevasses.

Lastly, our experiments show that undercutting is more important for glaciers with high calving rates than glaciers with low calving rates as high calving rates allows the glacier less time to adjust viscously.

In the last part of this thesis, we apply our 3D model on TG to study its response to enhanced ice shelf melting and the impact of different model configurations. We conduct our simulations with twelve model configurations with different stress balance models, treatment of ice shelf melt near the grounding line, and friction laws and six ice shelf melting scenarios based on observations.

Our experiments show that both model configuration and ice shelf melt rate have significant impact on the retreat of the glacier. The FS model is showing more grounding line retreat than the HO and SSA models in most experiments. Yet, the initial conditions also produce large differences in the results, especially in the mass loss perspective. Apply ice shelf melt on half floating elements can enhance grounding line retreat significantly compared to apply ice shelf melt only to fully floating elements. This difference is expected to diminish as mesh resolution increase to infinitely small, which, however, is hard to achieve numerically. The Budd friction law leads to more mass loss compared to the Weertman friction law due to the inclusion of the effective pressure, especially in the interior region. A higher ice shelf melt rate would accelerate grounding line retreat and thus mass loss than a lower rate. This difference is more significant during the phase when the glacier is retreating than the phase when the glacier is relatively stable.

Despite all the differences among the experiments, we found sustained grounding line retreat and mass loss in all simulations. The retreat rate and retreat pattern are highly controlled by the bed topography. According to our simulations, TG would retreat fast on the eastern side while stay relatively stable on the western side due to the present of a subglacial ridge. Once the glacier retreats over this ridge, however, there would be no more topographic features to stabilize it until the ice divide. Combining all our results, we project a consistent

5 mm contribution of TG to global sea level rise in the next 30 years, which is similar with the current rate. After 30 years, the sea level contribution of TG depends on model configurations and ice shelf melt rate parameterizations, with values ranging from 14 to 42 mm in the next 100 years.

6.2 Limitations and Future Perspectives

The mass loss of TG and other ice sheets is an important source to global mean sea level (GMSL) rise. In this thesis, we provide some insights in modeling calving and ice shelf melting of TG, two controlling factors of its mass loss. However, to have a better understanding of the role of ice sheets to the GMSL in the current warming climate, more studies are needed.

First of all, more observations are of great need. Currently, there are rare direct observations of calving because it happens irregularly and its time scale is short. Detailed *in-situ* measurement of calving and the propagation of crevasses and rifts can be used to validate and calibrate the current calving model so that we can make better future projections. Similarly to calving, ocean observations under ice shelves or near ice fronts are also rare. The dynamical changes of both the AIS and the Greenland Ice Sheet (GIS) have an important ocean origin. Therefore, the ocean condition is the most important factor to the future change of these two ice sheets. A long record of ocean observations would provide insight to ice shelf melt rate and ice front melt rate estimation.

Due to extreme weather conditions in the polar region, the observation of calving and ocean is both difficult and dangerous. Despite this, some recent field campaigns have already made access. For instance, the observation of calving through a GPS network or a Gamma

Portable Radar Interferometer (GPRI) and the observation of ocean conditions using CTDs (*Murray et al.*, 2015; *Jacobs et al.*, 2012)

In our modeling study on the crevasse propagation of TG, the linear elastic fracture mechanics (LEFM) approach has some limitations in simulating crevasse propagation. First, the LEFM theory does not explain the propagation of a crevasse from 1 mm to 1 m scale (*Weiss*, 2004). Therefore, we made the assumption that a crevasse can propagate as long as its minimum required depth is smaller than 1 m. The initiation of crevasses could be improved using a subcritical crevasse propagation method or damage mechanics (*Weiss*, 2004; *Krug et al.*, 2014), but this is beyond the scope of our study. Another issue is associated with the width of crevasses, which should be $\sim$1 cm according to LEFM (*Lister*, 1990; *Bassis and Ma*, 2015). Modeling a crevasse at this scale is computationally too demanding. Once a crevasse is formed, however, its shape is controlled by the viscous flow of ice, which reduces its depth and increases its width. In our experiments, crevasses are able to grow quickly from 20 m width to 60-70 m in 0.01 yr when deforming under viscous flow. This viscous widening process is not sensitive to the width itself like elastic widening. Experiments with an initial width of 10 m and 40 m are conducted and the crevasses width are similar at the end of these experiments. We therefore deem it reasonable to assume that the crevasses grow to a width of 20 m if LEFM shows that the infinitesimal crevasse can propagate.

Despite these limitations, we show that the combination of a FS ice flow model with a LEFM model can be used to study calving dynamics. This framework can be readily applied to other glaciers, including tidewater glaciers. For tidewater glaciers, basal crevasses are hard to form since the ice is grounded and calving is controlled by the penetration of surface crevasses, which is determined by the initial crevasse depth, surface stress field and the possible existence of water in the crevasses. The model can then be applied to glaciers that have direct calving observations to reproduce past calving events and make future projections.

In our ice shelf melting experiments, there are also two major limitations. The first one is our ice shelf melt rate parameterization. The actual ice shelf melt rate is determined by ocean temperature, salinity, ocean circulation, bathymetry and many other factors. Its pattern would be much more complicated than a linear relationship with depth. Therefore, it would be preferable to apply ice shelf melt rate calculated using a coupled ice-ocean model, i.e. with a time-dependent cavity (*Seroussi et al.*, 2017; *Cornford et al.*, 2015). Coupled models indicate that warm ocean water has more limited access to newly formed cavities as ice retreats (*De Rydt and Gudmundsson*, 2016; *Seroussi et al.*, 2017). This lower efficiency of ice shelf melt will lower the contribution of TG to sea level rise in the 21st century. In the case of TG, oceanic warming is the main cause of its retreat while atmospheric warming has limited impact. In other glaciers, or in a climate warming scenario, atmospheric warming would be another import trigger of dynamical changes. A fully coupled ice-global climate model is needed to produce the most realistic sea level projection. However, such a coupled model would require enormous computing power.

The second limitation is that ice front migration is not included in our simulations. We assume that the ice front position of TG remains fixed so that all ice passing the present day ice front immediately calves. Densely distributed crevasses along the ice shelf of TG, however, make the ice shelf conducive to rapid calving (*Yu et al.*, 2017). Once the ice shelf is removed, the grounding line will retreat into deeper regions, and the probability of calving increases according to the marine ice-cliff instability theory (*Pollard et al.*, 2015; *Wise et al.*, 2017). Crevassing and calving will therefore reduce ice shelf buttressing drastically and accelerate ice flow further, which means that our simulations underestimate the potential mass loss of TG (*MacGregor et al.*, 2012). On Pine Island Glacier, calving has increased in frequency and its ice front is now 35 km farther inland on the eastern side than in the 1940's (*MacGregor et al.*, 2012; *Jeong et al.*, 2016). On TG, the floating ice tongue in the center trunk has retreated by 26 km from 1973 to 2009 (*MacGregor et al.*, 2012). The eastern ice

shelf has been thinning and retreating, which means that the ice shelf may disintegrate in the coming decades.

In this study, we found that the different choice of numerical implementation of the model could significantly change model results. However, in the case of TG, the results start to diverge only after 30 years. Thus, with the current observation record, it is hard to find which model configuration best captures the behavior of TG. For different glaciers, the best model configurations could also be different. Therefore, a consistent longer record of glacier changes over the AIS and GIS is needed to better calibrate ice sheet models and to make better projections.

Bibliography

Anderson, T. L. (2005), *Fracture Mechanics: Fundamentals and Applications, Third Edition*, CRC Press, Taylor & Francis Group, 6000 Broken Sound Parkway NW, Suite 300, Boca Raton, FL, USA.

Arthern, R. J., and C. R. Williams (2017), The sensitivity of West Antarctica to the submarine melting feedback, *Geophys. Res. Lett.*, *44*(5), 2352–2359, doi:10.1002/2017GL072514.

Barrett, P. J. (2009), *Cenozoic Climate and Sea Level History from Glacimarine Strata off the Victoria Land Coast, Cape Roberts Project, Antarctica*, pp. 259–287, Blackwell Publishing Ltd., doi:10.1002/9781444304435.ch15.

Bassis, J. N., and Y. Ma (2015), Evolution of basal crevasses links ice shelf stability to ocean forcing, *Earth and Planetary Science Letters*, *409*, 203–211, doi:10.1016/j.epsl.2014.11.003.

Bassis, J. N., and C. C. Walker (2012), Upper and lower limits on the stability of calving glaciers from the yield strength envelope of ice, *Proceedings of the Royal Society A: Mathematical, Physical and Engineering Sciences*, *468*(2140), 913–931, doi:10.1098/rspa.2011.0422.

Benn, D. I., C. R. Warren, and R. H. Mottram (2007), Calving processes and the dynamics of calving glaciers, *Earth Sci. Rev.*, *82*(3-4), 143–179, doi:10.1016/j.earscirev.2007.02.002.

Berthier, E., T. A. Scambos, and C. A. Shuman (2012), Mass loss of Larsen B tributary glaciers (Antarctic Peninsula) unabated since 2002, *Geophysical Research Letters*, *39*(13), 1–6, doi:10.1029/2012GL051755.

Blatter, H. (1995), Velocity And Stress-Fields In Grounded Glaciers: A Simple Algorithm For Including Deviatoric Stress Gradients, *J. Glaciol.*, *41*(138), 333–344.

Blatter, H., G. Greve, and A. Abe-ouchi (2010), A short history of the thermomechanical theory and modelling of glaciers and ice sheets, *Ann. of Glaciol.*, *56 (200)*, 187–194.

Bracegirdle, T. J., W. M. Connolley, and J. Turner (2008), Antarctic climate change over the twenty first century, *Journal of Geophysical Research Atmospheres*, *113*(3), 1–13, doi:10.1029/2007JD008933.

Brondex, J., O. Gagliardini, F. Gillet-Chaulet, and G. Durand (2017), Sensitivity of grounding line dynamics to the choice of the friction law, *J. Glaciol.*, *63*(241), 854–866, doi:10.1017/jog.2017.51.

Budd, W. F., P. L. Keage, and N. A. Blundy (1979), Empirical studies of ice sliding, *J. Glaciol.*, *23*, 157–170.

Cook, A. J., A. J. Fox, D. G. Vaughan, and J. G. Ferrigno (2005), Retreating glacier fronts on the Antarctic Peninsula over the past half-century, *Science*, *308*(5721), 541–544, doi: 10.1126/science.1104235.

Cook, S., I. C. Rutt, T. Murray, a. Luckman, T. Zwinger, N. Selmes, a. Goldsack, and T. D. James (2014), Modelling environmental influences on calving at Helheim Glacier in eastern Greenland, *Cryosphere*, *8*(3), 827–841, doi:10.5194/tc-8-827-2014.

Cornford, S. L., D. F. Martin, D. T. Graves, D. F. Ranken, A. M. Le Brocq, R. M. Gladstone, A. J. Payne, E. G. Ng, and W. H. Lipscomb (2013), Adaptive mesh, finite volume modeling of marine ice sheets, *J. Comput. Phys.*, *232*(1), 529–549, doi:10.1016/j.jcp.2012.08.037.

Cornford, S. L., D. F. Martin, A. J. Payne, E. G. Ng, A. M. Le Brocq, R. M. Gladstone, T. L. Edwards, S. R. Shannon, C. Agosta, M. R. Van Den Broeke, H. H. Hellmer, G. Krinner, S. R. M. Ligtenberg, R. Timmermann, and D. G. Vaughan (2015), Century-scale simulations of the response of the West Antarctic Ice Sheet to a warming climate, *The Cryosphere*, *9*(4), 1579–1600, doi:10.5194/tc-9-1579-2015.

Cuffey, K. M., and W. S. B. Paterson (2010), *The Physics of Glaciers, 4th Edition*, Elsevier, Oxford.

De Rydt, J., and G. H. Gudmundsson (2016), Coupled ice shelfocean modeling and complex grounding line retreat from a seabed ridge, *J. Geophys. Res. Earth Surf.*, *121*(5), 865–880, doi:10.1002/2015JF003791.

Deconto, R. M., and D. Pollard (2016), Contribution of Antarctica to past and future sea-level rise, *Nature*, *531*(7596), 591–597, doi:10.1038/nature17145.

Depoorter, M. a., J. L. Bamber, J. a. Griggs, J. T. M. Lenaerts, S. R. M. Ligtenberg, M. R. van den Broeke, and G. Moholdt (2013), Calving fluxes and basal melt rates of Antarctic ice shelves., *Nature*, *502*(7469), 89–92, doi:10.1038/nature12567.

Duddu, R., J. N. Bassis, and H. Waisman (2013), A numerical investigation of surface crevasse propagation in glaciers using nonlocal continuum damage mechanics, *Geophys. Res. Lett.*, *40*, doi:10.1002/grl.50602.

Dupont, T. K., and R. B. Alley (2005), Assessment of the importance of ice-shelf buttressing to ice-sheet flow, *Geophys. Res. Lett.*, *32*(4), 1–4, doi:10.1029/2004GL022024.

Durand, G., O. Gagliardini, B. de Fleurian, T. Zwinger, and E. Le Meur (2009a), Marine ice sheet dynamics: Hysteresis and neutral equilibrium, *J. Geophys. Res.*, *114*(F3), 1–10, doi:10.1029/2008JF001170.

Durand, G., O. Gagliardini, T. Zwinger, E. Le Meur, and R. C. A. Hindmarsh (2009b), Full Stokes modeling of marine ice sheets: influence of the grid size, *Ann. Glaciol.*, *50*(52), 109–114.

Dutrieux, P., J. De Rydt, A. Jenkins, P. R. Holland, H. K. Ha, S. H. Lee, E. J. Steig, Q. Ding, E. P. Abrahamsen, and M. Schröder (2014), Strong sensitivity of Pine Island ice-shelf melting to climatic variability., *Science*, *343*(6167), 174–8, doi:10.1126/science.1244341.

Dutton, A., and K. Lambeck (2012), Ice Volume and Sea Level During the Last Interglacial, *Science*, *337*(6091), 216–219, doi:10.1126/science.1205749.

Favier, L., O. Gagliardini, G. Durand, and T. Zwinger (2012), A three-dimensional full Stokes model of the grounding line dynamics: effect of a pinning point beneath the ice shelf, *The Cryosphere*, *6*, 101–112, doi:10.5194/tc-6-101-2012.

Favier, L., G. Durand, S. L. Cornford, G. H. Gudmundsson, O. Gagliardini, F. Gillet-Chaulet, T. Zwinger, a. J. Payne, and a. M. Le Brocq (2014), Retreat of Pine Island Glacier controlled by marine ice-sheet instability, *Nat. Clim. Change*, *4*(2), 1–5, doi:DOI:10.1038/NCLIMATE2094.

Feldmann, J., and A. Levermann (2015), Collapse of the west antarctic ice sheet after local destabilization of the amundsen basin, *Proc. Natl. Acad. Sci. USA*, *112*(46), 14,191–14,196, doi:10.1073/pnas.1512482112.

Fischer, M. P., R. B. Alley, and T. Engelder (1995), Fracture toughness of ice and firn determined from the modified ring test, *Journal of Glaciology*, *41*, 383–394.

Flower, B. P., and J. P. Kennett (1994), The middle Miocene climatic transition - East Antarctic ice-sheet development, deep-ocean circulation and global carbon cycling, *Palaeogeography Palaeoclimatology Palaeoecology*, *108*(3-4), 537–555, doi:10.1016/0031-0182(94)90251-8.

Fretwell, P., H. D. Pritchard, D. G. Vaughan, J. L. Bamber, N. E. Barrand, R. Bell, C. Bianchi, R. G. Bingham, D. D. Blankenship, G. Casassa, G. Catania, D. Callens, H. Conway, a. J. Cook, H. F. J. Corr, D. Damaske, V. Damm, F. Ferraccioli, R. Forsberg, S. Fujita, Y. Gim, P. Gogineni, J. a. Griggs, R. C. a. Hindmarsh, P. Holmlund, J. W. Holt, R. W. Jacobel, A. Jenkins, W. Jokat, T. Jordan, E. C. King, J. Kohler, W. Krabill, M. Riger-Kusk, K. a. Langley, G. Leitchenkov, C. Leuschen, B. P. Luyendyk, K. Matsuoka, J. Mouginot, F. O. Nitsche, Y. Nogi, O. a. Nost, S. V. Popov, E. Rignot, D. M. Rippin, A. Rivera, J. Roberts, N. Ross, M. J. Siegert, a. M. Smith, D. Steinhage, M. Studinger, B. Sun, B. K. Tinto, B. C. Welch, D. Wilson, D. a. Young, C. Xiangbin, and A. Zirizzotti (2013), Bedmap2: improved ice bed, surface and thickness datasets for Antarctica, *The Cryosphere*, *7*(1), 375–393.

Fricker, H. A., T. Scambos, R. Bindschadler, and L. Padman (2007), An active subglacial water system in West Antarctica mapped from space, *Science*, *315*(5818), 1544–1548, doi:10.1126/science.1136897.

Gagliardini, O., D. Cohen, P. Raback, and T. Zwinger (2007), Finite-element modeling of subglacial cavities and related friction law, *J. Geophys. Res. - Earth Surface*, *112*(F2), 1–11, doi:10.1029/2006JF000576.

Gagliardini, O., G. Durand, T. Zwinger, R. C. a. Hindmarsh, and E. Le Meur (2010), Coupling of ice-shelf melting and buttressing is a key process in ice-sheets dynamics, *Geophys. Res. Lett.*, *37*(L14501), 1–5, doi:10.1029/2010GL043334.

Glen, J. W. (1952), Experiments on the Deformation of Ice, *Journal of Glaciology*, *2*(12), 111–114, doi:10.1017/S0022143000034067.

Glen, J. W. (1955), The creep of polycrystalline ice, *Proc. R. Soc. A*, *228*(1175), 519–538.

Gogineni, P. (2012), CReSIS Radar Depth Sounder Data.

Goldberg, D., D. M. Holland, and C. Schoof (2009), Grounding line movement and ice shelf buttressing in marine ice sheets, *J. Geophys. Res.*, *114*(F04026), 1–23, doi:10.1029/2008JF001227.

Goldberg, D. N., P. Heimbach, I. Joughin, and B. Smith (2015), Committed retreat of smith, pope, and kohler glaciers over the next 30 years inferred by transient model calibration, *The Cryosphere*, *9*(6), 2429–2446, doi:10.5194/tc-9-2429-2015.

Golledge, N. R., D. E. Kowalewski, T. R. Naish, R. H. Levy, C. J. Fogwill, and E. G. Gasson (2015), The multi-millennial Antarctic commitment to future sea-level rise, *Nature*, *526*(7573), 421–425, doi:10.1038/nature15706.

Gray, L., I. Joughin, S. Tulaczyk, V. B. Spikes, R. Bindschadler, and K. Jezek (2005), Evidence for subglacial water transport in the West Antarctic Ice Sheet through three-dimensional satellite radar interferometry, *Geophys. Res. Lett.*, *32*(3), 1–4, doi:10.1029/2004GL021387.

Gudmundsson, G. H., J. Krug, G. Durand, L. Favier, and O. Gagliardini (2012), The stability of grounding lines on retrograde slopes, *The Cryosphere*, *6*(6), 1497–1505, doi:10.5194/tc-6-1497-2012.

Holland, D. M., and A. Jenkins (1999), Modeling thermodynamic ice-ocean interactions at the base of an ice shelf, *J. Phys. Oceanogr.*, *29*(8, Part 1), 1787–1800.

Holt, J. W., D. D. Blankenship, D. L. Morse, D. A. Young, M. E. Peters, S. D. Kempf, T. G. Richter, D. G. Vaughan, and H. F. J. Corr (2006), New boundary conditions for the West Antarctic Ice Sheet: Subglacial topography of the Thwaites and Smith glacier catchments, *Geophys. Res. Lett.*, *33*(9), 1–4, doi:10.1029/2005GL025561.

Hooke, R. L. (2005), *Principles of Glacier Mechanics*, 2nd ed., 763 pp., Cambridge.

Hughes, T. (1981), The weak underbelly of the West Antarctic ice-Sheet, *J. Glaciol.*, *27*(97), 518–525.

Hulbe, C. L., and D. R. MacAyeal (1999), A new numerical model of coupled inland ice sheet, ice stream, and ice shelf flow and its application to the West Antarctic Ice Sheet, *J. Geophys. Res.*, *104*(B11), 25,349–25,366.

Humbert, A., and D. Steinhage (2011), The evolution of the western rift area of the Fimbul Ice Shelf, Antarctica, *The Cryosphere*, *5*(4), 931–944, doi:10.5194/tc-5-931-2011.

Hutter, K. (1983), *Theoretical glaciology: material science of ice and the mechanics of glaciers and ice sheets*, 150 pp., D. Reidel Publishing Co, Dordrecht, The Netherlands.

Huybrechts, P., J. Gregory, I. Janssens, and M. Wild (2004), Modelling Antarctic and Greenland volume changes during the 20th and 21st centuries forced by GCM time slice integrations, *Glob. Planet. Change*, *42*(1-4), 83–105, doi:10.1016/j.gloplacha.2003.11.011.

Jacobs, S., A. Jenkins, H. Hellmer, C. Giulivi, F. Nitsche, B. Huber, and R. Guerrero (2012), The Amundsen Sea and the Antarctic Ice Sheet, *Oceanography*, *25*(3, SI), 154–163, doi:10.5670/oceanog.2012.90.

Jacobs, S. S., A. Jenkins, C. F. Giulivi, and P. Dutrieux (2011), Stronger ocean circulation and increased melting under Pine Island Glacier ice shelf, *Nature Geosci.*, *4*(8), 519–523, doi:10.1038/NGEO1188.

Jenssen, D. (1977), A three-dimensional polar ice sheet model, *J. Glaciol.*, *18*, 373–389.

Jeong, S., I. M. Howat, and J. N. Bassis (2016), Accelerated ice shelf rifting and retreat at Pine Island Glacier, West Antarctica, *Geophys. Res. Lett.*, *43*(22), 11,720–11,725, doi:10.1002/2016GL071360.

Joughin, I., B. E. Smith, I. M. Howat, T. Scambos, and T. Moon (2010), Greenland flow variability from ice-sheet-wide velocity mapping, *J. Glaciol.*, *56*, 416–430.

Joughin, I., B. E. Smith, and B. Medley (2014), Marine ice sheet collapse potentially under way for the Thwaites Glacier Basin, West Antarctica., *Science*, *344*(6185), 735–8, doi:10.1126/science.1249055.

Kennett, J. P., and D. a. Hodell (1993), Evidence for relative climatic stability of Antarctica during the early Pliocene: a marine perspective, *Geografiska Annaler, Series A*, *75 A*(4), 205–220, doi:10.2307/521201.

Kopp, R. E., F. J. Simons, J. X. Mitrovica, A. C. Maloof, and M. Oppenheimer (2009), Probabilistic assessment of sea level during the last interglacial stage, *Nature*, *462*(7275), 863–867, doi:10.1038/nature08686.

Krabill, W. (2014), Icebridge atm l2 icessn elevation, slope, and roughness, version 2.

Krinner, G., O. Magand, I. Simmonds, C. Genthon, and J. L. Dufresne (2007), Simulated Antarctic precipitation and surface mass balance at the end of the twentieth and twenty-first centuries, *Climate Dynamics*, *28*(2-3), 215–230, doi:10.1007/s00382-006-0177-x.

Krug, J., J. Weiss, O. Gagliardini, and G. Durand (2014), Combining damage and fracture mechanics to model calving, *The Cryosphere*, *8*(6), 2101–2117, doi:10.5194/tc-8-2101-2014.

Krug, J., G. Durand, O. Gagliardini, and J. Weiss (2015), Modelling the impact of submarine frontal melting and ice mélange on glacier dynamics, *The Cryosphere Discussions*, *9*(1), 183–221, doi:10.5194/tcd-9-183-2015.

Larour, E., E. Rignot, and D. Aubry (2004a), Processes involved in the propagation of rifts near Hemmen Ice Rise, Ronne Ice Shelf, Antarctica, *J. Glaciol.*, *50*(170), 329–341.

Larour, E., E. Rignot, and D. Aubry (2004b), Modelling of rift propagation on Ronne Ice Shelf, Antarctica, and sensitivity to climate change, *Geophys. Res. Lett.*, *31*(L16404), 1–4, doi:10.1029/2004GL020077.

Larour, E., H. Seroussi, M. Morlighem, and E. Rignot (2012), Continental scale, high order, high spatial resolution, ice sheet modeling using the Ice Sheet System Model (ISSM), *J. Geophys. Res.*, *117*(F01022), 1–20, doi:10.1029/2011JF002140.

Le Brocq, A. M., N. Ross, J. A. Griggs, R. G. Bingham, H. F. J. Corr, F. Ferraccioli, A. Jenkins, T. A. Jordan, A. J. Payne, D. M. Rippin, and M. J. Siegert (2013), Evidence from ice shelves for channelized meltwater flow beneath the Antarctic Ice Sheet, *Nature Geoscience*, *6*(11), 945–948, doi:10.1038/ngeo1977.

Lenaerts, J. T. M., and M. R. van den Broeke (2012), Modeling drifting snow in Antarctica with a regional climate model: 2. Results, *J. Geophys. Res.*, *117*(D5), D05,109, doi:10.1029/2010JD015419.

Lenaerts, J. T. M., M. R. van den Broeke, W. J. van de Berg, E. van Meijgaard, P. Kuipers Munneke, and P. K. Munneke (2012), A new, high-resolution surface mass balance map of Antarctica (1979-2010) based on regional atmospheric climate modeling, *Geophys. Res. Lett.*, *39*(4), 1–5, doi:10.1029/2011GL050713.

Li, X., D. M. Holland, E. P. Gerber, and C. Yoo (2015), Rossby waves mediate impacts of tropical oceans on west Antarctic atmospheric circulation in austral winter, *Journal of Climate*, *28*(20), 8151–8164, doi:10.1175/JCLI-D-15-0113.1.

Li, X., E. Rignot, J. Mouginot, and B. Scheuchl (2016), Ice flow dynamics and mass loss of Totten Glacier, East Antarctica, from 1989 to 2015, *Geophysical Research Letters*, *43*(12), 6366–6373, doi:10.1002/2016GL069173.

Lister, J. R. (1990), Buoyancy-driven fluid fracture : similarity solutions for the horizontal and vertical propagation of fluid-filled cracks, *Journal of Fluid Mechanics*, *217*, 213–239.

Liu, Y., J. C. Moore, X. Cheng, R. M. Gladstone, J. N. Bassis, H. Liu, J. Wen, and F. Hui (2015), Ocean-driven thinning enhances iceberg calving and retreat of Antarctic ice shelves, *Proceedings of the National Academy of Sciences*, *112*(11), 3263–3268, doi:10.1073/pnas.1415137112.

Ma, Y., C. S. Tripathy, and J. N. Bassis (2017), Bounds on the calving cliff height of marine terminating glaciers, *Geophysical Research Letters*, *44*, 1–7, doi:10.1002/2016GL071560.

MacAyeal, D. R. (1989), Large-scale ice flow over a viscous basal sediment: Theory and application to Ice Stream B, Antarctica, *J. Geophys. Res.*, *94*(B4), 4071–4087.

MacAyeal, D. R. (1992), The basal stress distribution of Ice Stream E, Antarctica, inferred by control methods, *Journal of Geophysical Research*, *97*(B1), 595.

MacAyeal, D. R. (1993), Binge/Purge oscillations of the Laurentide ice-sheet as a cause of the North-Atlantic's Heinrich events, *Paleoceanography*, *8*(6), 775–784.

MacGregor, J. A., G. A. Catania, M. S. Markowski, and A. G. Andrews (2012), Widespread rifting and retreat of ice-shelf margins in the eastern Amundsen Sea Embayment between 1972 and 2011, *J. Glaciol.*, *58*(209), 458–466.

Mahaffy, M. W. (1976), 3-dimensional Numerical Model of Ice Sheets - Tests on the Barnes Ice Cap, Northwest Territories, *J. Geophys. Res.*, *81*(6), 1059–1066, doi:10.1029/JC081i006p01059.

Maule, C. F., M. E. Purucker, N. Olsen, and K. Mosegaard (2005), Heat Flux Anomalies in Antarctica Revealed by Satellite Magnetic Data, *Science*, *309*(5733), 464–467.

Mayewski, P. A., M. P. Meredith, C. P. Summerhayes, J. Turner, A. Worby, P. J. Barrett, G. Casassa, N. A. N. Bertler, T. Bracegirdle, A. C. N. Garabato, D. Bromwich, H. Campbell, G. S. Hamilton, W. B. Lyons, K. A. Maasch, S. Aoki, C. Xiao, and T. van Ommen (2009), State of the Antarctic and Southern Ocean Climate System, *Rev. Geophys.*, *47*, 38, doi:10.1029/2007RG000231.

Medley, B., I. Joughin, B. E. Smith, S. B. Das, E. J. Steig, H. Conway, S. Gogineni, C. Lewis, A. S. Criscitiello, J. R. McConnell, M. R. van den Broeke, J. T. M. Lenaerts, D. H. Bromwich, J. P. Nicolas, and C. Leuschen (2014), Constraining the recent mass balance of pine island and thwaites glaciers, west antarctica, with airborne observations of snow accumulation, *The Cryosphere*, *8*(4), 1375–1392, doi:10.5194/tc-8-1375-2014.

Millan, R., E. Rignot, V. Bernier, M. Morlighem, and P. Dutrieux (2017), Bathymetry of the Amundsen Sea Embayment sector of West Antarctica from Operation IceBridge gravity and other data, *Geophys. Res. Lett.*, *44*(3), 1360–1368, doi:10.1002/2016GL072071.

Morland, L. W. (1984), Thermomechanical balances of ice-sheet flows, *Geophys. Astrophys. Fluid Dynamics*, *29*(3), 237–266.

Morland, L. W. (1987), Unconfined ice shelf flow, *Proceedings of Workshop on the Dynamics of the West Antarctic Ice Sheet, University of Utrecht, May 1985. Published by Reidel, ed. C.J. v*, 99–116.

Morlighem, M. (2011), Ice sheet properties inferred by combining numerical modeling and remote sensing data, Ph.D. thesis, Ecole Centrale Paris.

Morlighem, M., E. Rignot, H. Seroussi, E. Larour, H. Ben Dhia, and D. Aubry (2010), Spatial patterns of basal drag inferred using control methods from a full-Stokes and simpler models for Pine Island Glacier, West Antarctica, *Geophys. Res. Lett.*, *37*(14), L14,502.

Morlighem, M., E. Rignot, H. Seroussi, E. Larour, H. Ben Dhia, and D. Aubry (2011), A mass conservation approach for mapping glacier ice thickness, *Geophys. Res. Lett.*, *38*(L19503), 1–6, doi:10.1029/2011GL048659.

Morlighem, M., H. Seroussi, E. Larour, and E. Rignot (2013), Inversion of basal friction in Antarctica using exact and incomplete adjoints of a higher-order model, *J. Geophys. Res.*, *118*(3), 1746–1753, doi:10.1002/jgrf.20125.

Mouginot, J., E. Rignot, and B. Scheuchl (2014), Sustained increase in ice discharge from the Amundsen Sea Embayment, West Antarctica, from 1973 to 2013, *Geophys. Res. Lett.*, *41*, 1–9, doi:10.1002/2013GL059069.

Murray, T., M. Nettles, N. Selmes, L. M. Cathles, J. C. Burton, T. D. James, S. Edwards, I. Martin, T. O'Farrell, R. Aspey, I. Rutt, and T. Baugé (2015), Reverse glacier motion during iceberg calving and the cause of glacial earthquakes, *Science*, *349*(6245), 305–308, doi:10.1126/science.aab0460.

Naish, T., K. Woolfe, P. Barrett, G. Wilson, C. Atkins, S. Bohaty, C. Bücker, M. Claps, F. Davey, G. Dunbar, A. Dunn, C. Fielding, F. Florindo, M. Hannah, D. Harwood, S. Henrys, L. Krissek, M. Lavelle, J. van Der Meer, W. McIntosh, F. Niessen, S. Passchier, R. Powell, A. Roberts, L. Sagnotti, R. Scherer, C. Strong, F. Talarico, K. Verosub, G. Villa, D. Watkins, P. Webb, and T. Wonik (2001), Orbitally induced oscillations in the East Antarctic ice sheet at the Oligocene/Miocene boundary., *Nature*, *413*(6857), 719–23, doi:10.1038/35099534.

Nick, F. M., A. Vieli, M. L. Andersen, I. Joughin, A. Payne, T. L. Edwards, F. Pattyn, and R. S. W. van de Wal (2013), Future sea-level rise from Greenland's main outlet glaciers in a warming climate, *Nature*, *497*(7448), 235–238.

Nowicki, S. M. J., and D. J. Wingham (2008), Conditions for a steady ice sheet–ice shelf junction, *Earth Planet. Sci. Lett.*, *265*(1-2), 246–255, doi:10.1016/j.epsl.2007.10.018.

Nye, J. F. (1953), The flow law of ice from measurements in glacier tunnels, laboratory experiments and the Jungfraufirn borehole experiment, *Proc. R. Soc. A*, *219*(1193), 477–489.

Nye, J. F. (1957a), *Physical properties of crystals: Their representation by tensor and matrices*, first ed., Oxford University Press.

Nye, J. F. (1957b), The distribution of stress and velocity in glaciers and ice-sheets, *Proc. R. Soc. A*, *239*(1216), 113–133.

O'Leary, M., and P. Christoffersen (2013), Calving on tidewater glaciers amplified by submarine frontal melting, *Cryosphere*, *7*(1), 119–128, doi:10.5194/tc-7-119-2013.

Parizek, B. R., K. Christianson, S. Anandakrishnan, R. B. Alley, R. T. Walker, R. a. Edwards, D. S. Wolfe, G. T. Bertini, S. K. Rinehart, R. a. Bindschadler, and S. M. J. Nowicki (2013), Dynamic (in)stability of Thwaites Glacier, West Antarctica, *J. Geophys. Res.*, *118*, 1–18, doi:10.1002/jgrf.20044.

Pattyn, F. (2003), A new three-dimensional higher-order thermomechanical ice sheet model: Basic sensitivity, ice stream development, and ice flow across subglacial lakes, *J. Geophys. Res.*, *108*(B8), 1–15, doi:10.1029/2002JB002329.

Pattyn, F., C. Schoof, L. Perichon, R. C. a. Hindmarsh, E. Bueler, B. de Fleurian, G. Durand, O. Gagliardini, R. Gladstone, D. Goldberg, G. H. Gudmundsson, P. Huybrechts, V. Lee, F. M. Nick, a. J. Payne, D. Pollard, O. Rybak, F. Saito, and A. Vieli (2012), Results of the Marine Ice Sheet Model Intercomparison Project, MISMIP, *The Cryosphere*, *6*(3), 573–588, doi:10.5194/tc-6-573-2012.

Pattyn, F., L. Perichon, G. Durand, L. Favier, O. Gagliardini, R. C. A. Hindmarsh, T. Zwinger, T. Albrecht, S. Cornford, D. Docquier, J. Fuerst, D. Goldberg, H. Gudmundsson, A. Humbert, M. Hutten, P. Huybrecht, G. Jouvet, T. Kleiner, E. Larour, D. Martin, M. Morlighem, A. J. Payne, D. Pollard, M. Ruckamp, O. Rybak, H. Seroussi, M. Thoma, N. Wilkens, J. J. Fu, G. H. Gudmundsson, P. Huybrechts, and M. Ru (2013), Grounding-line migration in plan-view marine ice-sheet models: results of the ice2sea MISMIP3d intercomparison, *J. Glaciol.*, *59 (215)*(215), 410–422, doi:10.3189/2013JoG12J129.

Plate, C., R. Müller, A. Humbert, and D. Gross (2012), Evaluation of the criticality of cracks in ice shelves using finite element simulations, *The Cryosphere*, *6*(5), 973–984, doi:10.5194/tc-6-973-2012.

Pollard, D., R. M. Deconto, and R. B. Alley (2015), Potential Antarctic Ice Sheet retreat driven by hydrofracturing and ice cliff failure, *Earth Planet. Sci. Lett.*, *412*, 112–121, doi:10.1016/j.epsl.2014.12.035.

Pritchard, H. D., R. J. Arthern, D. G. Vaughan, and L. A. Edwards (2009), Extensive dynamic thinning on the margins of the Greenland and Antarctic ice sheets, *Nature*, *461*, 971–975, doi:10.1038/nature08471.

Reist, A. (2005), Mathematical analysis and numerical simulation of the motion of a glacier, Ph.D. thesis, Ecole Polytechnique Fédérale de Lausanne.

Rignot, E. (2001), Evidence for rapid retreat and mass loss of Thwaites Glacier, West Antarctica, *J. Glaciol.*, *47*(157), 213–222, doi:10.3189/172756501781832340.

Rignot, E. (2006), Changes in ice dynamics and mass balance of the Antarctic ice sheet, *Phil. Trans R. Soc. A*, *364*(1844), 1637–1655, doi:10.1098/rsta.2006.1793.

Rignot, E. (2008a), Changes in West Antarctic ice stream dynamics observed with ALOS PALSAR data, *Geophys. Res. Lett.*, *35*(12), 1–5, doi:10.1029/2008GL033365.

Rignot, E. (2008b), PALSAR studies of ice sheet motion in Antarctica, in *ALOS PI Symposium, Nov. 3-7 2008*.

Rignot, E., J. L. Bamber, M. R. van den Broeke, C. Davis, Y. Li, W. J. van de Berg, and E. van Meijgaard (2008), Recent Antarctic ice mass loss from radar interferometry and regional climate modelling, *Nature Geoscience*, *1*(2), 106–110.

Rignot, E., M. Koppes, and I. Velicogna (2010), Rapid submarine melting of the calving faces of West Greenland glaciers, *Nat. Geosci.*, *3*(3), 187–191, doi:10.1038/NGEO765.

Rignot, E., J. Mouginot, and B. Scheuchl (2011a), Ice Flow of the Antarctic Ice Sheet, *Science*, *333*(6048), 1427–1430, doi:10.1126/science.1208336.

Rignot, E., J. Mouginot, and B. Scheuchl (2011b), Antarctic grounding line mapping from differential satellite radar interferometry, *Geophys. Res. Lett.*, *38*(10), doi:10.1029/2011GL047109.

Rignot, E., I. Velicogna, M. R. van den Broeke, A. Monaghan, and J. T. M. Lenaerts (2011c), Acceleration of the contribution of the Greenland and Antarctic ice sheets to sea level rise, *Geophys. Res. Lett.*, *38*(5), 1–5, doi:10.1029/2011GL046583.

Rignot, E., S. Jacobs, J. Mouginot, and B. Scheuchl (2013), Ice shelf melting around Antarctica, *Science*, *341*(6143), 266–270, doi:10.1126/science.1235798.

Rignot, E., J. Mouginot, M. Morlighem, H. Seroussi, and B. Scheuchl (2014), Widespread, rapid grounding line retreat of pine island, thwaites, smith, and kohler glaciers, west antarctica, from 1992 to 2011, *Geophys. Res. Lett.*, *41*(10), 3502–3509, doi:10.1002/2014GL060140.

Rist, M., P. Sammonds, S. Murrell, P. Meredith, H. Oerter, and C. Doake (1996), Experimental fracture and mechanical properties of Antarctic ice: preliminary results, *Annals of Glaciology*, *23*, 284–292.

Rist, M. A., P. R. Sammonds, H. Oerter, and C. S. M. Doake (2002), Fracture of Antarctic shelf ice, *J. Geophys. Res.*, *107*(B1), 1–13, doi:10.1029/2000JB000058.

Ritz, C., A. Fabre, and A. Letreguilly (1997), Sensitivity of a Greenland ice sheet model to ice flow and ablation parameters: Consequences for the evolution through the last climatic cycle, *Clim. Dyn.*, *13*(1), 11–24.

Rott, H., F. Mueller, T. Nagler, and D. Floricioiu (2011), The imbalance of glaciers after disintegration of Larsen-B ice shelf, Antarctic Peninsula, *The Cryosphere*, *5*(1), 125–134, doi:10.5194/tc-5-125-2011.

Scambos, T. A., R. E. Bell, R. B. Alley, S. Anandakrishnan, D. H. Bromwich, K. Brunt, K. Christianson, T. Creyts, S. B. Das, R. DeConto, P. Dutrieux, H. A. Fricker, D. Holland, J. MacGregor, B. Medley, J. P. Nicolas, D. Pollard, M. R. Siegfried, A. M. Smith, E. J. Steig, L. D. Trusel, D. G. Vaughan, and P. L. Yager (2017), How much, how fast?: A science review and outlook for research on the instability of Antarctica's Thwaites Glacier in the 21st century, *Global and Planetary Change*, *153*(April), 16–34, doi:10.1016/j.gloplacha.2017.04.008.

Schodlok, M. P., D. Menemenlis, E. Rignot, and M. Studinger (2012), Sensitivity of the ice-shelf/ocean system to the sub-ice-shelf cavity shape measured by NASA IceBridge in Pine Island Glacier, West Antarctica, *Ann. Glaciol.*, *53(60)*, 156–162, doi:10.3189/2012AoG60A073.

Schoof, C. (2006), A variational approach to ice stream flow, *J. Fluid Mech.*, *556*, 227–251, doi:10.1017/S0022112006009591.

Schoof, C. (2007), Ice sheet grounding line dynamics: Steady states, stability, and hysteresis, *J. Geophys. Res.*, *112*(F03S28), 1–19, doi:10.1029/2006JF000664.

Seroussi, H., and S. Price (2014), Modeling of Greenland ice sheet and ocean interactions: progress and challenges, *US CLIVAR Variations Newsletters*.

Seroussi, H., M. Morlighem, E. Rignot, E. Larour, D. Aubry, H. Ben Dhia, and S. S. Kristensen (2011), Ice flux divergence anomalies on 79north Glacier, Greenland, *Geophys. Res. Lett.*, *38*(L09501), 1–5.

Seroussi, H., H. Ben Dhia, M. Morlighem, E. Rignot, E. Larour, and D. Aubry (2012), Coupling ice flow models of varying order of complexity with the Tiling Method, *J. Glaciol.*, *58 (210)*, 776–786, doi:10.3189/2012JoG11J195.

Seroussi, H., M. Morlighem, E. Rignot, A. Khazendar, E. Larour, and J. Mouginot (2013), Dependence of century-scale projections of the Greenland ice sheet on its thermal regime, *J. Glaciol.*, *59*(218), 1024–1034, doi:10.3189/2013JoG13J054.

Seroussi, H., M. Morlighem, E. Larour, E. Rignot, and A. Khazendar (2014), Hydrostatic grounding line parameterization in ice sheet models, *The Cryosphere*, *8*, 2075–2087.

Seroussi, H., Y. Nakayama, E. Larour, D. Menemenlis, M. Morlighem, E. Rignot, and A. Khazendar (2017), Continued retreat of Thwaites Glacier, West Antarctica, controlled by bed topography and ocean circulation, *Geophys. Res. Lett.*, doi:10.1002/2017GL072910.

Shapiro, N. M., and M. H. Ritzwoller (2004), Inferring surface heat flux distributions guided by a global seismic model: particular application to Antarctica, *Earth Planet. Sci. Lett.*, *223*(1-2), 213–224, doi:10.1016/j.epsl.2004.04.011.

Shepherd, A., E. R. Ivins, G. A, V. R. Barletta, M. J. Bentley, S. Bettadpur, K. H. Briggs, D. H. Bromwich, R. Forsberg, N. Galin, M. Horwath, S. Jacobs, I. Joughin, M. a. King, J. T. M. Lenaerts, J. Li, S. R. M. Ligtenberg, A. Luckman, S. B. Luthcke, M. McMillan, R. Meister, G. Milne, J. Mouginot, A. Muir, J. P. Nicolas, J. Paden, A. J. Payne, H. Pritchard, E. Rignot, H. Rott, L. S. Sø rensen, T. a. Scambos, B. Scheuchl, E. J. O. Schrama, B. Smith, A. V. Sundal, J. H. van Angelen, W. J. van de Berg, M. R. van den Broeke, D. G. Vaughan, I. Velicogna, J. Wahr, P. L. Whitehouse, D. J. Wingham, D. Yi, D. Young, and H. J. Zwally (2012), A reconciled estimate of ice-sheet mass balance., *Science (New York, N.Y.)*, *338*(6111), 1183–9.

Spence, P., S. M. Griffie, M. H. England, A. M. Hogg, O. A. Saenko, and N. C. Jourdain (2014), Rapid subsurface warming and circulation changes of Antarctic coastal waters by poleward shifting winds, *Geophys. Res. Lett.*, *41*, 4601–4610, doi:10.1002/2014GL060613. Received.

Stocker, T., D. Qin, G.-K. Plattner, L. Alexander, S. Allen, N. Bindoff, F.-M. Bron, J. Church, U. Cubasch, S. Emori, P. Forster, P. Friedlingstein, N. Gillett, J. Gregory, D. Hartmann, E. Jansen, B. Kirtman, R. Knutti, K. Krishna Kumar, P. Lemke, J. Marotzke, V. Masson-Delmotte, G. Meehl, I. Mokhov, S. Piao, V. Ramaswamy, D. Randall, M. Rhein, M. Rojas, C. Sabine, D. Shindell, L. Talley, D. Vaughan, and S.-P. Xie (2013), *Technical Summary*, book section TS, p. 33115, Cambridge University Press, Cambridge, United Kingdom and New York, NY, USA, doi:10.1017/CBO9781107415324.005.

Thomas, R. H. (1979), Ice shelves: A review, *J. Glaciol.*, *24*(90), 273–286.

Tsai, V. C., A. L. Stewart, and A. F. Thompson (2015), Marine ice-sheet profiles and stability under Coulomb basal conditions, *J. Glaciol.*, *61*(226), 205–215, doi:10.3189/2015JoG14J221.

Uotila, P., A. H. Lynch, J. J. Cassano, and R. I. Cullather (2007), Changes in Antarctic net precipitation in the 21st century based on Intergovernmental Panel on Climate Change (IPCC) model scenarios, *Journal of Geophysical Research Atmospheres*, *112*(10), 1–19, doi:10.1029/2006JD007482.

van der Veen, C. J. (1998a), Fracture mechanics approach to penetration of surface crevasses on glaciers, *Cold Reg. Sci. Technol.*, *27*(1), 31–47.

van der Veen, C. J. (1998b), Fracture mechanics approach to penetration of bottom crevasses on glaciers, *Cold Reg. Sci. Technol.*, *27*(3), 213–223.

van der Veen, C. J., and I. M. Whillans (1989), Force budget: I. Theory and numerical methods, *J. Glaciol.*, *35*, 53–60.

Vaughan, D. G., H. F. J. Corr, R. A. Bindschadler, P. Dutrieux, G. H. Gudmundsson, A. Jenkins, T. Newman, P. Vornberger, and D. J. Wingham (2012), Subglacial melt channels and fracture in the floating part of Pine Island Glacier, Antarctica, *J. Geophys. Res. - Earth Surface*, *117*(F3), doi:10.1029/2012JF002360.

Vieli, A., and A. J. Payne (2005), Assessing the ability of numerical ice sheet models to simulate grounding line migration, *J. Geophys. Res.*, *110*(F1), F01,003, doi:10.1029/2004JF000202.

Vogel, C. R. (2002), *Computational Methods for Inverse Problems*, Society for Industrial and Applied Mathematics, Philadelphia, PA, USA.

Weertman, J. (1957), On the sliding of glaciers, *J. Glaciol.*, *3*, 33–38.

Weertman, J. (1973), Can a water-filled crevasse reach the bottom surface of a glacier?, *IASH Publ*, *95*, 139–145.

Weertman, J. (1974), Stability of the junction of an ice sheet and an ice shelf, *J. Glaciol.*, *13(67)*(67), 3–11.

Weiss, J. (2004), Subcritical crack propagation as a mechanism of crevasse formation and iceberg calving, *Journal of Glaciology*, *50*, 109–115.

Wise, M. G., J. A. Dowdeswell, M. Jakobsson, and R. D. Larter (2017), Evidence of marine ice-cliff instability in Pine Island Bay from iceberg-keel plough marks, *Nature*, *550*(7677), 506–510, doi:10.1038/nature24458.

Yu, H., E. Rignot, M. Morlighem, and H. Seroussi (2017), Iceberg calving of Thwaites Glacier, West Antarctica: Full-Stokes modeling combined with linear elastic fracture mechanics, *The Cryosphere*, *11*(3), 1283–1296, doi:10.5194/tc-11-1283-2017.

Zienkiewicz, O. C., and R. Codina (1995), A General Algorithm For Compressible And Incompressible-Flow .1. The Split, Characteristic-Based Scheme, *Int. J. Numer. Meth. Fluids*, *20*(8-9), 869–885.